Delft University of Technology

Topology, Magnetism, and Spin-Orbit: A Band Structure Study of Semiconducting Nanodevices

Skolasinski, Rafal

DOI
10.4233/uuid:c6543b39-401d-4d7d-9456-e54b02d71a69

Publication date
2018

Citation (APA)
Skolasinski, R. (2018). *Topology, Magnetism, and Spin-Orbit: A Band Structure Study of Semiconducting Nanodevices*. [Dissertation (TU Delft), Delft University of Technology].
https://doi.org/10.4233/uuid:c6543b39-401d-4d7d-9456-e54b02d71a69

Important note
To cite this publication, please use the final published version (if applicable).
Please check the document version above.

Copyright
Other than for strictly personal use, it is not permitted to download, forward or distribute the text or part of it, without the consent of the author(s) and/or copyright holder(s), unless the work is under an open content license such as Creative Commons.

Takedown policy
Please contact us and provide details if you believe this document breaches copyrights.
We will remove access to the work immediately and investigate your claim.

This work is downloaded from Delft University of Technology.
For technical reasons the number of authors shown on this cover page is limited to a maximum of 10.

TOPOLOGY, MAGNETISM, AND SPIN-ORBIT: A BAND STRUCTURE STUDY OF SEMICONDUCTING NANODEVICES

TOPOLOGY, MAGNETISM, AND SPIN-ORBIT: A BAND STRUCTURE STUDY OF SEMICONDUCTING NANODEVICES

Proefschrift

ter verkrijging van de graad van doctor
aan de Technische Universiteit Delft,
op gezag van de Rector Magnificus prof. dr. ir. T.H.J.J. van der Hagen.
voorzitter van het College voor Promoties,
in het openbaar te verdedigen op dinsdag 23 mei 2018 om 12:30 uur

door

Rafał Jarosław SKOLASIŃSKI

Master of Science in Physics,
University of Warsaw, Warschau, Polen,
geboren te Warschau, Polen.

Dit proefschrift is goedgekeurd door de

promotor: prof. dr. Y. V. Nazarov
copromotor: dr. M. T. Wimmer

Samenstelling promotiecommissie:

Rector Magnificus,	voorzitter
prof. dr. Y. V. Nazarov,	Technische Universiteit Delft, promotor
dr. M. T. Wimmer,	Technische Universiteit Delft, copromotor
prof. dr. J. Tworzydło,	University of Warsaw, Poland
dr. ir. F. A. Zwanenburg,	University of Twente
prof. dr. M. S. Golden,	University of Amsterdam
prof. dr. K. Flensberg,	University of Copenhagen, Denmark
prof. dr. Y. M. Blanter,	Technische Universiteit Delft
prof. dr. ir. L. P. Kouwenhoven,	Technische Universiteit Delft, reservelid

Printed by: Gildeprint

Front & Back: Copyright © 2018 by R.J. Skolasinski and K. Valečkaitė

Copyright © 2018 by R.J. Skolasinski

Casimir PhD Series, Delft-Leiden 2018-12

ISBN 978-90-8593-344-1

An electronic version of this dissertation is available at
`http://repository.tudelft.nl/`.

CONTENTS

SUMMARY

Topological insulators and topological superconductors are novel states of matter. These unique states are distinguished from ordinary states by a nontrivial value of their topological invariants, hence the name: topological insulators. A phase transition between the trivial and the topological phases is not characterized by a breaking of an underlying symmetry and may occur only when the energy gap closes, effectively making the system conducting.

One of the most characteristic properties of topological insulators are the topological edge states. They emerge on the boundary between a material in the topological and the trivial phase. While the bulk of the material stays insulating, the edge-state conductance is quantized and topologically protected from backscattering. In topological superconductors the edge states manifest themselves in the form of Majorana bound states: zero energy states inside the superconducting gap that are located at the end of a one-dimensional topological superconductor.

Despite the fact that the the study of topological materials is relatively new, it very quickly attracted the interests from both experimental and theoretical physicists, and is intensively studied from the perspective of fundamental research as well as the possible application for building a quantum computer.

Chapter 2 of this thesis contains a detailed review and a discussion of **k**·**p**-theory. **k**·**p**-theory allows one to go beyond commonly used effective models and obtain much more detailed description of a semiconductor's band structure around its gap. Topological insulators are often semiconductor-based and topological superconductors can be realized in a hybrid structure that consists of a semiconductor and a conventional superconductor. Because of that, the **k**·**p**-theory based band structure calculations are one of the main tools used in the research of topological materials. Chapter 3 covers implementation details of the numerical methods used in this thesis.

The two-dimensional topological insulator (2D TI), also known as the quantum spin Hall effect, is one example of a topological insulator. This effect has been theoretically predicted and observed in semiconductor-based quantum wells: HgTe or InAs/GaSb. As we change the thickness of the quantum well, we shift the conduction and valence band edges, and effectively cause band inversion. This leads to a topological phase that is characterized by topologically protected helical edge states which carry electric current with a quantized conductance $G = 2e^2/h$.

It was generally believed that in-plane magnetic field would break time reversal symmetry, suppress the conductance due to backscattering and open an energy gap in the edge-state dispersion. However, the experiment conducted by Du et al. reported robust helical edge transport in InAs/GaSb persisting up to a magnetic fields of 12 T. This discrepancy could not be explained with the commonly used BHZ model. In Chapter 4 of

this thesis we show that the burying of a Dirac point in the valence band, a feature of the system dispersion revealed only by the detailed **k·p**-simulation, explains this unexpected observation.

Once an experimental sample, a Hall bar made of InAs/GaSb quantum well, is fabricated, one can still tune the system between topological and trivial regimes by applying a gate voltage. This effect was studied in detail by the experimental group of L. P. Kouwenhoven in Delft. In a follow-up experiment, the details of spin-orbit interaction of this system in both topological (two-carrier regime) and trivial (single-carrier regime) phases have been investigated. In Chapter 5 we connect the results of this experiment with our band structure calculations: in the two-carrier regime, a quenching of the spin-splitting is observed and attributed to a crossing of spin bands, whereas in the single-carrier regime, the Rashba coefficient α changes linearly with electric field and the linear Dresselhaus coefficient β is constant.

We then take a look into the spin texture of the inverted InAs/GaSb system close to the hybridization gap. Transport measurements conducted by the experimental group of C. M. Marcus in Copenhagen revealed a giant spin-orbit splitting inherent to this system. This leads to a unique situation in which the Fermi energy in InAs/GaSb crosses a single spin-resolved band, resulting in a full spin-orbit polarization. We discuss this phenomenon in detail in Chapter 6.

In the last chapter of this thesis we move away from two-dimensional topological insulators and focus on topological superconductors. Semiconducting nanowires with induced superconductivity, inherent spin-orbit, and applied magnetic field are considered to be a promising platform for hosting Majorana bound states (MBS) with the first successful experiments over the last few years.

As the creation of the MBS requires a large enough magnetic field, such that $(g\mu_B B)^2 > \Delta^2 + \mu^2$, systems with large g-factors are of particular interest. In such a system this condition can be met by using smaller magnetic fields, which is beneficial for the superconductivity. In collaboration with theoretical physicists from ETH Zürich, we show that the orbital contribution to the electron g-factor in higher subbands of small-effective-mass semiconducting nanowires can lead to the g-factors that are larger by an order of magnitude or more than a bulk value g^*.

SAMENVATTING

Topologische isolatoren en topologische supergeleiders zijn nieuwe materietoestanden. Deze unieke toestanden onderscheiden zich van gewone toestanden door een niet-triviale waarde van hun topologische invariant, vandaar de naam topologische isolator. Een fasetransitie van de triviale naar de topologische toestand wordt niet gekenmerkt door de opheffing van een onderliggende symmetrie, en kan alleen plaatsvinden als de bandkloof sluit, waardoor het systeem geleidend wordt.

Eén van de meest karakteristieke eigenschappen van topologische isolatoren zijn topologische randtoestanden. Zij ontstaan op de grens van topologische en triviale materie. Terwijl de bulk van de materie isolerend blijft is de geleiding door randtoestanden gekwantiseerd en topologisch beschermd tegen terugverstrooiing. In topologische supergeleiders manifesteren de randtoestanden zichzelf in de vorm van Majorana-toestanden: toestanden van nul energie binnen de supergeleidende kloof, gelokaliseerd aan het einde van een ééndimensionale topologische supergeleider.

Ondanks het feit dat de studie van topologische materialen relatief nieuw is heeft het zeer snel de aandacht getrokken van zowel experimentele als theoretische fysici, en is het intensief bestudeerd zowel vanuit het perspectief van fundamenteel onderzoek als vanuit de mogelijke toepassing voor het bouwen van een kwantumcomputer.

Hoofdstuk 2 van deze thesis bevat een gedetailleerde bespreking van $\mathbf{k}\cdot\mathbf{p}$-theorie. $\mathbf{k}\cdot\mathbf{p}$-theorie stelt in staat om verder te gaan dan de gewoonlijk gebruikte effectieve modellen en om een veel gedetailleerdere beschrijving te verkrijgen van de bandenstructuur van een halfgeleider rondom de bandkloof. Topologische isolatoren zijn vaak gebaseerd op halfgeleiders en topologische supergeleiders kunnen worden gerealiseerd in een hybride structuur bestaande uit een halfgeleider en een conventionele supergeleider. Daardoor zijn $\mathbf{k}\cdot\mathbf{p}$-theorie-gebaseerde bandenstructuurberekeningen één van de belangrijkste gereedschappen die worden gebruikt in het onderzoek naar topologische materialen. Hoofdstuk 3 bevat details van de implementatie van de numerieke methoden die in deze thesis gebruikt worden.

De tweedimensionale topologische isolator (2D TI), ook bekend als het kwantum spin Halleffect, is een voorbeeld van een topologische isolator. Dit effect is theoretisch voorspeld en geobserveerd in op halfgeleiders gebaseerde kwantumputten: HgTe of InAs/GaSb. Wanneer we de breedte van de kwantumput aanpassen, verschuiven we de geleidings- en de valentiebandranden en veroorzaken daarmee effectief een bandinversie. Dit leidt tot een topologische fase die wordt gekarakteriseerd door topologisch beschermde spiraalvormige randtoestanden die een elektrische stroom dragen met een gekwantiseerde geleiding $G = 2e^2/h$.

Algemeen werd aangenomen dat een in het vlak gericht magnetisch veld de tijdsomkeringsymmetrie zou breken, de geleiding door terugverstrooiing zou onderdrukken en een energiekloof zou openen in de randtoestanddispersie. Het experiment uitgevoerd door Du et al. rapporteerde echter robuust schroefvorming randtransport in InAs/GaSb, aanhoudend tot een magnetisch veld van 12 T. Deze tegenstrijdigheid kon niet worden verklaard met het algemeen gebruikte BHZ-model. In Hoofdstuk 4 van deze thesis laten we zien dat het begraven van een Diracpunt in de valentieband, een eigenschap van de systeemdispersie die alleen onthuld wordt door een gedetailleerde $\mathbf{k}\cdot\mathbf{p}$-simulatie, deze onverwachte observatie verklaard.

Zodra een experimenteel sample, een Hallstaaf vervaardigd in een InAs/GaSb-kwantumput, is gefabriceerd, kan men nog steeds het systeem afstellen tussen topologische en triviale regimes door het aanbrengen van een gate-voltage. Dit effect is in detail bestudeerd door de experimentele groep van L. P. Kouwenhoven in Delft. In een opvolgend experiment zijn de details van de spin-baaninteractie van dit system bestudeerd in zowel de topologische fase (dubbele-ladingsdragerregime) als de triviale fase (enkele-ladingsdragerregime). In Hoofdstuk 5 verbinden we de resultaten van dit experiment met onze bandenstructuurberekeningen: in het dubbele-ladingsdragerregime wordt een afnemende spinsplitsing geobserveerd en toegeschreven aan een kruising van spinbanden, terwijl in het enkele-ladingsdragerregime de Rashba-coëfficiënt α lineair verandert als functie van het elektrische veld en de lineaire Dresselhaus-coëfficiënt β constant is.

Daarna beschouwen we de spinstructuur van het geïnverteerde InAs/GaSb-systeem dichtbij de hybridisatiekloof. Transportmetingen uitgevoerd door de experimentele groep van C. M. Marcus in Copenhagen onthulden een gigantische spin-baansplitsing inherent aan dit systeem. Dit leidt to een unieke situatie waarin de Fermi-energie in InAs/GaSb een enkele spinband kruist, resulterend in een volledige spin-baanpolarisatie. We bespreken dit fenomeen in detail in Hoofdstuk 6.

In het laatste hoofdstuk van deze thesis keren we ons af van twee-dimensionale topologische isolatoren en focussen we op topologische supergeleiders. Halfgeleidende draden met geïnduceerde supergeleiding, inherente spin-baankoppeling en een aangebracht magneetveld worden beschouwd als een veelbelovend platform voor gebonden Majorana-toestanden, met de eerste succesvolle experimenten gedurende de afgelopen jaren. Aangezien de creatie van gebonden Majorana-toestanden een groot genoeg magnetisch veld vereist zodanig dat $(g\mu_B B)^2 > \Delta^2 + \mu^2$ zijn systemen met grote g-factoren zeer gewild. In zulke systemen kan aan deze conditie worden voldaan met kleinere magneetvelden, wat gunstig is voor de supergeleiding. In samenwerking met theoretisch natuurkundigen van de ETH Zürich laten we zien dat de orbitaalcontributie aan de elektron-g-factor in hogere subbanden voor halfgeleidende nanodraden met kleine effectieve massa kan leiden tot g-factoren die een ordegrootte groter zijn dan de g-factor in de bulk.

1

INTRODUCTION

1.1. PREFACE

Imagine an apple and a doughnut or, to be more mathematically precise, a sphere and a torus. Are these two the same? They are not. Add to them now a coffee cup and ask yourself the same question, are any of these objects the same as the others? You may think that the answer is the same and, in most situations, indeed it is. If you, however, consider surfaces of these objects from the perspective of mathematical topology, then this simple question gets a bit more complicated.

Mathematical topology characterizes equivalent surfaces by a topological invariant, called the genus, which is in general the number of holes in their surfaces. In other words, if we can smoothly transform one object into another, without cutting or piercing its surface, these objects are considered equal. Bearing that in mind, both the torus and the coffee mug are equivalent to each other but different from the sphere. This picture will help us understand the idea behind the main subject of my research: topological insulators.

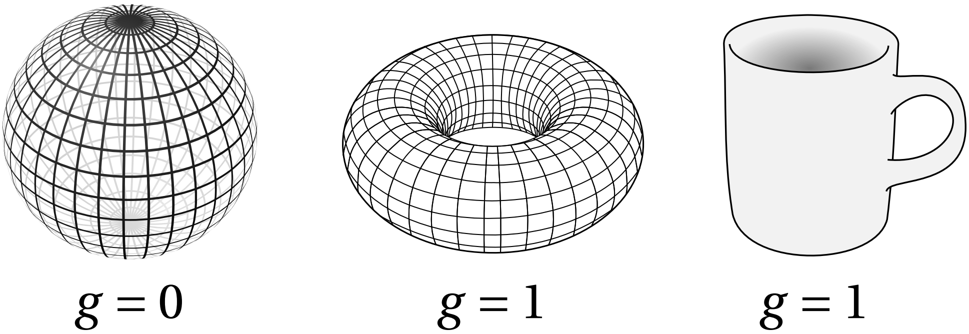

Figure 1.1: Surfaces of a sphere (left), a torus (middle), and a coffee cup (right). Each of the surfaces is characterized by the topological invariant g, called genus, that is in general equal to the number of holes in the surface. Surfaces with the same genus are considered topologically equivalent to each other. This figure is composed of materials distributed under the Creative Common licence, adapted from wikimedia.org.

In simple words, topological insulators are new electronic states of matter that are characterized by an insulating bulk and a conducting surface. We classify them by the topological invariants that define their key properties, e.g. conductance. Similarly, as with mathematical surfaces, we can transform one topological insulator into another, and as long as we don't make it conducting during the process, it is still the same object—the topological invariants that define its phase stay unchanged. This leads to a very interesting property of topological insulators: a small perturbation does not change properties of the topological phase.

1.2. TOPOLOGICAL PHASES OF MATTER

Before the 1980s, phases of matter were understood using the theory developed by Lev Landau. This theory connects the phase transition with the breaking of some underlying symmetry, e.g. the water-ice transition is connected to the breaking of continuous translational symmetry when molecules of water organize themselves into a crystalline structure.

The situation changed drastically after the discovery of the quantum Hall effect (QHE) in 1980 by von Klitzing [1]. When a two-dimensional electron gas (2DEG) is exposed to a strong perpendicular magnetic field, a unique state emerges at its edge. This state is characterized by quantized Hall conductivity, always in the form

$$G = N \times \frac{e^2}{h}, \tag{1.1}$$

where N is the number of filled Landau levels, e is the electron charge, and h is the Planck constant. Quantization of the Hall conductivity has been confirmed in multiple experiments which means that small differences in external conditions or usage of different samples does not destroy properties of the QHE phase.

In 1982 Thouless, Kohomoto, Nightingale and den Nijs (TKNN) explained that this unique property comes from the topology of the system's band structure [2]. They showed that the conduction G computed using the Kubo formula can be expressed in the same form as Eq. (1.1), using the topological invariant $n \in \mathbf{Z}$, called the Chern number [3], instead of the number of filled Landau levels, i.e. $n = N$. Furthermore, this topological invariant can change only when the gap closes and the system becomes conductive. This illustrates why the quantization of the Hall conductance is robust to small changes in external conditions, sample imperfections, or even the geometry of the sample itself.

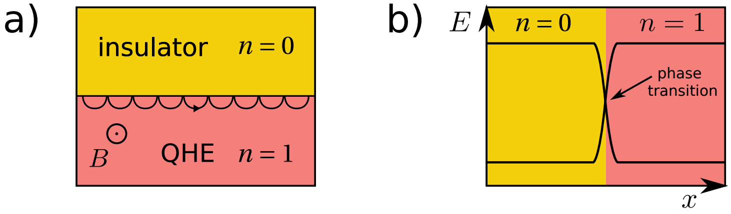

Figure 1.2: (a) Edge states in a QHE system. A magnetic field causes electrons to move in cyclotron orbits. Close to the interface with the ordinary insulator electrons bounce back from the edge and effectively travel along it. (b) Schematic view of the bulk-edge correspondence: at the interface between two materials with different topological invariants the energy gap vanishes. Therefore, there must be a low energy state bound to this region.

1.3. BULK-EDGE CORRESPONDENCE

Let us now discuss the origin of this unexpected edge state. In the case of QHE, it can be understood with a very simple picture. Electrons in strong magnetic field move in small cyclotron orbits—this leads us to the insulating bulk because there are simply no states that can carry the electric current. On the edge, however, the situation is different, an electron bounces back and effectively propagates along it, Fig. 1.2(a).

This quasi-classical picture gives us an intuition about one of the most important properties of topological insulators, known as bulk-edge correspondence. If we have an interface between a topological and an ordinary insulator, then as we go from one material to the other, the topological invariant changes and energy gap must vanish somewhere on the way. Therefore there will be a low energy electronic state bound to the region where a phase transition occurs [3], Fig. 1.2(b).

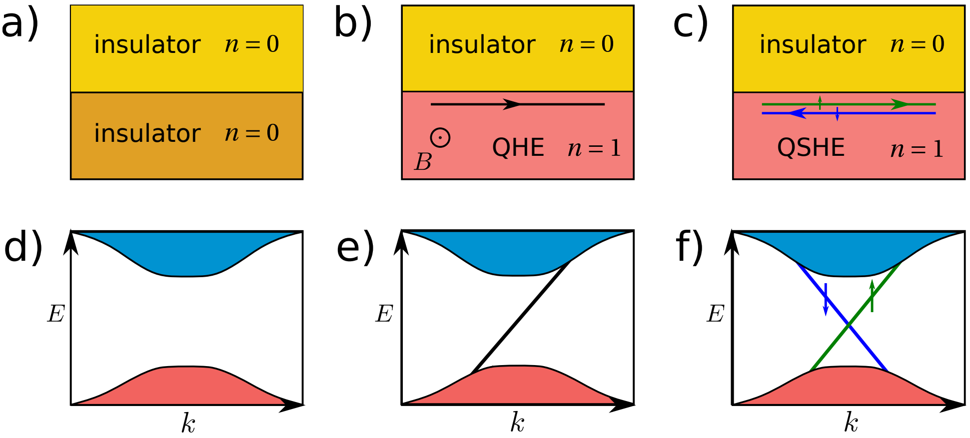

Figure 1.3: Edge states in two-dimensional topological insulators. (a, d) An interface between two normal insulators does not show any extraordinary behaviour, and dispersion of such system consists only of a conduction and a valence bands. (b) When we substitute one of the ordinary insulators with the quantum Hall system, a single edge state appears at the edge. (e) This state appears in the dispersion inside the bulk gap, connecting valence and conduction band, and propagates only in one direction. This edge state requires strong magnetic field to exist. (c) If a quantum spin Hall system is used instead, two edge states are created at the interface. (f) These edge states have opposite spins and propagate in opposite directions.

1.4. QUANTUM SPIN HALL EFFECT

The history of the quantum spin Hall effect (QSHE) starts with the pursuit of a topological phase based on a spin-orbit interaction [3]. Without a magnetic field, this phase would effectively be protected by time reversal symmetry (TRS), with topological properties similar to, but distinct from, QHE. At the turn of 2005 and 2006, two group independently proposed a realization of such a phase in graphene [4] and in semiconductor systems with uniform strain gradient [5].

A quantum spin Hall phase is characterized by helical edge states, i.e. counter-propagating states of opposite spin. In Fig. 1.3 I present differences in edge-state dispersion between QHE and QSHE. The crossing in the edge states in Fig. 1.3(c) is known as the Dirac point. This crossing is protected by TRS—Kramers theorem requires that every eigenstate at given energy E must be at least doubly degenerate. Unlike QHE, the quantum spin Hall effect does not require a magnetic field—on the contrary, the presence of a magnetic field would break the TRS and destroy the topological phase by opening a gap in edge states, as they would no longer be protected by TRS.

Unfortunately, due to a small energy gap and weak spin-orbit, the effect was not observed in proposed systems. A breakthrough moment came at the end of 2006 when Bernevig, Hughes and Zhang [6] proposed an alternative realization in HgTe/(Hg,Cd)Te quantum wells. The effective model that was used to predict the effect is now known as the BHZ model, named after its authors. The experimental confirmation came in the following year with an experiment conducted by the group of Laurens Molenkamp [7].

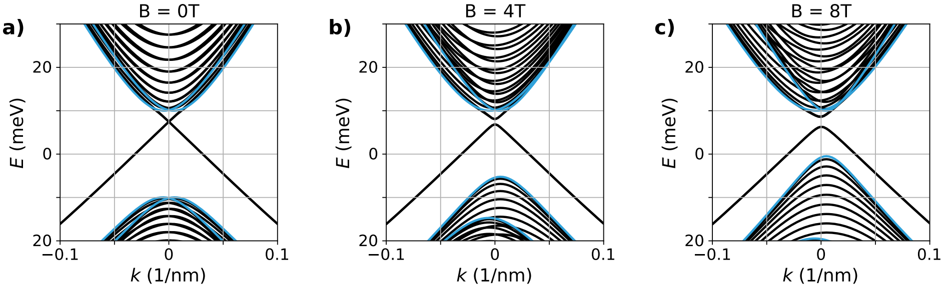

Figure 1.4: Dispersion of the edge states in BHZ model under an in-plane magnetic field. The magnetic field breaks the time-reversal-symmetry allowing an energy gap to open in the edge-states dispersion.

The BHZ model is a 4 × 4 band Hamiltonian derived with first order perturbation theory as

$$H^{\text{eff}}_{ij}(k_x, k_y) = \int_{-\infty}^{\infty} \langle \Psi_i | H_{\mathbf{k}\cdot\mathbf{p}}(k_x, k_y, -\mathrm{i}\partial_z) | \Psi_j \rangle \,, \tag{1.2}$$

where $H_{\mathbf{k}\cdot\mathbf{p}}$ is a six-band Kane model [8] and $\Psi_{1\ldots4} = (|E1,+\rangle, |H1,+\rangle, |E1,-\rangle, |H1,-\rangle)$ are the spin up/down states of the lowest Γ_6 conduction band and highest Γ_8 valence band in the HgTe/CdTe quantum well. Each of these states have a well defined symmetry in respect to z—$|E1,\pm\rangle$ is even in z, whereas $|H1,\pm\rangle$ is odd. This puts a certain constraint on the form of effective Hamiltonian that reads as

$$H_{\text{eff}} = \begin{pmatrix} H(\boldsymbol{k}) & 0 \\ 0 & H^*(-\boldsymbol{k}) \end{pmatrix} , \tag{1.3}$$

$$H(\boldsymbol{k}) = \epsilon(\boldsymbol{k}) + \boldsymbol{d}(\boldsymbol{k}) \cdot \boldsymbol{\sigma} \,, \tag{1.4}$$

where $\boldsymbol{k} = (k_x, k_y)$ is in-plane momentum, $\boldsymbol{\sigma} = (\sigma_1, \sigma_2, \sigma_3)$ is vector of Pauli matrices, and

$$d_1 + \mathrm{i}d_2 = A(k_x + \mathrm{i}k_y) \,, \tag{1.5}$$

$$d_3 = M - B(k_x^2 + k_y^2) \,, \tag{1.6}$$

$$\epsilon(\boldsymbol{k}) = C - D(k_x^2 + k_y^2) \,, \tag{1.7}$$

where A, B, C, and D are effective parameters that depend on the heterostructure geometry. The effect of a magnetic field is usually included through the Zeeman coupling matrices $M_{x,y,z}$, whereas the breaking of bulk inversion asymmetry is taken into account through the H_{BIA} term [9]:

$$M_x = \begin{pmatrix} & & g_{\parallel} & \\ & & & \\ g_{\parallel} & & & \\ & & & \end{pmatrix}, \quad M_y = \begin{pmatrix} & & -\mathrm{i}g_{\parallel} & \\ & & & \\ \mathrm{i}g_{\parallel} & & & \\ & & & \end{pmatrix},$$

$$M_z = \begin{pmatrix} g_{E_\perp} & & & \\ & g_{H_\perp} & & \\ & & -g_{E_\perp} & \\ & & & -g_{H_\perp} \end{pmatrix}, \quad H_{\mathrm{BIA}} = \begin{pmatrix} & & & -\Delta \\ & & \Delta & \\ & \Delta & & \\ -\Delta & & & \end{pmatrix}. \tag{1.8}$$

Figure 1.4(a) shows the band structure of the edge states calculated with this model. As we see on subfigures (b) and (c), magnetic field breaks TRS symmetry and opens an energy gap in the edge-state dispersion.

Soon after the experimental confirmation of QSHE in HgTe/CdTe another realization in InAs/GaSb quantum wells [10] was proposed and confirmed in experiments [11–13]. Gathered data [13] showed, however, an unexpected effect: an extraordinary robustness to the magnetic field. This was a surprising observation as the in-plane magnetic field should break TRS, open the gap in the edge states, distort the anti-parallel spin orientation and effectively lead to a drop in the conductance. In Chapter 4 of this thesis we investigate this issue further by going beyond the BHZ model.

Recent experiments conducted by the group of L. P. Kouwenhoven (Delft) and C. M. Marcus (Copenhagen) revealed more details on the spin-orbit interaction in InAs/GaSb based QSHE systems. These details were not captured by the BHZ model and were yet another example of the BHZ limitations. In Chapter 5 and Chapter 6 we present both results of these experiments and theoretical detailed analysis based on $\mathbf{k}\cdot\mathbf{p}$-method.

1.5. MAJORANA BOUND STATES

Majorana bound states (MBS) [14–16] are an example of another topological edge state. They are Andreev bound states inside the superconducting gap and are located at the end of a one-dimensional superconductor. Due to particle-hole symmetry, if such a state exists at finite energy E, it has a partner at energy $-E$ and could be pushed out of the gap. If we however have a single state at $E = 0$ then it cannot be pushed away—it is topologically protected. Due to their exotic exchange statistics [17–19], that are neither fermion nor boson like, and being robust to any local disorder, they are often considered to be a good platform for building a topological quantum computer [20–22].

To create Majorana bound states certain physical conditions must be met. The simplest theoretical model to describe them is the Kitaev chain [23] which is a one-dimensional tight-binding system with p-wave superconductivity and spinless electrons. Because of the exotic particle-hole coupling it is considered not to be a proposal of an experimental realization but rather a minimal model that helps to better understand MBS. However, the physics of the Kitaev chain can be realized with conventional materials if the following three ingredients are present: superconductivity which couples electrons and holes, magnetic field which breaks TRS and last but not least the spin-orbit interaction that breaks spin conservation.

Semiconducting nanowires with induced conventional superconductivity are considered to be one of most promising platforms for the realization of MBS [24–27]. Together with the spin-orbit interaction inherent to semiconductors and the possibility to apply a magnetic field along the wire, this proposal met all requirements for achieving MBS and led to the first successful experiments [28–32].

The effective Hamiltonian that describes the electrons in the first subband of semiconducting nanowires with spin-orbit coupling, magnetic field, and induced superconductivity is

$$H = -\left(\frac{p_x^2}{2m^*} + \mu\right)\tau_z + \alpha p_x \sigma_y \tau_z + g\mu_B B \sigma_z + \Delta \tau_x\,, \tag{1.9}$$

where p_x is the momentum, m^* is the effective mass, α the is strength of the spin-orbit coupling, g is the Landé g-factor, B is the magnetic field along the wire, and τ and σ are Pauli matrices acting in particle-hole and spin space, respectively. Both magnetic field and induced superconductivity are important ingredients for Majorana bound states. Unfortunately, these are competing effects because including strong magnetic fields suppresses the superconductivity. At the same time, MBS only appear for large enough magnetic field, so that

$$E_z^2 > \Delta^2 + \mu^2\,, \tag{1.10}$$

where $E_z = g\mu_B B$. However, if the Landé g-factor of the electron is large one can use smaller magnetic fields, which is beneficial for the superconductivity.

It is generally believed that the confinement leads to a reduced g-factor in semiconductor devices [33]. However, experiments in InAs [34, 35] and InSb [34, 35] found g-factors exceeding the bulk value by 40%. In a recent experiment [30], g-factors more than 3 times larger than the bulk value were measured. Furthermore, the g-factors in this experiment strongly depended on the chemical potential μ—for low μ small g-factors were found, whereas the anomalously large g-factors were found only for large μ. In Chapter 7, we investigate this problem in detail and present a mechanism that could lead to very large g-factors in higher subbands of semiconducting nanowires.

1.6. STRUCTURE OF THIS THESIS

1.6.1. CHAPTER 2 REVIEW OF **k·p** METHOD FOR SEMICONDUCTORS

In the first chapter of this thesis we review **k·p**-theory, a commonly used method in semiconductor research. We start our discussion with the theoretical background of **k·p**-theory quasi-degenerate perturbation theory, known as Löwdin partitioning. We continue with the symmetry analysis of III-V and II-VI semiconductors. Finally we derive an 8-band **k·p**-model, known as the Kane Hamiltonian. **k·p**-theory provides a more detailed description of the system's band structure compared to commonly used effective models that are usually derived directly from it.

1.6.2. CHAPTER 3: NUMERICAL METHODS FOR SEMICONDUCTORS

In the research of topological insulators, we often deal with devices of complicated geometry and structure, such as two-dimensional quantum wells or quantum nanowires. This puts a significant limit on the analytical study of these materials. Great advances in computer hardware and popularity of reliable open-source scientific libraries made numerical studies one of the most important tools that theoretical physicists can use.

Though computer simulations cannot replace an actual experiment, they often provide a valuable insight into the underlying physics. Thanks to this, we can investigate the effect of different geometries, or usage of different materials, before fabricating experimental samples. This allow us to adjust the design of the sample in order to achieve optimal physical properties, e.g. band gap or effective g-factors, before fabrication and measurement process.

This chapter discusses implementation details of $\mathbf{k}{\cdot}\mathbf{p}$-theory and Löwdin partitioning.

1.6.3. CHAPTER 4: ROBUST HELICAL EDGE TRANSPORT IN QUANTUM SPIN HALL QUANTUM WELLS

We show that burying of the Dirac point in semiconductor-based quantum spin Hall systems can generate unexpected robustness of edge states to magnetic fields. A detailed $\mathbf{k}{\cdot}\mathbf{p}$ band-structure analysis reveals that InAs/GaSb and HgTe/CdTe quantum wells exhibit such buried Dirac points. By simulating transport in a disordered system described within an effective model, we further demonstrate that buried Dirac points yield nearly quantized edge conduction even at large magnetic fields, consistent with recent experiments.

1.6.4. CHAPTER 5: SPIN-ORBIT INTERACTION IN A DUAL GATED InAs/GaSb QUANTUM WELL

Spin-orbit interaction is investigated in a dual gated InAs/GaSb quantum well. Using an electric field the quantum well can be tuned between a single carrier regime with exclusively electrons as carriers and a two-carrier regime where electrons and holes coexist. Spin-orbit interaction in both regimes manifests itself as a beating in the Shubnikov-de Haas oscillations. In the single carrier regime the linear Dresselhaus strength is characterized by $\beta = 28.5$ meVÅ and the Rashba coefficient α is tuned from 75 to 53 meVÅ by changing the electric field. This behaviour is qualitatively consistent with the parameters extracted from $\mathbf{k}{\cdot}\mathbf{p}$ calculations. In the two-carriers regime a quenching of the spin-splitting is observed and attributed to a crossing of spin bands.

1.6.5. CHAPTER 6: GIANT SPIN-ORBIT SPLITTING IN INVERTED InAs/GaSb DOUBLE QUANTUM WELLS

Transport measurements in inverted InAs/GaSb quantum wells reveal a giant spin-orbit splitting of the energy bands close to the hybridization gap. The splitting results from the interplay of electron-hole mixing and spin-orbit coupling, and can exceed the hybridization gap. We experimentally investigate the band splitting as a function of top gate voltage for both electron-like and hole-like states. Unlike conventional, noninverted two-dimensional electron gases, the Fermi energy in InAs/GaSb can cross a single spin-resolved band, resulting in full spin-orbit polarization. In the fully polarized regime we observe exotic transport phenomena such as quantum Hall plateaus evolving in e^2/h steps and a non-trivial Berry phase.

1.6.6. CHAPTER: 7: ORBITAL CONTRIBUTIONS TO THE ELECTRON g-FACTOR IN SEMICONDUCTOR NANOWIRES

Recent experiments on Majorana fermions in semiconductor nanowires [Albrecht *et al.*, Nat. 531, 206 (2016)] revealed a surprisingly large electronic Landé g-factor, several times larger than the bulk value—contrary to the expectation that confinement reduces the g-factor. Here we assess the role of orbital contributions to the electron g-factor in nanowires and quantum dots. We show that an $\mathbf{L}\cdot\mathbf{S}$ coupling in higher subbands leads to an enhancement of the g-factor by an order of magnitude or more for small effective mass semiconductors. We validate our theoretical findings with simulations of InAs and InSb, showing that the effect persists even if cylindrical symmetry is broken. A huge anisotropy of the enhanced g-factors under magnetic field rotation allows for a straightforward experimental test of this theory.

REFERENCES

[1] K. v. Klitzing, G. Dorda, and M. Pepper, *New Method for High-Accuracy Determination of the Fine-Structure Constant Based on Quantized Hall Resistance*, Phys. Rev. Lett. **45**, 494 (1980).

[2] D. J. Thouless, M. Kohmoto, M. P. Nightingale, and M. den Nijs, *Quantized Hall Conductance in a Two-Dimensional Periodic Potential*, Phys. Rev. Lett. **49**, 405 (1982).

[3] M. Z. Hasan and C. L. Kane, *Colloquium: Topological insulators*, Rev. Mod. Phys. **82**, 3045 (2010).

[4] C. L. Kane and E. J. Mele, *Quantum Spin Hall Effect in Graphene*, Phys. Rev. Lett. **95**, 226801 (2005).

[5] B. A. Bernevig and S.-C. Zhang, *Quantum Spin Hall Effect*, Phys. Rev. Lett. **96**, 106802 (2006).

[6] B. A. Bernevig, T. L. Hughes, and S.-C. Zhang, *Quantum Spin Hall Effect and Topological Phase Transition in HgTe Quantum Wells*, Science **314**, 1757 (2006).

[7] M. König, S. Wiedmann, C. Brüne, A. Roth, H. Buhmann, L. W. Molenkamp, X.-L. Qi, and S.-C. Zhang, *Quantum Spin Hall Insulator State in HgTe Quantum Wells*, Science **318**, 766 (2007).

[8] E. O. Kane, *Band structure of indium antimonide*, J Phys Chem Solids **1**, 249–261 (1957).

[9] M. König, H. Buhmann, L. W. Molenkamp, T. Hughes, C.-X. Liu, X.-L. Qi, and S.-C. Zhang, *The Quantum Spin Hall Effect: Theory and Experiment*, J. Phys. Soc. Jpn. **77**, 031007 (2008).

[10] C. Liu, T. L. Hughes, X.-L. Qi, K. Wang, and S.-C. Zhang, *Quantum Spin Hall Effect in Inverted Type-II Semiconductors*, Phys. Rev. Lett. **100**, 236601 (2008).

[11] I. Knez, R.-R. Du, and G. Sullivan, *Evidence for Helical Edge Modes in Inverted* InAs/GaSb *Quantum Wells*, Phys. Rev. Lett. **107**, 136603 (2011).

[12] I. Knez, C. T. Rettner, S.-H. Yang, S. S. Parkin, L. Du, R.-R. Du, and G. Sullivan, *Observation of Edge Transport in the Disordered Regime of Topologically Insulating* InAs/GaSb *Quantum Wells,* Phys. Rev. Lett. **112**, 026602 (2014).

[13] L. Du, I. Knez, G. Sullivan, and R.-R. Du, *Robust Helical Edge Transport in Gated* InAs/GaSb *Bilayers,* Phys. Rev. Lett. **114**, 096802 (2015).

[14] R. F. Service, *Search for Majorana Fermions Nearing Success at Last?* Science **332**, 193 (2011).

[15] F. Wilczek, *Majorana returns,* Nature Physics **5**, 614 (2009).

[16] C. Beenakker and L. Kouwenhoven, *A road to reality with topological superconductors,* Nature Physics **12**, 618 (2016).

[17] D. A. Ivanov, *Non-Abelian Statistics of Half-Quantum Vortices in p-Wave Superconductors,* Phys. Rev. Lett. **86**, 268 (2001).

[18] N. Read and D. Green, *Paired states of fermions in two dimensions with breaking of parity and time-reversal symmetries and the fractional quantum Hall effect,* Phys. Rev. B **61**, 10267 (2000).

[19] S. D. Sarma, M. Freedman, and C. Nayak, *Majorana zero modes and topological quantum computation,* Npj Quantum Inf. **1**, 15001 (2015).

[20] A. Y. Kitaev, *Fault-tolerant quantum computation by anyons,* Annals of Physics **303**, 2 (2003).

[21] M. H. Freedman, *P/NP, and the quantum field computer,* PNAS **95**, 98 (1998).

[22] C. Nayak, S. H. Simon, A. Stern, M. Freedman, and S. Das Sarma, *Non-Abelian anyons and topological quantum computation,* Rev. Mod. Phys. **80**, 1083 (2008).

[23] A. Y. Kitaev, *Unpaired Majorana fermions in quantum wires,* Phys.-Usp. **44**, 131 (2001).

[24] J. D. Sau, R. M. Lutchyn, S. Tewari, and S. Das Sarma, *Generic New Platform for Topological Quantum Computation Using Semiconductor Heterostructures,* Phys. Rev. Lett. **104**, 040502 (2010).

[25] J. Alicea, *Majorana fermions in a tunable semiconductor device,* Phys. Rev. B **81**, 125318 (2010).

[26] R. M. Lutchyn, J. D. Sau, and S. Das Sarma, *Majorana Fermions and a Topological Phase Transition in Semiconductor-Superconductor Heterostructures,* Phys. Rev. Lett. **105**, 077001 (2010).

[27] Y. Oreg, G. Refael, and F. von Oppen, *Helical Liquids and Majorana Bound States in Quantum Wires,* Phys. Rev. Lett. **105**, 177002 (2010).

[28] V. Mourik, K. Zuo, S. M. Frolov, S. R. Plissard, E. P. a. M. Bakkers, and L. P. Kouwenhoven, *Signatures of Majorana Fermions in Hybrid Superconductor-Semiconductor Nanowire Devices,* Science **336**, 1003 (2012).

[29] A. Das, H. Shtrikman, M. Heiblum, Y. Most, Y. Oreg, and Y. Ronen, *Zero-bias peaks and splitting in an Al–InAs nanowire topological superconductor as a signature of Majorana fermions,* Nat. Phys. **8**, 887 (2012).

[30] S. M. Albrecht, A. P. Higginbotham, M. Madsen, F. Kuemmeth, T. S. Jespersen, J. Nygård, P. Krogstrup, and C. M. Marcus, *Exponential protection of zero modes in Majorana islands,* Nature **531**, 206 (2016).

[31] H. Zhang, Ö. Gül, S. Conesa-Boj, M. P. Nowak, M. Wimmer, K. Zuo, V. Mourik, F. K. d. Vries, J. v. Veen, M. W. A. d. Moor, J. D. S. Bommer, D. J. v. Woerkom, D. Car, S. R. Plissard, E. P. A. M. Bakkers, M. Quintero-Pérez, M. C. Cassidy, S. Koelling, S. Goswami, K. Watanabe, T. Taniguchi, and L. P. Kouwenhoven, *Ballistic superconductivity in semiconductor nanowires,* Nat. Commun. **8**, 16025 (2017).

[32] Ö. Gül, H. Zhang, J. D. S. Bommer, M. W. A. de Moor, D. Car, S. R. Plissard, E. P. A. M. Bakkers, A. Geresdi, K. Watanabe, T. Taniguchi, and L. P. Kouwenhoven, *Ballistic Majorana nanowire devices,* Nature Nanotechnology (2018), 10.1038/s41565-017-0032-8.

[33] R. Winkler, *Spin-Orbit Coupling Effects in Two-Dimensional Electron and Hole Systems* (Springer, Berlin, Heidelberg, 2003).

[34] S. Csonka, L. Hofstetter, F. Freitag, S. Oberholzer, C. Schönenberger, T. S. Jespersen, M. Aagesen, and J. Nygård, *Giant Fluctuations and Gate Control of the g-Factor in InAs Nanowire Quantum Dots,* Nano Lett. **8**, 3932 (2008).

[35] M. D. Schroer, K. D. Petersson, M. Jung, and J. R. Petta, *Field Tuning the g Factor in InAs Nanowire Double Quantum Dots,* Phys. Rev. Lett. **107**, 176811 (2011).

2

REVIEW OF k·p METHOD FOR SEMICONDUCTORS

In this section we discuss the theoretical background of a commonly used method in the semiconductor research: **k·p**-theory [1–9]. This is an approximated method that gives us an effective Hamiltonian. This effective Hamiltonian describes bulk dispersion of a valence and a conduction band around high-symmetry points in the Brillouin zone. All other bands, referred to as remote bands, are integrated out using a quasi-degenerate perturbation theory.

By employing proper boundary conditions, these bulk models can be further used to describe low-dimensional systems, such as two-dimensional quantum wells and one-dimensional nanowires. Using the **k·p**-method gives more accurate results than simpler models, like effective mass approximation for conduction band electrons, that can be derived directly from the **k·p** Hamiltonian using perturbation theory.

The quasi-degenerate perturbation theory [10–13], known as Löwdin partitioning, is an extension of the standard quantum mechanical perturbation theory to cases with the quasi degenerate states. It is particularly helpful in finding effective low-energy models, that give us more insight into the underlying physics or provide a simple and elegant description of a considered physical system.

2.1. THEORETICAL BACKGROUND

2.1.1. k·p METHOD FOR SEMICONDUCTORS

We start our derivation with the Schrödinger equation

$$\left(\frac{\hat{\boldsymbol{p}}^2}{2m_o} + V(\boldsymbol{x})\right)\varphi_n(\boldsymbol{x}) = E_n\psi_n(\boldsymbol{x})\,, \tag{2.1}$$

where $V(\boldsymbol{x})$ is a periodic crystal potential and m_0 is free electron mass. Because of the potential periodicity we make use of the Bloch theorem

$$V(\boldsymbol{x}+\boldsymbol{R}) = V(\boldsymbol{x}) \quad \Rightarrow \quad \psi(\boldsymbol{x}) = e^{i\boldsymbol{k}\cdot\boldsymbol{x}}u_{n,\boldsymbol{k}}(\boldsymbol{x})\,, \tag{2.2}$$

where $\boldsymbol{R}$ is a lattice vector, $\boldsymbol{k}$ is a crystal momentum and $u_{n,\boldsymbol{k}}(\boldsymbol{x})$ is a periodic Bloch function. We then rewrite the Schrödinger equation as

$$e^{i\boldsymbol{k}\cdot\boldsymbol{x}}\left\{\frac{(\hat{\boldsymbol{p}}+\hbar\boldsymbol{k})^2}{2m_o} + V(\boldsymbol{x})\right\}u_{n,\boldsymbol{k}}(\boldsymbol{x}) = E_n e^{i\boldsymbol{k}\cdot\boldsymbol{x}}u_{n,\boldsymbol{k}}(\boldsymbol{x})\,. \tag{2.3}$$

Now, we drop out the exponential factor, and obtain following eigenvalue problem

$$H(\boldsymbol{k}) = \frac{\hat{\boldsymbol{p}}^2}{2m_o} + \frac{\hbar^2\boldsymbol{k}^2}{2m_o} + \frac{\hbar}{m_o}\boldsymbol{k}\cdot\hat{\boldsymbol{p}} + V(\boldsymbol{x})\,, \tag{2.4a}$$

$$H(\boldsymbol{k})u_{n,\boldsymbol{k}}(\boldsymbol{x}) = E_n(\boldsymbol{k})u_{n,\boldsymbol{k}}(\boldsymbol{x})\,, \tag{2.4b}$$

for the Bloch functions $u_{n,\boldsymbol{k}}(\boldsymbol{x})$. Note that the energies $E_n(\boldsymbol{k})$ now depend on crystal momentum $\boldsymbol{k}$.

The remaining problem is to obtain the band structure $E_n(\boldsymbol{k})$ by solving Eq. (2.4b). There exist numerous methods designed for this task. Here, we use **k·p** approach that we now explain in more detail.

In semiconductors, the electrons that are responsible for the transport properties usually occupy only a region of energies close to the semiconducting gap. We can therefore limit our discussion to only these states that corresponds to the top of a valence band and the bottom of a conduction band. The band structure of the remaining bands is not relevant, and the effect of these remote bands can be included through a quasi-degenerate perturbation theory, Furthermore, the precise knowledge of the dispersion in whole Brillouin zone is not required, and it is sufficient to obtain the band structure $E_n(\boldsymbol{k})$ around its extremum point, that we denote as $\boldsymbol{k_0}$.

We separate $H(\boldsymbol{k})$ into a constant extremum part $H(\boldsymbol{k_0})$ and a remaining $\boldsymbol{k}$ dependent part as

$$H(\boldsymbol{k}) = H(\boldsymbol{k_0}) + \frac{\hbar^2(\boldsymbol{k}^2 - \boldsymbol{k_0}^2)}{2m_o} + \frac{\hbar}{m_o}(\boldsymbol{k} - \boldsymbol{k_0}) \cdot \hat{\boldsymbol{p}}\,, \tag{2.5}$$

with

$$H(\boldsymbol{k_0})u_{n,\boldsymbol{k_0}}(\boldsymbol{x}) = E_n(\boldsymbol{k_0})u_{n,\boldsymbol{k_0}}(\boldsymbol{x})\,, \tag{2.6}$$

for which we treat energies $E_n(\boldsymbol{k_0})$ and wave functions $u_{n,\boldsymbol{k_0}}(\boldsymbol{x})$ as known. Because $u_{n,\boldsymbol{k_0}}(\boldsymbol{x})$ form a complete and orthonormal basis we use them to expand $u_{n,\boldsymbol{k}}(\boldsymbol{x})$ as

$$u_{n,\boldsymbol{k}}(\boldsymbol{x}) = \sum_{\mu} c_{n,\mu}(\boldsymbol{k})\; u_{\mu,\boldsymbol{k_0}}(\boldsymbol{x})m\,, \tag{2.7}$$

where $c_{n,\mu}(\boldsymbol{k})$ are the expansion coefficients. We substitute Eq. (2.7) into Eq. (2.4b) and integrate from the left hand side with $u^*_{\nu,\boldsymbol{k_0}}(\boldsymbol{x})$. We then obtain the following matrix equation

$$\sum_{\mu} H_{\nu\mu}(\boldsymbol{k})c_{n,\mu}(\boldsymbol{k}) = E_n(\boldsymbol{k})c_{n,\nu}(\boldsymbol{k})\,, \tag{2.8}$$

with matrix elements and interband momentum $\boldsymbol{p_{\nu\mu}}$ defined as follows

$$H_{\nu\mu}(\boldsymbol{k}) = \left\{E_\mu(\boldsymbol{k_0}) + \frac{\hbar^2}{2m_0}(\boldsymbol{k}^2 - \boldsymbol{k_0}^2)\right\}\delta_{\mu\nu} + \frac{\hbar}{m_0}(\boldsymbol{k} - \boldsymbol{k_0}) \cdot \boldsymbol{p_{\nu\mu}}\,, \tag{2.9a}$$

$$\boldsymbol{p_{\nu\mu}} = \int_\Omega \mathrm{d}^3\boldsymbol{x}\; u^*_{\nu,\,k_0}(\boldsymbol{x})\; \hat{\boldsymbol{p}}\; u_{\mu,\,k_0}(\boldsymbol{x})\,. \tag{2.9b}$$

Up to this point Eq. (2.9a) is exact and valid for all values of $\boldsymbol{k}$ in the Brillouin zone. If all energies $E_\mu(\boldsymbol{k_0})$ and interband couplings $\boldsymbol{p_{\nu\mu}}$ would be known then Eq. (2.8) could be solved directly. Unfortunately the number of matrix elements that are known from experiments is limited and including many band in calculation is numerically expensive.

We therefore treat the second term in Eq. (2.9a), $\frac{\hbar}{m_0}(\boldsymbol{k} - \boldsymbol{k_0}) \cdot \boldsymbol{p_{\nu\mu}}$, as a perturbation that couples states from different bands. This include states from both conduction and valence band, that we include directly in our model, as well as the remote bands whose effect we include only through quasi-degenerate perturbation theory.

2.1.2. QUASI-DEGENERATE PERTURBATION THEORY

Löwdin partitioning [10–13] allows us to obtain an effective model that describes selected group of the quasi-degenerate states (group A), that are weakly coupled to all other states (group B). This is an advance to the standard perturbation theory that gives us only corrections to a single nondegenerate state or a group of exactly degenerate states.

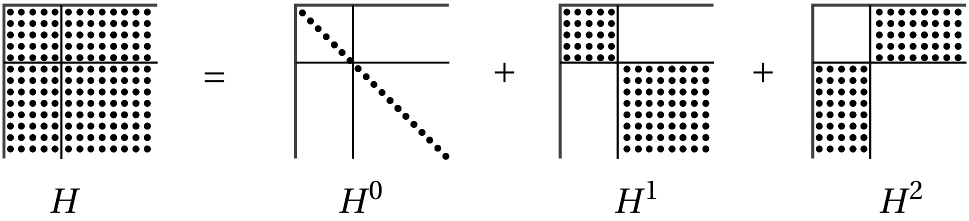

Figure 2.1: Visualisation of representation of H as $H^0 + H^1 + H^2$. First part H^0 is a diagonal matrix containing the energies E_n of all states. Second part H^1 is a block-diagonal matrix containing perturbation part of H Hamiltonian that acts only on states from groups A and B separately. And last part H^2 is non-block-diagonal matrix that corresponds perturbationm that couples states from block A and B.

Since with this method we do not need to distinguish between the degenerate and the nondegenerate states, this method is particularly useful in context of the **k·p** theory.

We will now discuss the foundations of the quasi-degenerate perturbation theory.[1] We separate Hamiltonian H into two parts

$$H = H^0 + H' . \tag{2.10}$$

The first part H^0 has known eigenstates

$$H^0 \left|\varphi_n\right\rangle = E_n \left|\varphi_n\right\rangle , \tag{2.11}$$

We treat the second part H' as a perturbation. Now, we split the eigenstates $\{\left|\varphi_n\right\rangle\}$ into two weakly interacting groups A and B. Group A contains all of the states that we want to include explicitly in our model.

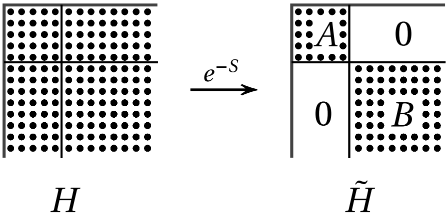

Figure 2.2: Visualisation of removal of off-diagonal elements. Hamiltonian H is transformed using unitary operator e^{-S} into Hamiltonian $\tilde{H}$ which blocks A and B are not coupled to each other.

We now split the perturbation H' into two parts H^1 and H^2. The first part corresponds to perturbation that couples only states within each group, whereas the second part is responsible for a coupling between states from groups A and B. Figure 2.1 visualizes this separation. Hamiltonian (2.10) reads now

$$H = H^0 + H^1 + H^2 . \tag{2.12}$$

Our goal now is to find a unitary operator[2] e^{-S} that gives us an effective Hamiltonian

$$\tilde{H} = e^{-s} H e^{s} , \tag{2.13}$$

---

[1] Similar discussion can be be found in R. Winkler's book, Ref. [13].

[2] Because operator e^{-S} is unitary operator S must by anti-Hermitian, i.e. $S^\dagger = -S$.

built only from the block-diagonal parts corresponding to groups A and B separately. Figure 2.2 visualizes this transformation. To find the operator S we expand e^S into a Taylor series

$$e^S = \sum_{n=0}^{\infty} \frac{1}{n!} S^n \,, \tag{2.14}$$

and substitute it into Eq. (2.13). The result is

$$\tilde{H} = \sum_{n=0}^{\infty} \frac{1}{n!} [H, S]^{(n)} = \sum_{n=0}^{\infty} \frac{1}{n!} [H^0 + H^1, S]^{(n)} + \sum_{n=0}^{\infty} \frac{1}{n!} [H^2, S]^{(n)} \,, \tag{2.15}$$

where the commutator $[A, B]^{(n)}$ is defined as

$$[A, B]^{(n)} = [\ldots[[A, \underbrace{B], B], \ldots, B]}_{n \text{ times}} . \tag{2.16}$$

This leads us to the following equations[3] for block-diagonal and non-block-diagonal parts $\tilde{H}_d$ and $\tilde{H}_n$:

$$\tilde{H}_d = \sum_{n=0}^{\infty} \frac{1}{(2n)!} [H^0 + H^1, S]^{(2n)} + \sum_{n=0}^{\infty} \frac{1}{(2n+1)!} [H^2, S]^{(2n+1)} \,, \tag{2.17a}$$

$$\tilde{H}_n = \sum_{n=0}^{\infty} \frac{1}{(2n+1)!} [H^0 + H^1, S]^{(2n+1)} + \sum_{n=0}^{\infty} \frac{1}{(2n)!} [H^2, S]^{(2n)} . \tag{2.17b}$$

To find S we make use of the fact that the non-block-diagonal part of $\tilde{H}$ must vanish, i.e. $\tilde{H}_n = 0$. We assume that S is given as a series of successive approximations

$$S = \sum_{k=1}^{\infty} S^{(k)} \,, \tag{2.18}$$

where we consider $S^{(k)}$ to be of order k. Note that from Eq. (2.17a) it follows that if we are interested in the N-th order of the perturbation we need to calculate $S^{(k)}$ up to $k_N = N - 1$ order. By substituting this ansatz into Eq. (2.17b) and grouping terms of the same order we get:

$$[H^0, S^{(1)}] = -H^2 \,, \tag{2.19a}$$

$$[H^0, S^{(2)}] = -[H^1, S^{(1)}] \,, \tag{2.19b}$$

$$[H^0, S^{(3)}] = -[H^1, S^{(2)}] - \frac{1}{3} [[H^2, S^{(1)}], S^{(1)}] \,, \tag{2.19c}$$

$$\ldots = \qquad \ldots .$$

To solve Eqs. (2.19) we multiply them with $\langle \varphi_m |$ and $| \varphi_l \rangle$ from left and right hand side, respectively, and solve for S_{ml}, starting with the the first order and use its result to

---

[3] Crucial observation here is fact that product of even (odd) number of non-block-diagonal matrices is block-diagonal (non-block-diagonal). In order to be able to remove non-block-diagonal parts of H^2 operator S must be non-block-diagonal as well.

successively find the higher order terms. The first two orders of S are as follows:

$$S^{(1)}_{ml} = -\frac{H'_{ml}}{E_m - E_l}\,, \tag{2.20a}$$

$$S^{(2)}_{ml} = \frac{1}{E_m - E_l}\left[\sum_{m'} \frac{H'_{mm'}H'_{m'l}}{E_{m'} - E_l} - \sum_{l'} \frac{H'_{ml'}H'_{l'l}}{E_m - E_{l'}}\right], \tag{2.20b}$$

$$\ldots = \ldots .$$

where m and m' corresponds to states from group A, whereas l and l' corresponds to states from group B.

We then put $S = \sum_0^{k_N} S^{(k)}$ into Eq. (2.17a) and group together terms of the same order. Explicit formula for the first two order corrections to the effective Hamiltonian are:

$$\tilde{H}^{(0)}_{mn} = H^0_{mn}\,, \tag{2.21a}$$

$$\tilde{H}^{(1)}_{mn} = H^1_{mn}\,, \tag{2.21b}$$

$$\tilde{H}^{(2)}_{mn} = \frac{1}{2}\sum_{l\in B} H^2_{ml}H^2_{ln}\left(\frac{1}{E_m - E_l} + \frac{1}{E_n - E_l}\right), \tag{2.21c}$$

$$\ldots = \ldots . \tag{2.21d}$$

In order to apply quasi-degenerate perturbation theory to the $\boldsymbol{k}$-dependent Hamiltonians, e.g. Eq. (2.5), for which $H^0 = H(\boldsymbol{k_0})$ and $H' = H(\boldsymbol{k}) - H(\boldsymbol{k_0})$, we choose perturbation basis as

$$H(\boldsymbol{k_0})\left|\varphi_\nu\right\rangle = E(\boldsymbol{k_0})\left|\varphi_\nu\right\rangle . \tag{2.22}$$

The second-order effective model can be then written as

$$\tilde{H}_{\nu\mu}(\boldsymbol{k}) = H_{\nu\mu}(\boldsymbol{k}) + \frac{1}{2}\sum_{\beta\in B} H_{\nu\beta}(\boldsymbol{k})H_{\beta\mu}(\boldsymbol{k})\left(\frac{1}{E_\nu(\boldsymbol{k_0}) - E_\beta(\boldsymbol{k_0})} + \frac{1}{E_\mu(\boldsymbol{k_0}) - E_\beta(\boldsymbol{k_0})}\right), \tag{2.23}$$

with

$$H_{\nu\mu}(\boldsymbol{k}) = \langle\varphi_\nu|H(\boldsymbol{k})|\varphi_\mu\rangle = \langle\varphi_\nu|H^0 + H'|\varphi_\mu\rangle . \tag{2.24}$$

2.2. SYMMETRY PROPERTIES OF THE ZINC-BLENDE CRYSTALS

In this section we discuss the symmetry properties of the highest valence and lowest conduction bands of III-V and II-VI semiconductors [14]. These semiconductors have a zinc-blende structure, which is built from two FCC sublattices shifted with respect to each other by a quarter of a lattice constant along the $(1,1,1)$ direction. The only difference to the diamond crystal structure is the fact that here the two sublattices are built from different kinds of atoms, whereas for the diamond structure all atoms are the same. We show both crystal structures in Fig. 2.3.

Each atom in the crystal forms tetrahedral bonds with its nearest neighbours from the other sublattice. We assume that the origin of the Cartesian coordinate system is located at an atom with the axes x, y and z being oriented along the main crystal directions. The point group of the zinc-blende crystal is isomorphic to the point group

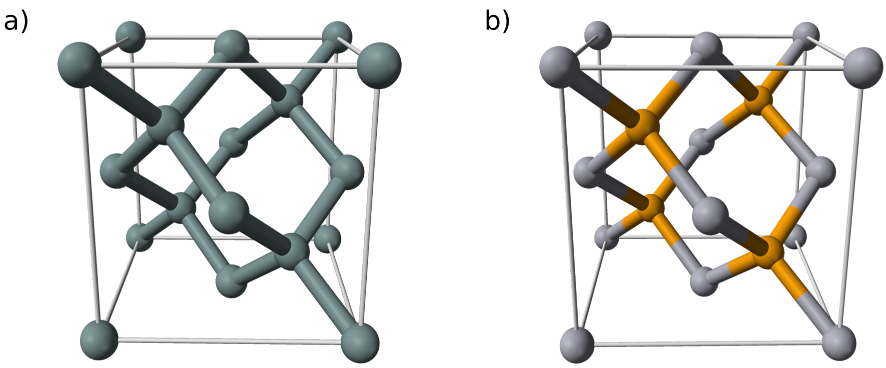

Figure 2.3: Diamond (a) and zinc-blende (b) structure. The crystals are built from two FCC sublattices that are shifted in respect to each other by a quarter of a lattice constant along $(1,1,1)$ direction. Atoms form tetrahedral bonding with their nearest neighbours. The diamond lattice is build from the atoms of the same kind. In the zinc-blende structure we have two different families of atoms, marked by grey and orange colour. Examples of semiconductors with a diamond structure are Si, Ge, and $\alpha-$Sn, while InAs, GaSb, and HgTe have a zinc-blende structure.

of the tetrahedron, denoted as T_d, that has 24 symmetry operations. Grouped by their classes, these symmetry operations are:

$\{E\}$:	identity;
$\{3\,C_2\}$:	rotation of 180° about the $[100]$, $[010]$, and $[001]$ axes;
$\{8\,C_3\}$:	clockwise and anticlockwise rotation of 120° about the $[111]$, $[\bar{1}11]$, $[1\bar{1}1]$, and $[11\bar{1}]$ axes;
$\{6\,S_4\}$:	clockwise and anticlockwise rotation of 90° about the $[100]$, $[010]$, and $[001]$ axes, followed by a reflection on the plane perpendicular to the rotation axis;
$\{6\sigma\}$:	reflection with respect to the (110), $(1\bar{1}0)$, (101), $(10\bar{1})$, (011), and $(01\bar{1})$ planes;

With every symmetry operation T we can associate a matrix $R(T)$ that represents its action on the real space position vector $\boldsymbol{x}$:

$$\boldsymbol{x}' = R(T)\boldsymbol{x}. \tag{2.25}$$

Similarly, $P(T)$ denotes the action of this operation on a scalar function

$$P(T)\varphi(\boldsymbol{x}) = \varphi(R(T)^{-1}\boldsymbol{x}). \tag{2.26}$$

Let us consider now two sets of functions: $\{\varphi_0\} = \{xyz\}$ and $\{\varphi_1, \varphi_2, \varphi_3\} = \{x, y, z\}$. The first set contains a single function that stays unchanged under all symmetry operation of T_d, i.e.

$$P(T)\varphi_0 = \varphi_0. \tag{2.27}$$

Functions of the second set, each equal to one of the Cartesian coordinates, transform under $P(T)$ as

$$P(T)\varphi_i = \sum_j R(T)_{ij}\varphi_j. \tag{2.28}$$

These two sets are examples of the basis functions of two irreducible representations of the tetrahedral group, denoted as Γ_1 and Γ_4. In general case, we can write

$$P(T)\,|\Gamma_n,i\rangle = \sum_j \Gamma_n(T)_{ji}\left|\Gamma_n,j\right\rangle, \tag{2.29}$$

where Γ_n is n-th irreducible representation of the group, $\Gamma_n(T)_{ij}$ are the matrix elements of this representation for group element T, and $\left\{|\Gamma_n,i\rangle\right\}$ is a set of the basis functions of this representation.

Irreducible representations of a group, whose number is equal to the number of classes in the group, allow us to classify all functions based on how they transform under symmetry operations. As the choice of basis functions is arbitrary—it is the symmetry of the functions that actually matters—one could for example replace the two sets we just presented with $\{s\}$ and $\{p_x, p_y, p_z\}$ orbitals. All irreducible representations of the T_d group with their basis functions are presented in Table 2.1.

Koster notation	BSW notation	Dimension	Basis functions
Γ_1	Γ_1	1	$\{1\}$ or $\{xyz\}$
Γ_2	Γ_1	1	$\{x^4(y^2-z^2)+y^4(z^2-x^2)+z^4(x^2-y^2)\}$
Γ_3	Γ_{12}	2	$\{(x^2-y^2),z^2-\frac{1}{2}(x^2+y^2)\}$
Γ_4	Γ_{15}	3	$\{x,y,z\}$
Γ_5	Γ_{25}	3	$\{x(y^2-z^2),y(z^2-x^2),z(x^2-y^2)\}$

Table 2.1: Basis function of the T_d group. Note that in Koster notation Γ_4 and Γ_5 are sometimes reversed in the literature.

2.2.1. SYMMETRY OF THE VALENCE AND THE CONDUCTION BAND

To understand what the symmetry of the valence and the conduction band is in III-V and II-VI semiconductors we will first look at a heteropolar molecule built from two different atoms, e.g. from In and As. These atoms have in total 8 valence electrons that come from s- and p-type orbitals of each atom. When the atoms are brought together, they form a molecule and their wave functions start to overlap. The overlapping wave functions form a symmetric or antisymmetric superpositions creating bonding or antibonding orbitals, respectively, as shown in Fig. 2.4 (a, b, c). The energy of bonding (antibonding) orbitals is decreased (increased) in respect to the initial energy.

The magnitude of the energy difference however depends strongly on the initial atoms forming the molecule. In InAs and GaSb for example the shift is so strong that the p bonding orbitals and s antibonding orbital switch order, Fig. 2.4 (d). Therefore in these materials the highest valence band has p-type symmetry and lowest conduction band has s-type symmetry. For HgTe, however, Fig. 2.4 (e), the energy shift of the bands is smaller and they do not change order—in this case symmetries of the highest valence and lowest conduction bands are changed compared to InAs or GaSb.

Note that in a zinc-blende crystals, the p-bonding and p-antibonding states will be formed by some nontrivial superposition of all three orbitals—each atom has four neighbours and tetrahedral bondings with them have more complicated structure than Fig. 2.4 suggests. The general properties, however, stay the same and for the purpose of

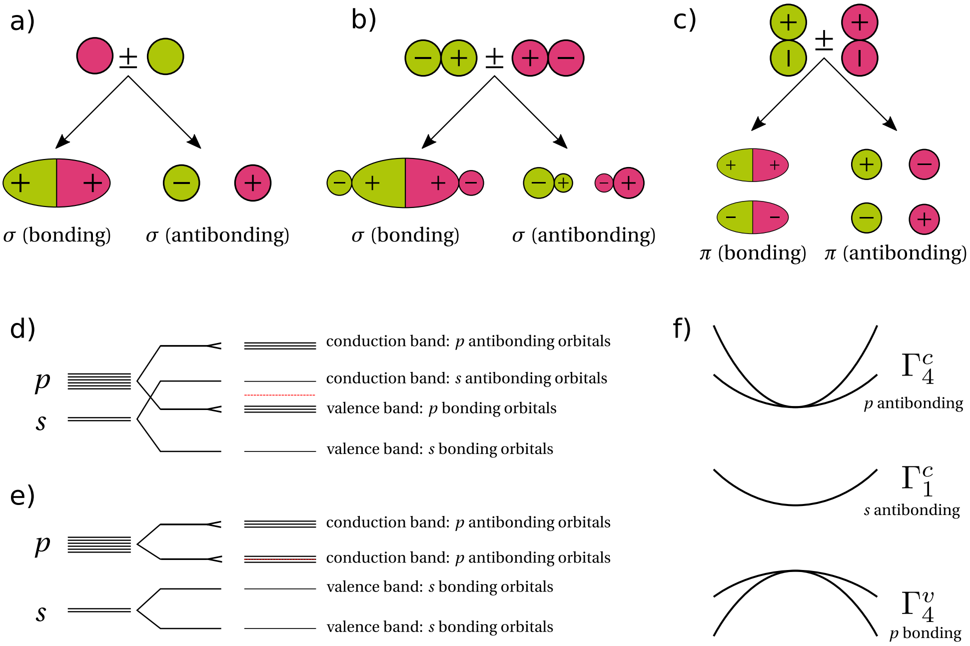

Figure 2.4: (a) σ orbitals created from s-type orbitals. (b) p-orbitals that are orientated along shared axis form σ orbitals. (c) π orbitals created for p-orbitals when they are oriented along perpendicular axis. (d) For most semiconductors, e.g. InAs, GaSb, or AlSb, p bonding and s antibonding orbitals interchange. In these materials the highest valence band has p-type symmetry and the lowest conduction band has s-type symmetry. (e) There are a few known examples of semiconductors, like HgTe or $\alpha-$Sn, for which these orbitals do not interchange—symmetries of their highest valence and lowest conduction band are therefore invert. (f) Schematic band structure, when s-type and p-type orbitals interchange, with bands classified by the irreducible representation according to which they transform.

symmetry analysis it is enough to understand how a single orbital transforms under the group operations.

As it was mentioned in previous chapter, group theory can be used to classify these bands using irreducible representations of T_d group, see Fig. 2.4 (f). The s-type states transform according to irreducible representation Γ_1, while p-type states transform according to irreducible representation Γ_4. It is important to note that momentum operator $\boldsymbol{p}$ also transforms according to irreducible representation Γ_4. From now on we will denote states from the first conduction band Γ_1^c as $|S\rangle$, whereas $|X\rangle$, $|Y\rangle$ and $|Z\rangle$ will be a notation for the states from the highest valence band Γ_4^v. The primed notation, $\left|X'\right\rangle$, $\left|Y'\right\rangle$ and $\left|Z'\right\rangle$, will be used for the states from the conduction band Γ_4^c.

2.2.2. CONSEQUENCES OF MATRIX-ELEMENT THEOREM

As it was stated in Section 2.1.1, in $\mathbf{k}\cdot\mathbf{p}$ theory we need to calculate matrix elements of the momentum operator $\boldsymbol{p}_{\mu\nu} \propto \left\langle u_\mu \right| \boldsymbol{p} \left| u_\nu \right\rangle$. This task can be significantly simplified by using one of the tools provided by group theory, called **matrix-element theorem** [8, 14]. This theorem tells us which matrix elements $\boldsymbol{p}_{\mu\nu}$ must be zero from the symmetry of the system.

Generalizing the notation, our task is to calculate matrix elements of the form

$$\left\langle \psi_i^{(\alpha)} \middle| P_j^{(\beta)} \middle| \psi_k^{(\gamma)} \right\rangle , \tag{2.30}$$

where ψ is a wave function and P is an operator. Both wave functions ψ and operator P transform according to the irreducible representation indicated by the upper index: $\Gamma^{(\alpha)}$, $\Gamma^{(\beta)}$ or $\Gamma^{(\gamma)}$. **Matrix-element theorem** stays that this product is nonzero if, and only if, the irreducible representation $\Gamma^{(\alpha)}$ appears in the reduction of the direct product $\Gamma^{(\beta)} \otimes \Gamma^{(\gamma)}$. In Table 2.2 we show the direct products of Γ^4 with all other irreducible representation of the T_d group.

Because $\boldsymbol{p}$ has Γ_4 symmetry, this simple tool can drastically limit the number of matrix elements $\boldsymbol{p}_{\mu\nu}$ that one needs to compute. For example, states with Γ_4 symmetry can only be coupled to states that have Γ_1, Γ_3, Γ_4, or Γ_5 symmetries, whereas Γ_1 states are only coupled to Γ_4 states.

Direct product	Direct sum
$\Gamma_4 \otimes \Gamma_1$	Γ_4
$\Gamma_4 \otimes \Gamma_2$	Γ_5
$\Gamma_4 \otimes \Gamma_3$	$\Gamma_4 \oplus \Gamma_5$
$\Gamma_4 \otimes \Gamma_4$	$\Gamma_1 \oplus \Gamma_3 \oplus \Gamma_4 \oplus \Gamma_5$
$\Gamma_4 \otimes \Gamma_5$	$\Gamma_2 \oplus \Gamma_3 \oplus \Gamma_4 \oplus \Gamma_5$

Table 2.2: Direct products of the Γ_4 representation with all representations of the T_d point group. Because $\boldsymbol{p}$ has Γ_4 symmetry this table gives direct information about which bands are coupled to each other, e.g. Γ_1 states are coupled only to Γ_4 states in the **k·p** theory.

2.2.3. CONSEQUENCES OF WIGNER-ECKART THEOREM

The **Wigner-Eckart** theorem [8, 15]provide us with an additional tool to minimize the number of matrix elements $\boldsymbol{p}_{\mu\nu}$ that one needs to compute. In addition to the matrix-element theorem, that only gave us information if a certain matrix element is nonzero, the Wigner-Eckart theorem can give us information which matrix elements are equal to each other.

Since point group operations leave inner products invariant, we can write

$$\left\langle \psi_i^{(\alpha)} \middle| P_j^{(\beta)} \middle| \psi_k^{(\gamma)} \right\rangle = \left\langle \Gamma^{(\alpha)}(T)_{li}\, \psi_l^{(\alpha)} \middle| \Gamma^{(\beta)}(T)_{mj}\, P_m^{(\beta)} \middle| \Gamma^{(\gamma)}(T)_{nk}\, \psi_n^{(\gamma)} \right\rangle , \tag{2.31}$$

for some symmetry operation T of the point group T_d, and Einstein summation convention is used. The usual output of this formula is either

$$\left\langle \psi_i^{(\alpha)} \middle| P_j^{(\beta)} \middle| \psi_k^{(\gamma)} \right\rangle = -\left\langle \psi_i^{(\alpha)} \middle| P_j^{(\beta)} \middle| \psi_k^{(\gamma)} \right\rangle , \tag{2.32}$$

which simply means that the respective matrix element is zero, or

$$\left\langle \psi_i^{(\alpha)} \middle| P_j^{(\beta)} \middle| \psi_k^{(\gamma)} \right\rangle = \left\langle \psi_u^{(\alpha)} \middle| P_v^{(\beta)} \middle| \psi_w^{(\gamma)} \right\rangle , \tag{2.33}$$

which indicates equality of two matrix elements.

The most important couplings in the context of the **k·p** model describing the highest valence and lowest conduction bands in a zinc-blende-type semiconductor are couplings between Γ_1 and Γ_4 states. The only nonzero matrix elements allowed by the symmetry[4] between these bands are summarized below.

$\langle \Gamma_4^c | \mathbf{k}\cdot\mathbf{p} | \Gamma_1^v \rangle$ nonzero matrix elements:

$$\langle S | p_x | X \rangle = \langle S | p_y | Y \rangle = \langle S | p_z | Z \rangle = \frac{im_0}{\hbar} P. \tag{2.34}$$

$\langle \Gamma_4^v | \mathbf{k}\cdot\mathbf{p} | \Gamma_4^c \rangle$ nonzero matrix elements:

$$\begin{aligned} \langle X | p_y | Z' \rangle = \langle Y | p_z | X' \rangle = \langle Z | p_x | Y' \rangle = \frac{im_0}{\hbar} Q, \\ \langle X | p_z | Y' \rangle = \langle Y | p_x | Z' \rangle = \langle Z | p_y | X' \rangle = \frac{im_0}{\hbar} Q, \end{aligned} \tag{2.35}$$

where primed and non-primed indices corresponds to wave functions of Γ_4^c and Γ_4^v states, respectively. Note that matrix elements between states from the same band are zero, e.g. $\langle X | p_y | Z \rangle = 0$.

2.3. **k·p** MODELS FOR CONDUCTION AND VALENCE BAND

Now that we understand the symmetry of the highest valence and the lowest conduction band in the zinc-blende-type semiconductors, we write the Hamiltonian that describes dispersion of these bands at the Γ point of the Brillouin zone, i.e. $\boldsymbol{k_0} = 0$.

In Chapter 2.3.1, we start with a single band model that describes the $|S\rangle$ states of the conduction band Γ_1^c. In Chapter 2.3.2, we continue with a 3−band model, that describes the dispersion of the valence band states $|X\rangle$, $|Y\rangle$, and $|Z\rangle$. In Chapter 2.3.3 and Chapter 2.3.4 we introduce spin-orbit coupling that partially removes degeneracy of Γ_4^v states and **k·p**-coupling between conduction and valence states, respectively. Finally, in Chapter 2.3.5 we present the Burt-Foreman symmetrization that extends these models to systems that are composed of more than one material. We conclude this section in Chapter 2.3.6 where we present a full 8 × 8 band Kane Hamiltonian that describes the dispersion of both Γ_1^c electrons and Γ_4^v holes.

---

[4] As an example we consider in detail matrix elements of $\boldsymbol{p}$ between p-states. First, let us note that we can choose wave functions to be real without loss of generality, therefore because $\boldsymbol{p} = -\mathrm{i}\nabla$ the matrix elements are purely imaginary. Second, all p-type states must come from different bands. To see that let us consider symmetry operation σ_{101} that changes $xyz \to \bar{z}y\bar{x}$; one can immediately see that $\langle X|p_y|Z\rangle = \langle Z|p_y|X\rangle = \left(\langle X|p_y|Z\rangle\right)^* = 0$, because matrix elements are purely imaginary. Now, all coordinate indices that are present must be unique. It can be seen from analysing action of C_2 symmetry operation that switches sign of two coordinates, e.g. $xyz \to x\bar{y}\bar{z}$, and $\langle X|p_z|Z'\rangle = -\langle X|p_z|Z'\rangle = 0$. Finally, we observe that C_3 symmetry operation cyclically permutes all coordinates and therefore $\langle X|p_y|Z'\rangle = \langle Y|p_z|X'\rangle = \langle Z|p_x|Y'\rangle$, and from σ operations we have e.g. $\langle X|p_y|Z'\rangle = \langle X|p_z|Y'\rangle$.

The derivation of all models is based on Eq. (2.9a) and Eq. (2.9b), which we for convenience repeat here

$$H_{\nu\mu} = \left\{ E_\mu(\boldsymbol{k_0}) + \frac{\hbar^2}{2m_0}(\boldsymbol{k}^2 - \boldsymbol{k_0}^2) \right\} \delta_{\mu\nu} + \frac{\hbar}{m_0}(\boldsymbol{k} - \boldsymbol{k_0}) \cdot \boldsymbol{p_{\nu\mu}}\,, \tag{2.9a}$$

$$\boldsymbol{p_{\nu\mu}} = \int_\Omega \mathrm{d}^3\boldsymbol{x}\; u^*_{\nu,k_0}(\boldsymbol{x})\, \hat{\boldsymbol{p}}\, u_{\mu,k_0}(\boldsymbol{x})\,. \tag{2.9b}$$

These equations describe the **k·p** Hamiltonian that couples an infinite amount of bands through the matrix elements $\boldsymbol{p_{\nu\mu}}$. The effective Hamiltonian for the bands of interest will be obtained through the second-order quasi-degenerate perturbation theory, Eq. (2.23):

$$\tilde{H}_{\nu\mu}(\boldsymbol{k}) = H_{\nu\mu}(\boldsymbol{k}) + \frac{1}{2}\sum_{\beta\in B} H_{\nu\beta}(\boldsymbol{k}) H_{\beta\mu}(\boldsymbol{k}) \left(\frac{1}{E_\nu(\boldsymbol{k_0}) - E_\beta(\boldsymbol{k_0})} + \frac{1}{E_\mu(\boldsymbol{k_0}) - E_\beta(\boldsymbol{k_0})} \right). \tag{2.23}$$

Indices ν and μ correspond to states in group A—states that are explicitly present in our model—whereas indices β correspond to states in group B—all other states which influence we include only through perturbation theory.

2.3.1. EFFECTIVE MASS APPROXIMATION

We now consider the single band model for the $|S\rangle$ state of the Γ_1^c band. From the matrix-element theorem we know that the Γ_1 band is coupled, through the **k·p** term, only with the Γ_4 states. From Eq. (2.23) we obtain

$$E_c(\boldsymbol{k}) = E_c + \frac{\hbar^2 k^2}{2m_0} + \frac{\hbar^2}{m_0^2} \sum_{\beta\in\Gamma_4} \frac{\left|\langle S|\,\mathbf{k{\cdot}p}\,|u_\beta\rangle\right|^2}{E_c - E_\beta}\,, \tag{2.36}$$

where $\langle \boldsymbol{x}|u_\beta\rangle = u_{\beta,\boldsymbol{k_0}}(\boldsymbol{x})$ and E_c is the band edge of the Γ_1^c band. This relation can be rewritten as

$$E_c(\boldsymbol{k}) = E_c + \frac{\hbar^2 k^2}{2m_c}\,, \tag{2.37a}$$

$$\frac{1}{m_c} = \frac{1}{m_0} + \sum_{\beta\in\Gamma_4} \frac{2\left|\langle S|\mathbf{k{\cdot}p}|u_\beta\rangle\right|^2}{m_0^2 k^2 (E_c - E_\beta)}\,, \tag{2.37b}$$

and is known as effective mass approximation.

Because the strength of the interband interaction is inversely proportional to the energy difference $E_c - E_\beta$, the most significant contribution comes from the nearest Γ_4 bands from both conduction and valence band. In a diamond structure, due to the parity selection rule, matrix elements with the Γ_4^c states are exactly zero, but even in zinc-blende-type semiconductors it is much smaller than matrix elements with the Γ_4^v states. We can therefore limit the sum in Eq. (2.37b) to $\beta \in \Gamma_4^v$. By taking into account Eq. (2.34) we have

$$\frac{m_0}{m_c} \approx 1 + \frac{E_p}{E_0}\,, \tag{2.38}$$

where

$$E_p = \frac{2m_0 P^2}{\hbar^2}\,. \tag{2.39}$$

As it is pointed in Ref. [14], P is more or less constant for most group IV, III-V and II-VI semiconductors, with $E_p \approx 20\,\text{eV}$. In Table 2.3 we present theoretical values compared to the experiment.

	Ge	GaN	GaAs	GaSb	InP	InAs	ZnTe	CdTe
E_0 [eV] (exp)	0.89	3.44	1.55	0.81	1.34	0.45	2.39	1.59
m_c/m_0 (exp)	0.041	0.17	0.067	0.047	0.073	0.026	0.124	0.093
m_c/m_0 (theory)	0.04	0.17	0.078	0.04	0.067	0.023	0.12	0.08

Table 2.3: Γ_1^c conduction band effective masses in chosen diamond and zinc-blende-type semiconductors. Theoretical values are calculated with Eq. (2.38) using the values of E_0 obtained from Ref. [16] compared with experimental values. Adopted from Ref. [14]

2.3.2. THE DRESSELHAUS-KIP-KITTEL MODEL

Now we will take a look at the 3−band model, known as Dresselhaus-Kip-Kittel model [5, 17]. This model descibes holes in Γ_4^v band. Neglecting spin, the basis for the Hamiltonian is

$$\Big\{ |X\rangle\,,|Y\rangle\,,|Z\rangle \Big\}. \tag{2.40}$$

We neglect spin in order to preserve clarity of the discussion. We include it in the next chapter, where we discuss consequences of spin-orbit coupling.

From Table 2.2, we know that this band couples through the **k·p** term only to Γ_1, Γ_3, Γ_4, and Γ_5 bands. The nonzero matrix elements with the Γ_1^c and the Γ_4^c bands are given by Eq. (2.34) and Eq. (2.35), and are equal to $\frac{im}{\hbar}P$ and $\frac{im}{\hbar}Q$, respectively. Ignoring for a moment interactions with Γ_3 and Γ_5, from Eq (2.9a), (2.9b) and Eq. (2.23) we obtain

$$H_{vv}^{3\times3}(\boldsymbol{k}) = E_v + \frac{\hbar^2 k^2}{2m_0} + \begin{pmatrix} Lk_x^2 + M(k_y^2+k_z^2) & Nk_xk_y & Nk_xk_z \\ Nk_xk_y & Lk_y^2 + M(k_x^2+k_z^2) & Nk_yk_z \\ Nk_xk_z & Nk_yk_z & Lk_z^2 + M(k_x^2+k_y^2) \end{pmatrix}, \tag{2.41}$$

where

$$L = -\frac{\hbar^2 P^2}{m_0^2 E_0}, \quad M = -\frac{\hbar^2 Q^2}{m_0^2 E_0}, \quad N = L + M. \tag{2.42}$$

When all interactions are taken into account the form of Eq. (2.41) remains unchanged and Dresselhaus-Kip-Kittel parameters L, M, and N are then defined as:

$$L = F + 2G\,, \tag{2.43a}$$

$$M = H_1 + H_2\,, \tag{2.43b}$$

$$N = N_+ + N_-\,, \tag{2.43c}$$

$$N_+ = F - G\,, \tag{2.43d}$$

$$N_- = H_1 - H_2\,, \tag{2.43e}$$

$$F = \frac{\hbar^2}{m_0^2}\sum_\beta^{\Gamma_1}\frac{|\langle X|p_x|u_\beta\rangle|^2}{E_v - E_\beta}\,, \tag{2.43f}$$

$$G = \frac{1}{2}\frac{\hbar^2}{m_0^2}\sum_\beta^{\Gamma_3}\frac{|\langle X|p_x|u_\beta\rangle|^2}{E_v - E_\beta}\,, \tag{2.43g}$$

$$H_1 = \frac{\hbar^2}{m_0^2}\sum_\beta^{\Gamma_4}\frac{|\langle X|p_x|u_\beta\rangle|^2}{E_v - E_\beta}\,, \tag{2.43h}$$

$$H_2 = \frac{\hbar^2}{m_0^2}\sum_\beta^{\Gamma_5}\frac{|\langle X|p_x|u_\beta\rangle|^2}{E_v - E_\beta}\,. \tag{2.43i}$$

Another set of parameters that are commonly used in **k·p**-theory are the Luttinger parameters [18] γ_1, γ_2, γ_3, and κ that are related to the Dresselhaus-Kip-Kittel parameters by the following relations [5]:

$$L = (-\gamma_1 - 4\gamma_2 - 1)\frac{\hbar^2}{2m_0}\,, \tag{2.44a}$$

$$M = (2\gamma_2 - \gamma_1 - 1)\frac{\hbar^2}{2m_0}\,, \tag{2.44b}$$

$$N_+ = (-3\gamma_3 - (3\kappa + 1))\frac{\hbar^2}{2m_0}\,, \tag{2.44c}$$

$$N_- = (-3\gamma_3 + (3\kappa + 1))\frac{\hbar^2}{2m_0}\,. \tag{2.44d}$$

2.3.3. SPIN-ORBIT COUPLING

After including spin, the basis (2.40) takes following form

$$\left\{|X\uparrow\rangle, |Y\uparrow\rangle, |Z\uparrow\rangle, |X\downarrow\rangle, |Y\downarrow\rangle, |Z\downarrow\rangle\right\}. \tag{2.45}$$

These six wave functions are degenerate at the Γ point of the Brillouin zone. This degeneracy will be partially removed if we now include the spin-orbit coupling. The spin-orbit coupling is included in the Hamiltonian by adding the following term [5, 13]

$$H_{so} = \frac{\hbar}{4m_0^2c^2}\left(\nabla V_0 \times \boldsymbol{p}\right)\cdot\boldsymbol{\sigma}\,. \tag{2.46}$$

In the basis of (2.45), first order perturbation theory gives [5, 19]

$$H_{so}^{6\times6} = \frac{\Delta_0}{3}\begin{pmatrix} 0 & -\mathrm{i} & 0 & 0 & 0 & 1 \\ \mathrm{i} & 0 & 0 & 0 & 0 & -\mathrm{i} \\ 0 & 0 & 0 & -1 & \mathrm{i} & 0 \\ 0 & 0 & -1 & 0 & \mathrm{i} & 0 \\ 0 & 0 & -\mathrm{i} & -\mathrm{i} & 0 & 0 \\ 1 & \mathrm{i} & 0 & 0 & 0 & 0 \end{pmatrix}, \tag{2.47}$$

with matrix element Δ_0 defined as

$$\Delta_0 = -3\mathrm{i}\left(\frac{h}{4m_0^2c^2}\right)\langle X|\left(\nabla V_0 \times \boldsymbol{p}\right)_y|Y\rangle\,. \tag{2.48}$$

The total Hamiltonian for Γ_4^v that includes spin and spin-orbit interaction takes following form

$$H_{vv}^{6\times6} = \begin{pmatrix} H_{vv}^{3\times3} & 0 \\ 0 & H_{vv}^{3\times3} \end{pmatrix} + H_{so}^{6x6}\,. \tag{2.49}$$

Because in atomic physics spin-orbit interaction can be expressed in terms of $\boldsymbol{l}$ and $\boldsymbol{s}$ as

$$H_{so} = \lambda\boldsymbol{l}\cdot\boldsymbol{s}\,, \tag{2.50}$$

one can choose a more appropriate basis for the Hamiltonian that diagonalizes the spin-orbit interaction:

$$\left|\frac{3}{2},\frac{3}{2}\right\rangle = \frac{1}{\sqrt{2}}\left|\begin{matrix} X+\mathrm{i}Y \\ 0 \end{matrix}\right\rangle, \tag{2.51a}$$

$$\left|\frac{3}{2},\frac{1}{2}\right\rangle = \frac{1}{\sqrt{6}}\left|\begin{matrix} -2Z \\ X+\mathrm{i}Y \end{matrix}\right\rangle, \tag{2.51b}$$

$$\left|\frac{3}{2},-\frac{1}{2}\right\rangle = -\frac{1}{\sqrt{6}}\left|\begin{matrix} X-\mathrm{i}Y \\ +2Z \end{matrix}\right\rangle, \tag{2.51c}$$

$$\left|\frac{3}{2},-\frac{3}{2}\right\rangle = -\frac{1}{\sqrt{2}}\left|\begin{matrix} 0 \\ X-\mathrm{i}Y \end{matrix}\right\rangle, \tag{2.51d}$$

$$\left|\frac{1}{2},\frac{1}{2}\right\rangle = \frac{1}{\sqrt{3}}\left|\begin{matrix} Z \\ X+\mathrm{i}Y \end{matrix}\right\rangle, \tag{2.51e}$$

$$\left|\frac{1}{2},-\frac{1}{2}\right\rangle = \frac{1}{\sqrt{3}}\left|\begin{matrix} X-\mathrm{i}Y \\ -Z \end{matrix}\right\rangle. \tag{2.51f}$$

The spin-orbit part of the Hamiltonian, Eq. (2.47), reads now

$$H_{so}^{6\times6} = \frac{\Delta_0}{3}\begin{pmatrix} 1 & & & & & \\ & 1 & & & & \\ & & 1 & & & \\ & & & 1 & & \\ & & & & -2 & \\ & & & & & -2 \end{pmatrix}. \tag{2.52}$$

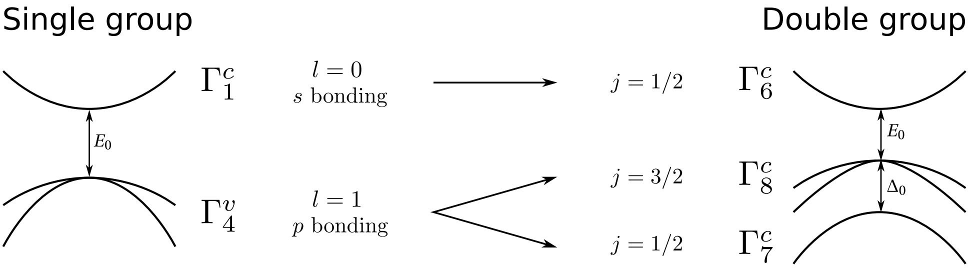

Figure 2.5: Bands of a single and double T_d point group. When spin-orbit interaction is included Γ_4 bands split into Γ_7 and Γ_8 bands. These new bands are characterized by the total momentum, $J = L + S$, with $s = 1/2$ coming from the electron's spin. Notation of irreducible representations of the T_d point group follows the one of Koster.

These are the eigenstates of total-momentum operator $J = L + S$, denoted as $|j, m_j\rangle$. The spin-orbit induced splitting $\Delta_0 = 3\lambda/2$ partially removes the degeneracy in the valence band states. Energy of the $j = 3/2$ states is increased to the new valence band edge $E_v + \Delta_0/3$, whereas energy of the $j = 1/2$ states is lowered to $E_v - \frac{2\Delta_0}{3}$. It is however customary to still denote the band gap between conduction and valence band as E_0 and treat energy of the $j = 3/2$ states as new band edge of the valence band states. After including the spin, the symmetry character of these states changes and it is common to classify them using a double group notation that we present in Fig. 2.5.

The $j = 3/2$ states with $m_j = \pm 3/2$ and $m_j = \pm 1/2$ are known as heavy-hole and light-hole bands, respectively, because of the significant difference in their effective masses around the Γ point of the Brillouin zone. The $j = 1/2$ states are known as split-off-hole band. In Table 2.4 we give effective masses of these states in term of Luttinger parameters [12, 20].

	[001]	[110]	[111]
$\frac{m_0}{m_{hh}}$	$\gamma_1 - 2\gamma_2$	$\gamma_1 - \frac{1}{2}\left(\gamma_2 + 3\gamma_3\right)$	$\gamma_1 - 2\gamma_3$
$\frac{m_0}{m_{lh}}$	$\gamma_1 + 2\gamma_2$	$\gamma_1 + \frac{1}{2}\left(\gamma_2 + 3\gamma_3\right)$	$\gamma_1 + 2\gamma_3$
$\frac{m_0}{m_{soh}}$	$\gamma_1 - \frac{1}{3}\frac{E_p}{E_0}\frac{\Delta_0}{E_0+\Delta_0}$		

Table 2.4: Effective mass of the heavy-hole, light-hole and split-off-hole states along crystallographic directions [001], [110], and [111].

2.3.4. CONDUCTION-VALENCE BAND COUPLING

In many physical scenarios, a model that describes only conduction or valence band dispersion is not sufficient, e.g. broken-gap system of a InAs/GaSb heterostructure. In such situation we include explicitly both the conduction (2.36) and the valence band (2.41) states in our model, and obtain effectively 8-band Hamiltonian. The conduction-valence band coupling, in basis

$$\Big\{|S\rangle\,,|X\rangle\,,|Y\rangle\,,|Z\rangle\Big\}, \tag{2.53}$$

is obtained via second-order perturbation (2.23)

$$H_{4\times4}(\boldsymbol{k}) = \left(\begin{array}{c|ccc} E_c(\boldsymbol{k}) & \mathrm{i}Pk_x + Bk_yk_z & \mathrm{i}Pk_y + Bk_xk_z & \mathrm{i}Pk_z + Bk_xk_y \\ \hline -\mathrm{i}Pk_x + Bk_yk_z & & & \\ -\mathrm{i}Pk_y + Bk_xk_z & & H_{vv}^{3x3}(\boldsymbol{k}) & \\ -\mathrm{i}Pk_z + Bk_xk_y & & & \end{array}\right). \tag{2.54}$$

The B term comes from the interaction with the Γ_4 bands

$$B = \frac{\hbar^2}{2m_0^2}\sum_{\beta\in\Gamma_4}\langle s|p_x|u_\beta\rangle\langle u_\beta|p_y|Z\rangle\left(\frac{1}{E_0+E_v-E_\beta(\boldsymbol{k_0})}+\frac{1}{E_v-E_\beta(\boldsymbol{k_0})}\right), \tag{2.55}$$

and is known as the Dresselhaus term. It will be ignored in further discussion due to its small impact on the analysed systems.

In a basis that includes spin

$$\Big\{|S\uparrow\rangle\,,|S\downarrow\rangle\,,|X\uparrow\rangle\,,|Y\uparrow\rangle\,,|Z\uparrow\rangle\,,|X\downarrow\rangle\,,|Y\downarrow\rangle\,,|Z\downarrow\rangle\Big\}. \tag{2.56}$$

the conduction-valence band coupling takes the following form

$$H_{8\times8}(\boldsymbol{k}) = \left(\begin{array}{cc|cccccc} \multicolumn{2}{c|}{H_{cc}^{2\times2}(\boldsymbol{k})} & \mathrm{i}Pk_x & \mathrm{i}Pk_y & \mathrm{i}Pk_z & 0 & 0 & 0 \\ & & 0 & 0 & 0 & \mathrm{i}Pk_x & \mathrm{i}Pk_y & \mathrm{i}Pk_z \\ \hline -\mathrm{i}Pk_x & 0 & & & & & & \\ -\mathrm{i}Pk_y & 0 & & & & & & \\ -\mathrm{i}Pk_z & 0 & & & & & & \\ 0 & -\mathrm{i}Pk_x & & & H_{vv}^{6x6}(\boldsymbol{k}) & & & \\ 0 & -\mathrm{i}Pk_y & & & & & & \\ 0 & -\mathrm{i}Pk_z & & & & & & \end{array}\right), \tag{2.57}$$

where $H_{cc}^{2\times2} = E_c(\boldsymbol{k})\,\mathbf{I}_{2\times2}$ and $H_{vv}^{6x6}(\boldsymbol{k})$ are given by Eq. (2.37a) and Eq. (2.49), respectively. Because the Γ_4^c is now included explicitly, the Dresselhaus-Kip-Kittel parameters L, N, and F present in $H_{vv}^{6x6}(\boldsymbol{k})$ must be modified

$$L' \to L + \frac{P^2}{E_0}\,, \quad N' \to N + \frac{P^2}{E_0}\,, \quad F' \to F + \frac{P^2}{E_0}\,. \tag{2.58}$$

To obtain the correct effective mass m_c the Γ_4^v band must be now excluded from the sum (2.37b). However, the effective mass m_c is usually known from the experiment, and it is therefore more practical to modify its value, before inserting into Eq. (2.57), as

$$\frac{m_0}{m_c'} = \frac{m_0}{m_c} - \frac{2}{3}\frac{E_P}{E_0} - \frac{1}{3}\frac{E_p}{E_0+\Delta_0}\,, \tag{2.59}$$

where $E_p = \frac{2m_0P^2}{\hbar^2}$. The other parameters stay the same, i.e.

$$M' = M\,, \quad G' = G\,, \quad H_1' = H_1\,, \quad H_2' = H_2\,. \tag{2.60}$$

2.3.5. BURT-FOREMAN SYMMETRIZATION

The material parameters in the Hamiltonian become position-dependent if the system has a layered structure, like in two-dimensional quantum wells. The Bloch momentum $\boldsymbol{k}$ is now considered as the differential operator $\boldsymbol{k} = -\mathrm{i}\nabla_{\boldsymbol{x}}$ rather than a scalar. In this situation, the Hamiltonian (2.57) is no longer Hermitian and great care has to be taken to symmetrize it in order to treat the interface between different materials properly. In this thesis we follow the approach put forward by Burt and Foreman [21, 22], that we summarize in this chapter.

Diagonal terms in $H_{vv}^{6\times 6}$ and $H_{cc}^{2\times 2}$: The diagonal terms, e.g. Mk_x^2, are symmetrized according to usual principle

$$Mk_x^2 \rightarrow k_x M k_x \,, \tag{2.61}$$

for both valence and conduction bands.

Off-diagonal terms in $H_{vv}^{6\times 6}$: The off-diagonal terms, e.g. $H_{XY} = H_{YX} = N' k_x k_y$, are symmetrized in following way

$$H_{XY} \rightarrow k_x N'_+ k_y + k_y N_- k_x \,, \tag{2.62a}$$

$$H_{YX} \rightarrow k_y N'_+ k_x + k_x N_- k_y \,. \tag{2.62b}$$

Here $N'_+ = F' - G$ is the contribution to N' from Γ_1 and Γ_3, while $N_- = H_1 - H_2$ is that from Γ_4 and Γ_5.

Conduction-valence band coupling: The conduction valence band couplings, e.g. $\mathrm{i}Pk_x$, is symmetrized in the following way

$$\begin{pmatrix} & \mathrm{i}Pk_x \\ -\mathrm{i}Pk_x & \end{pmatrix} \rightarrow \begin{pmatrix} & \mathrm{i}Pk_x \\ -\mathrm{i}k_x P & \end{pmatrix} . \tag{2.63}$$

2.3.6. 8 × 8 KANE HAMILTONIAN

We now give form of a full 8-band **k·p** Hamiltonian for a two-dimensional heterostructure with the [001] growth direction. We make use of the Burt-Foreman symmetrization and use basis that diagonalize the spin-orbit interaction (2.51). The Hamiltonian reads [23, 24]:

$$H^{8\times 8}_{\mathbf{k}\cdot\mathbf{p}} = \begin{pmatrix}
T & 0 & -\frac{1}{\sqrt{2}}Pk_+ & \sqrt{\frac{2}{3}}Pk_z & \frac{1}{\sqrt{6}}Pk_- & 0 & -\frac{1}{\sqrt{3}}Pk_z & -\frac{1}{\sqrt{3}}Pk_-\,, \\
0 & T & 0 & -\frac{1}{\sqrt{6}}Pk_+ & \sqrt{\frac{2}{3}}Pk_z & \frac{1}{\sqrt{2}}Pk_- & -\frac{1}{\sqrt{3}}Pk_+ & \frac{1}{\sqrt{3}}Pk_z\,, \\
-\frac{1}{\sqrt{2}}k_-P & 0 & U+V & -\overline{S}_- & R & 0 & \frac{1}{\sqrt{2}}\overline{S}_- & -\sqrt{2}R\,, \\
\sqrt{\frac{2}{3}}k_zP & -\frac{1}{\sqrt{6}}k_-P & -\overline{S}^\dagger_- & U-V & C & R & \sqrt{2}V & -\sqrt{\frac{3}{2}}\widetilde{S}_-\,, \\
\frac{1}{\sqrt{6}}k_+P & \sqrt{\frac{2}{3}}k_zP & R^\dagger & C^\dagger & U-V & \overline{S}^\dagger_+ & -\sqrt{\frac{3}{2}}\widetilde{S}_+ & -\sqrt{2}V\,, \\
0 & \frac{1}{\sqrt{2}}k_+P & 0 & R^\dagger & \overline{S}_+ & U+V & \sqrt{2}R^\dagger & \frac{1}{\sqrt{2}}\overline{S}_+\,, \\
-\frac{1}{\sqrt{3}}k_zP & -\frac{1}{\sqrt{3}}k_-P & \frac{1}{\sqrt{2}}\overline{S}^\dagger_- & \sqrt{2}V & -\sqrt{\frac{3}{2}}\widetilde{S}^\dagger_+ & \sqrt{2}R & U-\Delta_0 & C\,, \\
-\frac{1}{\sqrt{3}}k_+P & \frac{1}{\sqrt{3}}k_zP & -\sqrt{2}R^\dagger & -\sqrt{\frac{3}{2}}\widetilde{S}^\dagger_- & -\sqrt{2}V & \frac{1}{\sqrt{2}}\overline{S}^\dagger_+ & C^\dagger & U-\Delta_0\,,
\end{pmatrix}, \tag{2.64}$$

where

$$k_\parallel^2 = k_x^2 + k_y^2, \quad k_\pm = k_x \pm i k_y, \quad k_z = -i\partial/\partial z,$$

$$\begin{aligned}
T &= E_0 + E_v + \frac{\hbar^2}{2m_0}\left(\gamma_0' k_\parallel^2 + k_z\gamma_0' k_z\right), \\
U &= E_v - \frac{\hbar^2}{2m_0}\left(\gamma_1' k_\parallel^2 + k_z\gamma_1' k_z\right), \\
V &= -\frac{\hbar^2}{2m_0}\left(\gamma_2' k_\parallel^2 - 2k_z\gamma_2' k_z\right), \\
R &= -\frac{\hbar^2}{2m_0}\frac{\sqrt{3}}{2}\left[(\gamma_3' - \gamma_2')k_+^2 - (\gamma_3' + \gamma_2')k_-^2\right], \\
\overline{S}_\pm &= -\frac{\hbar^2}{2m_0}\sqrt{3}k_\pm\left(\{\gamma_3', k_z\} + [\kappa', k_z]\right), \\
\widetilde{S}_\pm &= -\frac{\hbar^2}{2m_0}\sqrt{3}k_\pm\left(\{\gamma_3', k_z\} - \frac{1}{3}[\kappa', k_z]\right), \\
C &= \frac{\hbar^2}{m_0}k_-\left[\kappa', k_z\right].
\end{aligned}$$

Here $[A,B] = AB - BA$ is the commutator and $\{A,B\} = AB + BA$ is the anticommutator for the operators A and B, E_v is the valence band offset, Δ_0 is the spin-orbit induced splitting

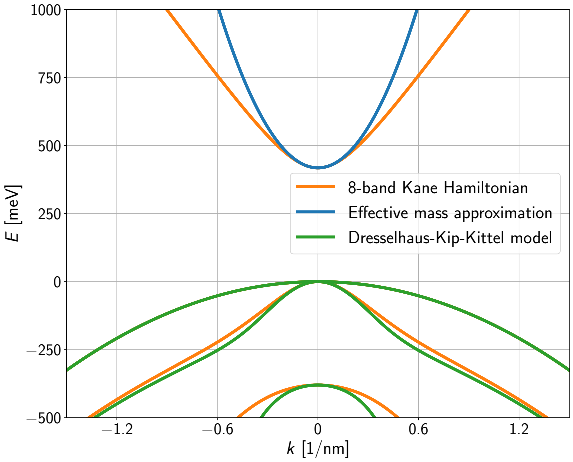

Figure 2.6: Band structure of bulk InAs calculated using three different models: (blue) the effective mass approximation for the conduction band $\Gamma_6 c$, (green) the Dresselhaus-Kip-Kittel model for heavy- light- and split-of-holes of $\Gamma_8 v$ and $\Gamma_7 v$ bands, and (orange) the 8-band Kane Hamiltonian for all bands.

in the valence band states, and E_0 is the band gap between conduction and valence band states. γ_0', γ_1', γ_2', γ_3' and κ' are the bare parameters entering the 8×8 Hamiltonian. They are related to the effective mass of the conduction band (m_c) and the Luttinger parameters of the hole bands ($\gamma_{1,2,3}$ and κ) through

$$\gamma_0' = \gamma_0 - \frac{E_P}{E_0}\frac{E_0 + \frac{2}{3}\Delta_0}{E_0 + \Delta_0}, \tag{2.65a}$$

$$\gamma_1' = \gamma_1 - \frac{1}{3}\frac{E_P}{E_0}, \tag{2.65b}$$

$$\gamma_2' = \gamma_2 - \frac{1}{6}\frac{E_P}{E_0}, \tag{2.65c}$$

$$\gamma_3' = \gamma_3 - \frac{1}{6}\frac{E_P}{E_0}, \tag{2.65d}$$

$$\kappa' = \kappa - \frac{1}{6}\frac{E_P}{E_0}, \tag{2.65e}$$

where

$$E_P = \frac{2m_0P^2}{\hbar^2}, \quad \gamma_0 = \frac{m_0}{m_c}, \quad \gamma_0' = \frac{m_0}{m_c'}, \tag{2.66}$$

and E_0 is the band gap. All of these parameters are material dependent and hence a function of the z-coordinate. The order of operators in Eq. (2.64) follow the one presented in Section. 2.3.5 and guarantee that Hamiltonian is indeed Hermitian and properly symmetrized.

As an example, we show in Fig. 2.6 the band structure bulk InAs calculated using three different models: the effective mass approximation for the conduction band $\Gamma_6 c$, the

Dresselhaus-Kip-Kittel model for heavy- light- and split-of-holes of $\Gamma_8 v$ and $\Gamma_7 v$ bands, and the 8-band Kane Hamiltonian for all bands.

Magnetic field is included through the Zeeman and the orbital effect. The **k·p** Zeeman term [13] is

$$\begin{aligned} H^z_{6c6c} &= \frac{1}{2} g' \mu_B \boldsymbol{\sigma} \cdot \boldsymbol{B}, \\ H^z_{8v8v} &= -2\mu_B \kappa' \boldsymbol{J} \cdot \boldsymbol{B}, \\ H^z_{7v7v} &= -2\mu_B \kappa' \boldsymbol{\sigma} \cdot \boldsymbol{B}, \\ H^z_{8v7v} &= -3\mu_B \kappa' \boldsymbol{U} \cdot \boldsymbol{B}, \end{aligned} \tag{2.67}$$

where $\boldsymbol{\sigma}$ is a vector of Pauli matrices, $U = T^\dagger$, and

$$T_x = \frac{1}{3\sqrt{2}} \begin{pmatrix} -\sqrt{3} & 0 & 1 & 0 \\ 0 & -1 & 0 & \sqrt{3} \end{pmatrix}, \tag{2.68a}$$

$$T_y = \frac{-\mathrm{i}}{3\sqrt{2}} \begin{pmatrix} \sqrt{3} & 0 & 1 & 0 \\ 0 & 1 & 0 & \sqrt{3} \end{pmatrix}, \tag{2.68b}$$

$$T_z = \frac{\sqrt{2}}{3} \begin{pmatrix} 0 & 1 & 0 & 0 \\ 0 & 0 & 1 & 0 \end{pmatrix}, \tag{2.68c}$$

$$J_x = \frac{1}{2} \begin{pmatrix} 0 & \sqrt{3} & 0 & 0 \\ \sqrt{3} & 0 & 2 & 0 \\ 0 & 2 & 0 & \sqrt{3} \\ 0 & 0 & \sqrt{3} & 0 \end{pmatrix}, \tag{2.68d}$$

$$J_y = \frac{\mathrm{i}}{2} \begin{pmatrix} 0 & -\sqrt{3} & 0 & 0 \\ \sqrt{3} & 0 & -2 & 0 \\ 0 & 2 & 0 & -\sqrt{3} \\ 0 & 0 & \sqrt{3} & 0 \end{pmatrix}, \tag{2.68e}$$

$$J_z = \frac{1}{2} \begin{pmatrix} 3 & 0 & 0 & 0 \\ 0 & 1 & 0 & 0 \\ 0 & 0 & -1 & 0 \\ 0 & 0 & 0 & -3 \end{pmatrix}. \tag{2.68f}$$

We include the orbital effect by making a following substitution in the Hamiltonian

$$\boldsymbol{k} \to \boldsymbol{k} + \frac{2\pi}{\phi_0} \boldsymbol{A}, \tag{2.69}$$

where $\boldsymbol{A}$ is the vector potential and $\phi_0 = \frac{h}{e}$ is the flux quantum. This method gives the same results as using Peierl's substitution on the tight-binding level in the regime of simulation parameters used this thesis. For the in-plane magnetic fields the vector potential reads

$$\boldsymbol{A} = \left(B_y(z-z_0)\,,-B_x(z-z_0)\,,0\right)\,. \tag{2.70}$$

In simulation included in this thesis we adopt parameters from [23–26], presented in Table 2.5 and Table 2.6. We calculate the parameters for the alloy $Hg_{0.3}Cd_{0.7}Te$ by linear interpolation of all Hamiltonian parameters except the band gap for which we use [24]

$$E_g(\text{eV}) = -0.303(1-x) + 1.606x - 0.132x(1-x). \tag{2.71}$$

The valence band offsets for InAs/GaSb/AlSb system are 0.56 eV for GaSb-InAs, 0.18 eV for AlSb-InAs, and −0.38 eV for AlSb-GaSb [25], whereas for HgTe/CdTe for HgTe-CdTe it is 0.570 eV [23, 24].

Table 2.5: Band structure parameters for InAs, GaSb, and AlSb [25, 26]. These parameters are the bare parameters and need to be renormalized before using them in simulation. All parameters are for $T = 0$ K.

	E_g [eV]	Δ [eV]	E_P [eV]	m_c/m_0	g_c	γ_1	γ_2	γ_3	κ
InAs	0.41	0.38	22.2	0.024	-14.8	19.67	8.37	9.29	7.68
GaSb	0.8128	0.752	22.4	0.042	-7.12	11.80	4.03	5.26	3.18
AlSb	2.32	0.75	18.7	0.18	0.52	4.15	1.01	1.75	0.31

Table 2.6: Band structure parameters for HgTe and CdTe [23, 24]. These parameters are already in renormalized form and can be used directly in the simulation. Alloy parameters parameters for $Hg_{0.3}Cd_{0.7}Te$ are obtained using interpolation scheme from [24]. All parameters are for $T = 0$ K.

	E_g [eV]	Δ [eV]	E_P [eV]	m'_c/m_0	g'_c	γ'_1	γ'_2	γ'_3	κ'
HgTe	-0.303	1.08	18.8	1	2	4.1	0.5	1.3	-0.4
CdTe	1.606	0.91	18.8	1.22	2	1.47	-0.28	0.03	-1.31
HgCdTe	1.006	0.961	18.8	1.445	2	2.259	-0.046	0.411	-1.037

2.3.7. SPURIOUS SOLUTIONS

The Hamiltonian (2.57) exhibits unphysical solutions inside the band gap if $m'_c < 0$. These spurious solutions appear at large momenta, beyond the validity of the $\boldsymbol{k}\cdot\boldsymbol{p}$ model. We apply the method put forward in Ref. [22] to avoid these unphysical states: we renormalize P in a way that m_0/m'_c is equal to either 0 or 1 (our choice). From (2.59) we thus obtain

$$P^2 = \left(\frac{m_0}{m_c} - \frac{m_0}{m'_c}\right)\frac{E_0(E_0+\Delta_0)}{E_0+\frac{2}{3}\Delta_0}\,\frac{\hbar^2}{2m_0}, \tag{2.72}$$

which we then use to modify all other parameters, as required in Eq. (2.65). With this renormalization, the spurious solutions at large $\boldsymbol{k}$ are pushed away from the band gap, whilst preserving the band structure around $\boldsymbol{k} = 0$. In Chapter 3.1.3 we discuss the procedure of removing spurious solutions in tight-binding approach.

REFERENCES

[1] E. O. Kane, *Band structure of indium antimonide,* J Phys Chem Solids **1**, 249–261 (1957).

[2] E. O. Kane, *Semiconductors and Semimetals,* in *Physics of III-V-Compounds*, Vol. 1, edited by R. K. Willardson and A. C. Beer (Academic Press, New York, London, 1966) pp. 75–100.

[3] E. O. Kane, in *Handbook on Semiconductors*, Vol. 1, edited by W. Paul and F. John (North-Holland, Amsterdam, 1982) p. 193.

[4] G. Bastard, *Wave Mechanics Applied to Semiconductor Heterostructures* (Wiley, New York, 1988).

[5] S. Birner, *Modeling of semiconductor nanostructures and semiconductor–electrolyte interfaces*, Phd dissertation, Walter Schottky Institut, Technische Universität München (2011).

[6] T. Andlauer, *Optoelectronic and spin-related properties of semiconductor nanostructures in magnetic fields*, Phd dissertation, Walter Schottky Institut, Technische Universität München (2009).

[7] T. Andlauer, *Discretization of multiband-$k\cdot p$-Schrödinger equations for multidimensional semiconductor nanostructures*, Diploma thesis, Walter Schottky Institut, Technische Universität München (2004).

[8] G. Calin, *$k\cdot p$ Theory Of Semiconductor Nanostructures*, Phd dissertation, Worcester Polytechnic Institute (2005).

[9] L. C. L. Y. Voon, *Electronic and Optical Properties of Semiconductors: A Study Based on the Empirical Tight Binding Model*, Phd dissertation, Universal-Publishers (1997).

[10] P. Löwdin, *A Note on the Quantum-Mechanical Perturbation Theory,* J. Chem. Phys. **19**, 1396–1401 (1951).

[11] J. M. Luttinger and W. Kohn, *Motion of Electrons and Holes in Perturbed Periodic Fields,* Phys Rev **97**, 869–883 (1955).

[12] G. L. Bir and G. Pikus, *Symmetry and strain-induced effects in semiconductors* (New York, Wiley, 1974).

[13] R. Winkler, *Spin-Orbit Coupling Effects in Two-Dimensional Electron and Hole Systems* (Springer, Berlin, Heidelberg, 2003).

[14] P. Yu and M. Cardona, *Fundamentals of Semiconductors: Physics and Materials Properties*, 4th ed. (Springer, Berlin ; New York, 2010).

[15] J. Sakurai, *Modern Quantum Mechanics* (Addison-Wesley, 1994).

[16] O. Madelung, M. Schulz, and H. Weiss, eds., *Landolt-Börnstein*, Vol. 17a-h (Semiconductors) (Springer, Berlin, Heidelberg, 1987).

[17] G. Dresselhaus, A. F. Kip, and C. Kittel, *Cyclotron Resonance of Electrons and Holes in Silicon and Germanium Crystals,* Phys. Rev. **98**, 368 (1955).

[18] J. M. Luttinger, *Quantum Theory of Cyclotron Resonance in Semiconductors: General Theory,* Phys. Rev. **102**, 1030 (1956).

[19] J. M. Hinckley and J. Singh, *Hole transport theory in pseudomorphic* $\mathrm{Si}_{1-\mathrm{x}}\mathrm{Ge}_{\mathrm{x}}$ *alloys grown on Si(001) substrates,* Phys. Rev. B **41**, 2912 (1990).

[20] I. Vurgaftman, J. R. Meyer, and L. R. Ram-Mohan, *Band parameters for III–V compound semiconductors and their alloys,* J. Appl. Phys. **89**, 5815 (2001).

[21] M. G. Burt, *The justification for applying the effective-mass approximation to microstructures,* J. Phys. Condens. Matter **4**, 6651 (1992).

[22] B. A. Foreman, *Elimination of spurious solutions from eight-band* $k\cdot p$ *theory,* Phys. Rev. B **56**, R12748–R12751 (1997).

[23] E. G. Novik, A. Pfeuffer-Jeschke, T. Jungwirth, V. Latussek, C. R. Becker, G. Landwehr, H. Buhmann, and L. W. Molenkamp, *Band structure of semimagnetic* $\mathrm{Hg}_{1-y}\mathrm{Mn}_y\mathrm{Te}$ *quantum wells,* Phys. Rev. B **72**, 035321 (2005).

[24] A. J. Pfeuffer-Jeschke, *Transport experiments in two-dimensional systems with strong spin-orbit interaction,* Ph.D. thesis, Physikalisches Institut, Universität Würzburg (2000).

[25] E. Halvorsen, Y. Galperin, and K. A. Chao, *Optical transitions in broken gap heterostructures,* Phys. Rev. B **61**, 16743 (2000).

[26] P. Lawaetz, *Valence-Band Parameters in Cubic Semiconductors,* Phys Rev B **4**, 3460–3467 (1971).

3

NUMERICAL METHODS FOR SEMICONDUCTORS

There is a computer disease that anybody who works with computers knows about. It's a very serious disease and it interferes completely with the work. The trouble with computers is that you 'play' with them!

Richard Feynman

In the previous chapter we have discussed a theoretical background of **k·p** theory and Löwdin partitioning, two important theoretical methods for semiconductor research. In this chapter we take a look on two numerical projects that simplify working with these methods.

The first of them aims on automatizing the discretization process—derivation of a tight-binding approximation of a given continuous Hamiltonian—that allows one to do numerical calculations of a system's band structure or transport properties.

The second project is an implementation of a Löwdin's quasi-degenerate perturbation theory. Our approach allows one to obtain in principle effective models of any order. The perturbation Hamiltonian is represented using free parameters, e.g. in-plane momenta or magnetic field, and the obtained effective model is a polynomial in these free parameters.

3.1. TIGHT-BINDING APPROACH

Physical devices, such as two-dimensional heterostructures or quantum nanowires, are often characterized by the complicated geometry. Together with a nontrivial structure of the Hamiltonian (2.64) this make solving the Schrödinger equation

$$H\left|\psi\right\rangle = E\left|\psi\right\rangle \tag{3.1}$$

analytically very difficult, if not even impossible, in most cases. For this reason the numerical calculation, that uses the approximated method, is often the only possible solution.

3.1.1. GENERAL CONSIDERATIONS

I will present a method that, due to similarity of the mathematical formalism, is called tight-binding approach.[1] In this method we do not longer consider the Hamiltonian as defined in a continuum space but rather as defined on a discrete lattice. We assume that the lattice is build from N sites with positions $\boldsymbol{x}_i$ for $i \in \{1\ldots N\}$. The eigenstate of position operator at site $\boldsymbol{x}_i$ is $|i\rangle$ and value of the wave function is $\left\langle i\middle|\psi\right\rangle = \psi(i)$. In this notation, the Hamiltonian and the wave function take following forms

$$H = \sum_{i,j} t_{ij} \left|i\right\rangle\!\left\langle j\right| , \tag{3.2a}$$

$$\left|\psi\right\rangle = \sum_{j} \psi(j) \left|j\right\rangle . \tag{3.2b}$$

Substituting Eqs. (3.2) into Eq. (3.1) and multiplying by $\langle\boldsymbol{x}|$ from the left-hand side we obtain

$$H\psi(\boldsymbol{x}) = \left\langle \boldsymbol{x}\middle|H\middle|\psi\right\rangle = \sum_j t_{xj}\psi(j) = E\psi(\boldsymbol{x}) . \tag{3.3}$$

The discretization procedure is based on approximating the differential operator on

---

[1] In mathematics this approach is known as finite difference method.

the discrete lattice. First, we do a Taylor expansion of $f(x)$:

$$f(x+a) = f(x) + f'(x)a + \frac{1}{2}f''(x)a^2 + \mathcal{O}(a^3)\,, \tag{3.4a}$$

$$f(x-a) = f(x) - f'(x)a + \frac{1}{2}f''(x)a^2 + \mathcal{O}(a^3)\,. \tag{3.4b}$$

This leads us to a central derivatie scheme:

$$f'(x) = \frac{1}{2a}\left[f(x+a) - f(x-a)\right] + \mathcal{O}(a^2)\,, \tag{3.5a}$$

$$f''(x) = \frac{1}{a^2}\left[f(x+a) + f(x-a) - 2f(x)\right] + \mathcal{O}(a)\,. \tag{3.5b}$$

As an example let us consider a one-dimensional Hamiltonian of a single particle with mass m that moves in potential $V(x)$:

$$H\psi(x) = \left\{-\frac{\hbar^2}{2m}\partial_x^2 + V(x)\right\}\psi(x)\,, \tag{3.6a}$$

$$H\psi(x) = -\frac{\hbar^2}{2ma^2}\left\{\psi(x+a) + \psi(x-a) - 2\psi(x)\right\} + V(x)\psi(x)\,. \tag{3.6b}$$

From Eq. (3.3) we immediately read

$$t_{x,x-a} = -t\,, \quad t_{x,x+a} = -t\,, \quad t_{x,x} = 2t + V(x)\,, \tag{3.7}$$

where $t = \frac{\hbar^2}{2ma^2}$. For a finite system of N sites the Schrödinger equation can be written in a matrix form

$$\begin{pmatrix} 2t+V(x) & -t & & \\ -t & \ddots & \ddots & \\ & \ddots & \ddots & -t \\ & & -t & 2t+V(x) \end{pmatrix} \begin{pmatrix} \psi(0) \\ \psi(1) \\ \vdots \\ \psi(N-1) \end{pmatrix} = E \begin{pmatrix} \psi(0) \\ \psi(1) \\ \vdots \\ \psi(N-1) \end{pmatrix}, \tag{3.8}$$

and diagonalized numerically.

3.1.2. AUTOMATING THE PROCESS: THE DISCRETIZER

The discretization procedure is usually a simple process. However, its complexity increase rapidly when we include more degrees of freedom, such as spin and space dependent parameters. To save time and reduce possibility of human-caused errors we wrote, together with S.H.P Rubbert, an automated tool called the Discretizer. The reference implementation has been released with version 1.3 of a Python simulation package Kwant [1].

Our algorithm is based on Eq. (3.5a). We decide to use tight-binding approximation of a first-order derivative, instead of a general formula, in order to handle Hamiltonian with space dependent parameters, e.g.

$$H = -\frac{\hbar^2}{2}\partial_x \frac{1}{m(x)}\partial_x\,. \tag{3.9}$$

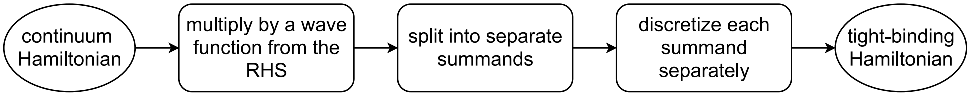

Figure 3.1: Overview of the `discretizer` algorithm. The initial continuum Hamiltonian is first multiplied by a trial wave function and split into separate summands. Each summand is then discretized independently and tight-binding approximation of the continuum Hamiltonian is returned.

When we apply Eq. (3.5a) to each derivative operator, one at a time,

$$H\psi(x) \approx -\partial_x \frac{1}{m(x)} \partial_x \psi(x)\,, \tag{3.10a}$$

$$H\psi(x) \approx -\frac{1}{2a} \partial_x \frac{1}{m(x)} \big(\psi(x+a) - \psi(x-a)\big)\,, \tag{3.10b}$$

$$H\psi(x) \approx -\frac{1}{4a^2} \left(\frac{\psi(x+2a)}{m(x+a)} + \frac{\psi(x-2a)}{m(x-a)} - \left(\frac{1}{m(x+a)} + \frac{1}{m(x-a)} \right) \psi(x) \right)\,, \tag{3.10c}$$

the result is a tight-binding Hamiltonian with an onsite term and next-nearest-neighbour hoppings. Because nearest-neighbour hoppings are absent, this Hamiltonian is equivalent to two disconnected sublattices which is clearly wrong. To workaround this problem one can substitute $a \to a/2$:

$$H\psi(x) \approx -\frac{1}{a^2} \left(\frac{\psi(x+a)}{m(x+\frac{a}{2})} + \frac{\psi(x-a)}{m(x-\frac{a}{2})} - \left(\frac{1}{m(x+\frac{a}{2})} + \frac{1}{m(x-\frac{a}{2})} \right) \psi(x) \right)\,. \tag{3.11}$$

For the general situation the solution is to find a greatest-common-divisor (GCD) of all hopping lengths coming from one summand of initial Hamiltonian and substitute $a \to a/GCD$. For the multi-dimensional systems this procedure must be done along each axis separately. For the purpose of our algorithm, we call this procedure a hopping shortening.

Figure 3.1 contains a flowchart of the algorithm. Initial Hamiltonian may contain terms with differential operators of different order, e.g. $H = ak_x^2 + bk_x^4$, where $k_x = -i\partial_x$. Therefore, it is necessary to conduct a discretization procedure on each of the summands separately. We present details of the discretization procedure on Fig. 3.2. We start with the

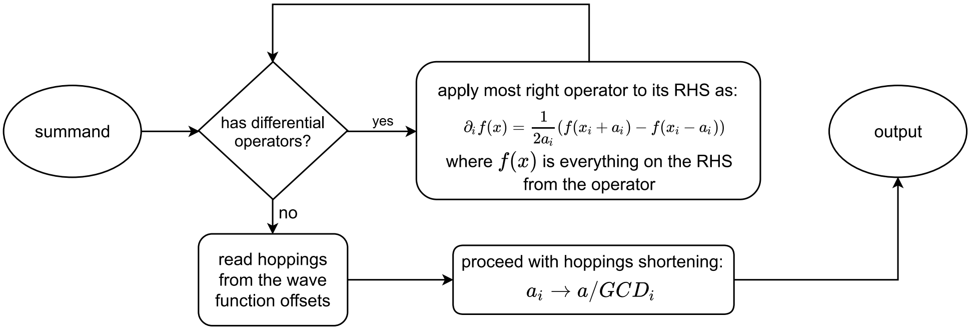

Figure 3.2: Details of discretization procedure.

most right differential operator and use Eq. (3.5a) to apply it to its right hand side (RHS). We repeat the procedure for all differential operators present in the summand. Finally we calculate the GCD of hoppings' lengths and conduct the shortening procedure.

Simple example: Rashba Hamiltonian As an example we now consider a simple Hamiltonian of a spin-full electron with a spin-orbit coupling α:

$$H = k_x^2 + \alpha k_x \sigma_y . \tag{3.12}$$

Making use of the reference implementation in Kwant, we obtain a following tight-binding Hamiltonian

$$t_{x,x} = \begin{pmatrix} \frac{2}{a^2} & 0 \\ 0 & \frac{2}{a^2} \end{pmatrix}, \tag{3.13}$$

$$t_{x,x+a} = \begin{pmatrix} -\frac{1}{a^2} & -\frac{\alpha}{2a} \\ \frac{\alpha}{2a} & -\frac{1}{a^2} \end{pmatrix}. \tag{3.14}$$

We can then make further use of Kwant to calculate, in example, the band structure of this model, Fig. 3.3.

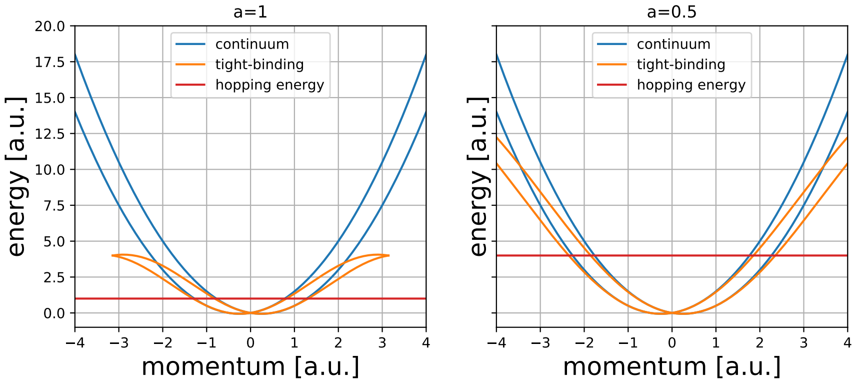

Figure 3.3: Tight-binding simulation of a spin-full electron with spin-orbit orbit coupling α: $H = k_x^2 + \alpha k_x \sigma_y$.

We can clearly see strong dependence on the chosen grid spacing a. First, the range of momenta is limited by the Brillouin zone that extends from $-\pi/a$ to π/a. Second, we see that the smaller grid spacing a is, the better the continuous dispersion is approximated by the tight-binding model. The rule-of-thumb is that the tight-binding dispersion gives good approximation for states which have energy smaller than the magnitude of the hopping. For this example it means that

$$E < |t| = \frac{1}{a^2} .$$

3.1.3. SIMULATION EXAMPLE: InAs/GaSb QUANTUM WELL

We now take a look on a tight-binding simulation for the $\mathbf{k}\cdot\mathbf{p}$-Hamiltonian. As an example we will consider a two-dimensional InAs/GaSb quantum well, tuned into non-inverted regime: $L_{\text{InAs}} = L_{\text{GaSb}} = 5\,\text{nm}$. We choose discretization grid spacing to be $a = 0.5$ nm, which value approximates continuum band structure properly for a relevant range of energies.

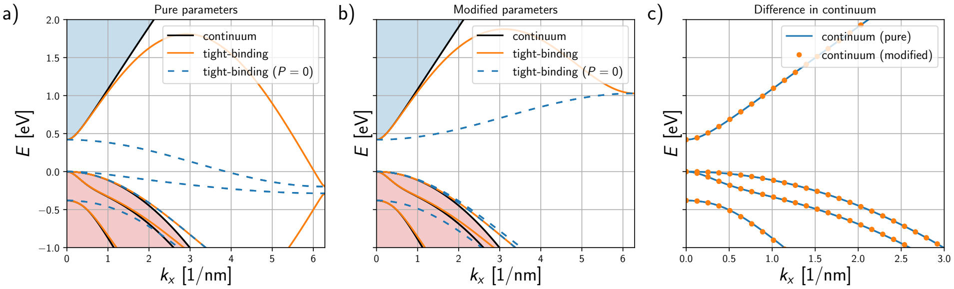

Figure 3.4: Dispersion of bulk InAs. (a-b) Removing of spurious solution. (black) Continuum dispersion. (orange) Tight-binding dispersion. (dashed blue) Tight-binding dispersion without the conduction-valence band interaction ($P = 0$). (a) Tight-binding dispersion shows spurious solution when effective mass is negative, $\gamma_0' < 0$, because the $\mathbf{k}\cdot\mathbf{p}$ interaction vanish at the edge of the Brillouin zone. (b) Spurious solution are removed by modification of the interband momentum P in a way that $\gamma_0' = 1$. (c) Difference in continuum dispersion caused by modification of interband momentum P is negligible.

Elimination of spurious solutions In the beginning of every $\mathbf{k}\cdot\mathbf{p}$-simulation, we must make sure that our model does not exhibit spurious solutions in its bulk dispersion. As it was mentioned in Chapter 2.3.5, the $\mathbf{k}\cdot\mathbf{p}$-Hamiltonian in tight-binding approach exhibits unphysical solution in the band gap if $\gamma_0' < 0$. In the continuum model, the $\mathbf{k}\cdot\mathbf{p}$ interaction between conduction and valence band repulses the conduction band and despite negative γ_0' dispersion of the conduction band is correct. In the tight-binding approach, k-linear terms behave as

$$k \to \frac{2}{a} \sin ka, \tag{3.15}$$

and therefore the $\mathbf{k}\cdot\mathbf{p}$ interaction vanishes at the edge of the Brillouin zone, leading to the unphysical solutions in the band gap, see Fig. 3.4 (a). In order to eliminate this unphysical solutions, we apply the method that we described in Chapter 2.3.5. By setting $\gamma_0' = 1$ we push spurious solution out of the band gap, see Fig. 3.4 (b). Furthermore the change in P yields no significant change in bulk dispersion, see Fig. 3.4 (c), and is typically smaller than 10%. Though in Figure 3.4 we show only elimination of spurious solution for InAs, the same procedure must be repeated for all materials present in the system.

Tight-binding simulation of InAs/GaSb **quantum well** Now that we modified interband momentum P in a way that eliminates the spurious solutions, we perform a $\mathbf{k}\cdot\mathbf{p}$-simulation of the system. Derivation of a proper tight-binding model from the continuum

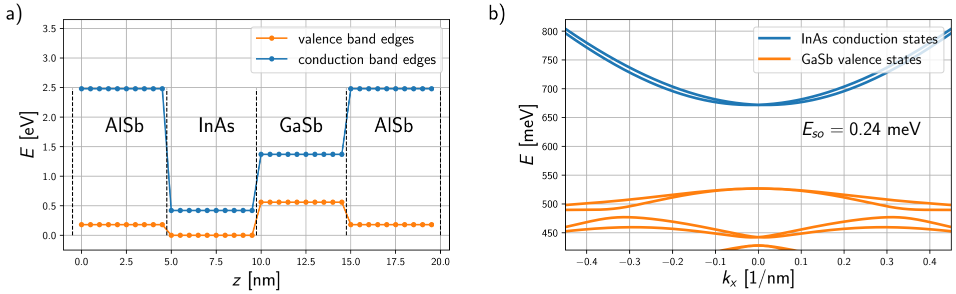

Figure 3.5: InAs/GaSb quantum well system. (a) Schematic structure of the InAs/GaSb heterostructure, that shows variation of the conduction (blue) and valence (orange) band along the growth direction z. (b) Numerically calculated **k**·**p**-dispersion of quantum well. $L_{\text{InAs}} = L_{\text{GaSb}} = 5$ nm.

k·**p**-Hamiltonian is greatly simplified by the `kwant.continuum` module,[2] which contains a reference implementation of the discretization alogirthm discussed in Chapter 3.1.2. Once the 8×8 Kane Hamiltonian, Eq. (2.64), is defined in SymPy,[3] the tight-binding model is obtained using the Discretizer. We then use Kwant to build a finite system. We choose z to be the growth direction, thus all material parameters are z-dependent. Figure 3.5 (a) show the evolution of conduction and valence band edges in function of z along the system.

Band structure calculation Once the system is built we obtain the Bloch Hamiltonian $H(k_x, k_y)$ that we use to compute the dispersion, see Fig. 3.5 (b). The InAs/GaSb quantum well is tuned into the trivial regime. Due to the strong structure inversion asymmetry, the band structure exhibits relatively strong Rashba spin-orbit effect without a presence of an external electric field. In Chapters 4 and 6 we investigate properties of this system in topological regime.

3.2. EFFECTIVE MODELS

In Section 2.1.2 we discussed the quasi-degenerate perturbation theory, called Löwdin partitioning. In this section we discuss a possible numerical implementation, that allows one to calculate effective models of an arbitrary order. We base our implementation on

---

[2] We would like to draw attention to the ongoing effort that is made to provide an open-source Python package that aim to help in performing **k**·**p**-simulations. Goal of the package is to provide research-ready implementation of the common **k**·**p**-models and all necessary tools for making **k**·**p**-simulations with Kwant. Early stage of the code can be find at the following link: `https://gitlab.kwant-project.org/semicon/semicon`.

[3] The syntax that is used to defined Hamiltonian in SymPy resembles that of LaTeX. Furthermore, the Hamiltonian defined in this way can be easily rendered using LaTeX in order to simplify proof reading of the implementation.

equations (2.17a) and (2.17b), which we repeat here:

$$\tilde{H}_d = \sum_{n=0}^{\infty} \frac{1}{(2n)!}[H^0 + H^1, S]^{(2n)} + \sum_{n=0}^{\infty} \frac{1}{(2n+1)!}[H^2, S]^{(2n+1)}, \tag{2.17a}$$

$$\tilde{H}_n = \sum_{n=0}^{\infty} \frac{1}{(2n+1)!}[H^0 + H^1, S]^{(2n+1)} + \sum_{n=0}^{\infty} \frac{1}{(2n)!}[H^2, S]^{(2n)}. \tag{2.17b}$$

We assume that the goal is to obtain effective model of the N-th order.

3.2.1. CALCULATION OF $S^{(j)}$

Similarly as in in Section 2.1.2, we start with computing the operator S. We perform this task using SymPy [2], a Python module for symbolic calculations. We use the fact that for the N-th order we only need to know $S^{(k)}$ up to the $k_N = N-1$ order. Equation (2.18) reads now

$$S = \sum_{k=1}^{k_N} S^{(k)} \tag{3.16}$$

We then substitute Eq. (3.16) into Eq. (2.17b) and evaluate all commutator relations. We group all terms of the same order. Each group of the i-th order terms always contains $\left[H^0, S^{(i)}\right]$, e.g.

$$\begin{aligned}
&\text{1-st order:} && [H^0, S^{(1)}] + H^2 = 0, && (3.17a)\\
&\text{2-st order:} && [H^0, S^{(2)}] + [H^1, S^{(1)}] = 0, && (3.17b)\\
&\text{3-st order:} && [H^0, S^{(3)}] + \ldots = 0, && (3.17c)\\
&\ldots && \ldots .
\end{aligned}$$

We then obtain automatically generated expressions for $Y_i = \left[H^0, S^{(i)}\right]$, that we present below up to the 5-th order:[4]

---

[4] Please note that in Eqs. (3.18), and only there, order of a term is denotes by a lower index. We have generated Y_i functions up to the 8-th order.

$$Y_1 = -H_2\,, \tag{3.18a}$$

$$Y_2 = -H_1 S_1 + S_1 H_1\,, \tag{3.18b}$$

$$\begin{aligned} Y_3 = {} & -H_1 S_2 + S_1 H_2 S_1 + S_2 H_1 - \frac{1}{2} H_2 S_1^2 + \frac{1}{2} S_1 H_0 S_1^2 - \frac{1}{2} S_1^2 H_0 S_1 - \frac{1}{2} S_1^2 H_2 - \frac{1}{6} H_0 S_1^3 \\ & + \frac{1}{6} S_1^3 H_0\,, \end{aligned} \tag{3.18c}$$

$$\begin{aligned} Y_4 = {} & -H_1 S_3 + S_1 H_2 S_2 + S_2 H_2 S_1 + S_3 H_1 - \frac{1}{2} H_2 S_1 S_2 - \frac{1}{2} H_2 S_2 S_1 + \frac{1}{2} S_1 H_0 S_1 S_2 \\ & + \frac{1}{2} S_1 H_0 S_2 S_1 + \frac{1}{2} S_1 H_1 S_1^2 - \frac{1}{2} S_1 S_2 H_0 S_1 - \frac{1}{2} S_1 S_2 H_2 - \frac{1}{2} S_1^2 H_0 S_2 - \frac{1}{2} S_1^2 H_1 S_1 \\ & + \frac{1}{2} S_2 H_0 S_1^2 - \frac{1}{2} S_2 S_1 H_0 S_1 - \frac{1}{2} S_2 S_1 H_2 - \frac{1}{6} H_0 S_1 S_2 S_1 - \frac{1}{6} H_0 S_1^2 S_2 - \frac{1}{6} H_0 S_2 S_1^2 \\ & - \frac{1}{6} H_1 S_1^3 + \frac{1}{6} S_1 S_2 S_1 H_0 + \frac{1}{6} S_1^2 S_2 H_0 + \frac{1}{6} S_1^3 H_1 + \frac{1}{6} S_2 S_1^2 H_0\,, \end{aligned} \tag{3.18d}$$

$$\begin{aligned} Y_5 = {} & -H_1 S_4 + S_1 H_2 S_3 + S_2 H_2 S_2 + S_3 H_2 S_1 + S_4 H_1 - \frac{1}{2} H_2 S_1 S_3 - \frac{1}{2} H_2 S_2^2 \\ & - \frac{1}{2} H_2 S_3 S_1 + \frac{1}{2} S_1 H_0 S_1 S_3 + \frac{1}{2} S_1 H_0 S_2^2 + \frac{1}{2} S_1 H_0 S_3 S_1 + \frac{1}{2} S_1 H_1 S_1 S_2 \\ & + \frac{1}{2} S_1 H_1 S_2 S_1 - \frac{1}{2} S_1 S_2 H_0 S_2 - \frac{1}{2} S_1 S_2 H_1 S_1 - \frac{1}{2} S_1 S_3 H_0 S_1 - \frac{1}{2} S_1 S_3 H_2 \\ & - \frac{1}{2} S_1^2 H_0 S_3 - \frac{1}{2} S_1^2 H_1 S_2 + \frac{1}{2} S_2 H_0 S_1 S_2 + \frac{1}{2} S_2 H_0 S_2 S_1 + \frac{1}{2} S_2 H_1 S_1^2 - \frac{1}{2} S_2 S_1 H_0 S_2 \\ & - \frac{1}{2} S_2 S_1 H_1 S_1 - \frac{1}{2} S_2^2 H_0 S_1 - \frac{1}{2} S_2^2 H_2 + \frac{1}{2} S_3 H_0 S_1^2 - \frac{1}{2} S_3 S_1 H_0 S_1 - \frac{1}{2} S_3 S_1 H_2 \\ & - \frac{1}{4} S_1^2 H_2 S_1^2 - \frac{1}{6} H_0 S_1 S_2^2 - \frac{1}{6} H_0 S_1 S_3 S_1 - \frac{1}{6} H_0 S_1^2 S_3 - \frac{1}{6} H_0 S_2 S_1 S_2 - \frac{1}{6} H_0 S_2^2 S_1 \\ & - \frac{1}{6} H_0 S_3 S_1^2 - \frac{1}{6} H_1 S_1 S_2 S_1 - \frac{1}{6} H_1 S_1^2 S_2 - \frac{1}{6} H_1 S_2 S_1^2 + \frac{1}{6} S_1 H_2 S_1^3 + \frac{1}{6} S_1 S_2 S_1 H_1 \\ & + \frac{1}{6} S_1 S_2^2 H_0 + \frac{1}{6} S_1 S_3 S_1 H_0 + \frac{1}{6} S_1^2 S_2 H_1 + \frac{1}{6} S_1^2 S_3 H_0 + \frac{1}{6} S_1^3 H_2 S_1 + \frac{1}{6} S_2 S_1 S_2 H_0 \\ & + \frac{1}{6} S_2 S_1^2 H_1 + \frac{1}{6} S_2^2 S_1 H_0 + \frac{1}{6} S_3 S_1^2 H_0 - \frac{1}{12} S_1^2 H_0 S_1^3 + \frac{1}{12} S_1^3 H_0 S_1^2 - \frac{1}{24} H_2 S_1^4 \\ & + \frac{1}{24} S_1 H_0 S_1^4 - \frac{1}{24} S_1^4 H_0 S_1 - \frac{1}{24} S_1^4 H_2 - \frac{1}{120} H_0 S_1^5 + \frac{1}{120} S_1^5 H_0\,. \end{aligned} \tag{3.18e}$$

To calculate Y_j we need to know the matrix form of H^0, H^1, H^2 in basis that diagonalizes H^0, Eq. (2.11), and all $S^{(k)}$ for $k < j$. We then make use of the fact that

$$\langle \varphi_m | [H^0, S^{(i)}] | \varphi_l \rangle = (E_m - E_l) S^{(i)}_{ml}\,, \tag{3.19}$$

to calculate $S^{(j)}$ as

$$S^{(j)}_{ml} = \frac{1}{E_m - E_l} (Y_j)_{ml}\,. \tag{3.20}$$

3.2.2. CALCULATION OF $\tilde{H}$

So far we considered H^0, H^1, H^2 to be SymPy symbols, and discussed how one can obtain $S^{(j)}$ knowing the matrix form of these quantities. The main goal however is to obtain effective models that contain one or more free parameters, e.g. momentum or magnetic field. Let assume that we have following Hamiltonian for a two-dimensional quantum well

$$H = H(k_x, k_y, k_z)\,, \tag{3.21}$$

where k_x and k_y are the in-plane momenta, z is the growth direction and $k_z = -\mathrm{i}\partial_z$. In addition we will assume that our Hamiltonian has N_b orbitals, e.g. $N_b = 8$ for the $\mathbf{k}{\cdot}\mathbf{p}$ Hamiltonian. When discretized along the z-direction on the grid with N points we have $8N$ bands. Obtaining an effective model for this system allows us to have model with only a couple of bands that we choose in context of specified physical scenario.

We therefore divide our Hamiltonian into two parts as

$$H = H^0 + H'\,, \tag{3.22a}$$

$$H^0 = H(k_x = k_y = 0, k_z = -\mathrm{i}\partial_z)\,, \tag{3.22b}$$

$$H' = H - H^0\,. \tag{3.22c}$$

We discretize H^0 and diagonalize it to obtain eigenstates $\{|\varphi_n\rangle\}$ with energies E_n. We then express perturbation H' as a polynomial

$$H' = \sum_{\alpha,\beta} H_{\alpha\beta}(k_z = -\mathrm{i}\partial_z) k_x^\alpha k_y^\beta\,, \tag{3.23}$$

where we treat k_x, k_y as the free parameters. We discretize $H_{\alpha\beta}$ on the same grid as H^0 and transform them to $\{|\varphi_n\rangle\}$ basis. We obtain H^0, H^1, and H^2, which we use then to calculate $S^{(i)}$. Finally we calculate the effective Hamiltonian using Eq. (2.17a) and truncate all terms that have higher powers of k_x and k_y than desired order of perturbation.

3.2.3. SIMULATION EXAMPLE: EFFECTIVE MODEL FOR InAs/GaSb QUANTUM WELL

We now come back to the example of InAs/GaSb, that we discussed in Chapter 3.1.3. Following the implementation described in previous chapter, we obtain an effective model for first electron band:

$$\tilde{H} = \begin{bmatrix} 0.710k_x^2 + 0.710k_y^2 + 0.672 & -0.0261 i k_x + 0.0261 k_y \\ 0.0261 i k_x + 0.0261 k_y & 0.710k_x^2 + 0.710k_y^2 + 0.6721 \end{bmatrix}. \tag{3.24}$$

In Figure 3.6 we compare the exact $\mathbf{k}{\cdot}\mathbf{p}$-dispersion obtained in Chapter 3.1.3 with the dispersion obtained from the effective model. Around $k_x = 0.2\,/\mathrm{nm}$, these two dispersions start to diverge due to increasing strength of the perturbation. From the effective model we read Rashba coefficient to be $|\alpha| = 26\,\mathrm{meV}\cdot\mathrm{nm}$.

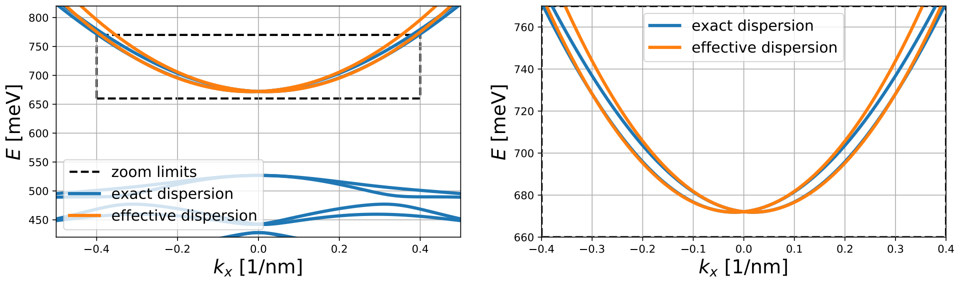

Figure 3.6: Dispersion of InAs/GaSb quantum well obtained from the effective model. The effective dispersion is compared to the exact one obtained from the $\mathbf{k}\cdot\mathbf{p}$-simulation. $L_{\mathrm{InAs}} = L_{\mathrm{GaSb}} = 5$ nm.

REFERENCES

[1] C. W. Groth, M. Wimmer, A. R. Akhmerov, and X. Waintal, *Kwant: a software package for quantum transport,* New J. Phys. **16**, 063065 (2014).

[2] A. Meurer, C. P. Smith, M. Paprocki, O. Čertík, S. B. Kirpichev, M. Rocklin, A. Kumar, S. Ivanov, J. K. Moore, S. Singh, T. Rathnayake, S. Vig, B. E. Granger, R. P. Muller, F. Bonazzi, H. Gupta, S. Vats, F. Johansson, F. Pedregosa, M. J. Curry, A. R. Terrel, v. Roučka, A. Saboo, I. Fernando, S. Kulal, R. Cimrman, and A. Scopatz, *SymPy: Symbolic computing in Python,* PeerJ Comput. Sci. **3**, e103 (2017).

4

ROBUST HELICAL EDGE TRANSPORT IN QUANTUM SPIN HALL QUANTUM WELLS

This chapter has been previously published as **Rafal Skolasinski**, Dmitry I. Pikulin, Jason Alicea, and Michael Wimmer, *Robust Helical Edge Transport in Quantum Spin Hall Quantum Wells*, arXiv:1709.04830 (2017). The submission to Phys. Rev. Lett. is pending.

4.1. INTRODUCTION

Topological insulators (TIs) are materials that exhibit a gapped bulk yet enjoy metallic surface or edge states protected by time-reversal symmetry. In particular, two-dimensional (2D) TIs host helical edge modes—i.e., counter-propagating states composed of Kramers partners—that underlie quantized edge conductance [1–3]. Consequently, 2D TIs are often referred to as quantum spin Hall (QSH) systems. The experimentally most studied QSH systems are now based on semiconductor quantum wells. Following the proposal of Bernevig, Hughes, and Zhang [4], the QSH effect was first observed in HgTe/(Hg,Cd)Te quantum wells [5]; various QSH signatures, including quantized edge transport, have by now been identified in this material [6–9].

In HgTe, the QSH effect originates from an inversion of electron and hole bands that is intrinsic to HgTe. This inversion can also be engineered in a multilayer quantum well. In particular, InAs/GaSb quantum wells were also predicted to be QSH systems [10], as they exhibit a so-called broken gap alignment where the conduction band edge of electrons is energetically below the valence band edge of holes. Quantized edge conductance has also been observed in InAs/GaSb [11–13], and the properties of the band inversion and edge-state transport have since been investigated by several experimental groups [14–20].

The hallmark quantized edge conductance in QSH systems originates from time-reversal symmetry, which prevents the helical edge states from elastically backscattering in the presence of non-magnetic disorder. A magnetic field B breaks time-reversal symmetry, and common expectation dictates that quantized conductance must break down in this case. For example, a magnetic field applied to semiconductor-based QSH systems can directly couple the counter-propagating edge modes, opening up a Zeeman gap in the edge spectrum. It thus came as a surprise that Ref. [13] measured edge conductances that remained quantized with in-plane magnetic fields up to 12 T—sharply defying theoretical expectations.

Here we show that, contrary to naive expectations, edge-state transport in semiconductor-based QSH systems (HgTe and InAs/GaSb) *typically exhibits a very weak dependence on in-plane magnetic fields*. We have identified three mechanisms for such robustness: (i) The effective edge-state g-factor is strongly suppressed compared to the bulk electron g-factor due to significant heavy-hole contribution in the edge-state wavefunction. (ii) The Dirac point of the edge states typically resides not in the bulk energy gap, but is hidden in a bulk band. A Zeeman gap opened by the magnetic field appears only at the Dirac point and is thus invisible to transport (see Fig. 4.1). (iii) Although the combination of disorder and a magnetic field generically permits backscattering, it is strongly suppressed away from the Dirac point due to the nearly anti-aligned spins of the counter-propagating edge states [see Figs. 4.1(b) and (d)]. This alignment increases for energies away from the Dirac point. When the Dirac point is buried, one then obtains near-perfect quantization of edge conductance in a disordered system out to large magnetic fields of order 10 T as observed experimentally.

We note that buried Dirac points have been predicted and observed in several three-dimensional TIs [21–23]. Our findings suggest that Dirac-point burying is a common feature also in 2D QSH quantum-well platforms.

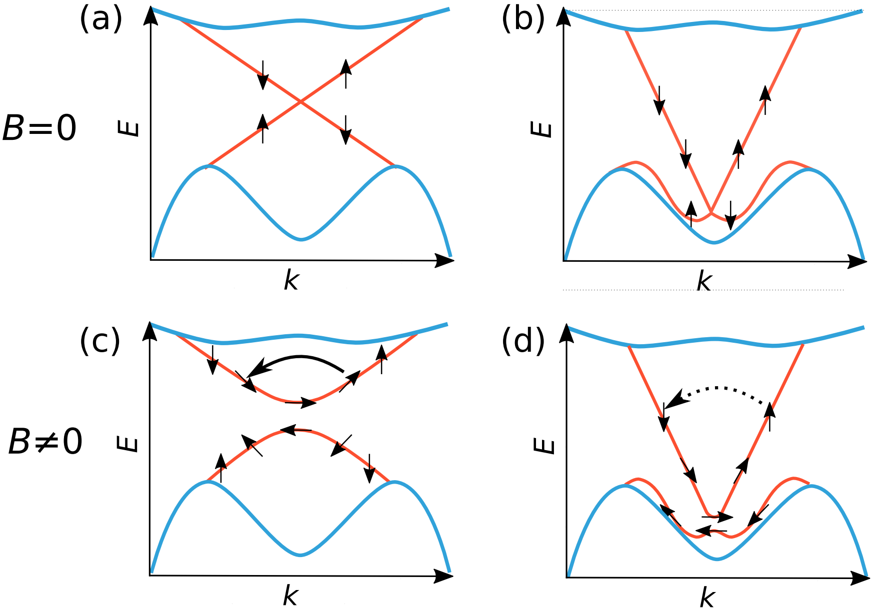

Figure 4.1: Schematic depiction of edge-state dispersions: in the absence of a magnetic field, the edge-state crossing is topologically protected, but may (a) reside in the gap or (b) be hidden in a bulk band. In a finite magnetic field, a Zeeman gap opens and the edge-state spins become canted—permitting backscattering as in (c) However, when the edge-state crossing is hidden in a bulk band, spins within the gap are further away from the Zeeman gap and nearly anti-align, greatly suppressing backscattering as in (d).

4.2. SUPPRESSION OF g-FACTOR

We first flesh out the suppression of the edge-state g-factor, which is already accessible from the canonical Bernevig-Hughes-Zhang (BHZ) model [4] written as:

$$[M - B_+(k_x^2 - \partial_y^2)]\psi_1 + A(k_x - \partial_y)\psi_2 = E\psi_1; \tag{4.1}$$

$$A(k_x + \partial_y)\psi_1 - [M - B_-(k_x^2 - \partial_y^2)]\psi_2 = E\psi_2. \tag{4.2}$$

Here A, M, and $B_\pm = B \pm D$ are BHZ model parameters, x is the propagation direction, y is the direction into the QSH bulk, and $\psi_{1,2}$ respectively denote the electron and hole part of the wavefunction within one spin sector. The derivation of the effective g-factor is based on computing the wavefunctions $\psi_{1,2}$ with a hard-wall boundary condition, similar to Ref. [24], and is presented in the Appendix. The result is simple and is based on the relative contributions of electrons and holes in the edge wavefunctions:

$$g_{\text{eff}} = \frac{g_e B_- + g_h B_+}{B_+ + B_-}. \tag{4.3}$$

Here g_e and g_h are electron and hole g-factors, respectively. Equation (4.3) shows that the effective g-factor of the edge states is the weighted sum of the electron and hole g-factors with their corresponding inverse masses as pre-factors.

Typically, g_h is much smaller than g_e; in fact $g_h = 0$ by symmetry in [001] quantum wells [25]. Moreover, the hole mass usually far exceeds that of electrons, i.e., $B_- \ll B_+$. Together these properties suppress the effective edge-state g-factor considerably compared to bulk values.

We have performed **k·p** simulations (see Appendix for details) to obtain numerical values for the g-factor in experimentally relevant geometries. For InAs/GaSb we find an edge-state g-factor $g_{\text{eff}} \sim 2$, whereas for HgTe we find $g_{\text{eff}} \sim 8 - 10$ (in our conventions the Zeeman gap is $g_{\text{eff}}\mu_B B$, with μ_B the Bohr magneton). In contrast, the bulk electron g-factors are $g \sim 6 - 8$ in InAs/GaSb and $g \sim 30 - 60$ in HgTe.

4.3. DIRAC-POINT BURYING FROM k·p MODELS

In the 'pure' BHZ model given above, the edge-state Dirac point always resides in the gap [24]. Recovering the burying of the Dirac point requires going beyond this minimal model. To this end we now simulate the full semiconductor heterostructure for the experimentally relevant InAs/GaSb and HgTe/CdTe quantum wells. In the numerical analysis we use the 8×8 Kane Hamiltonian [26–28]. Details of the model and material parameters appear in the Appendix. Using a finite-difference method with grid spacing a, we convert the continuous Kane Hamiltonian into a tight-binding model. The resulting energy dispersion are then computed using Kwant [29].

We investigate [001]-grown quantum wells sketched in Figs. 4.2(a) and (b). In particular, we consider InAs/GaSb with AlSb barrier (layer thicknesses 12.5 nm/5 nm as in Ref. [15]), and HgTe with HgCdTe barriers (thickness 7.5 nm as in Refs. [6, 9]). Figure 4.2 shows the dispersion for these heterostructures along the [100] direction. We compare the dispersion for an infinite 2D quantum well without edges (blue lines) to systems of finite width W (black lines) modeled using hard-wall boundary conditions.

Figures 4.2(c) and (d) respectively illustrate the energy dispersions for InAs/GaSb and HgTe in the absence of a magnetic field. In both quantum wells we observe that the edge-state crossing is shifted out of the topological gap and buried in the valence band. Note that while the crossing itself is topologically protected, its position inside the gap is not.

The **k·p** results diverge from the BHZ model due to the presence of additional hole states that are close in energy to the electron and heavy-hole (HH) bands forming the inverted band structure. For InAs/GaSb, those states lead to a significant deviation of the band structure at the topological gap from the BHZ model, which only contains momentum up to second order. Those states are energetically much further away from the gap than the size of the gap itself [no additional hole states are visible in Fig. 4.2(c)]; nevertheless, they strongly influence the gap edges at finite momentum, as the coupling between bands increases with momentum (see Appendix for models that take into account this interaction). In the case of HgTe a second HH band crosses with the topological gap. Since it only weakly interacts with the edge state, the Dirac point is deeply hidden in this additional band.

Figures 4.2(e) and (f) show the energy dispersions in a finite magnetic field. For both quantum wells, the Zeeman splitting of the edge states remains well-hidden in the valence band. Note that while the InAs/GaSb bulk band structure and bulk transport therein is affected by an in-plane field due to orbital effects on the tunneling between the two

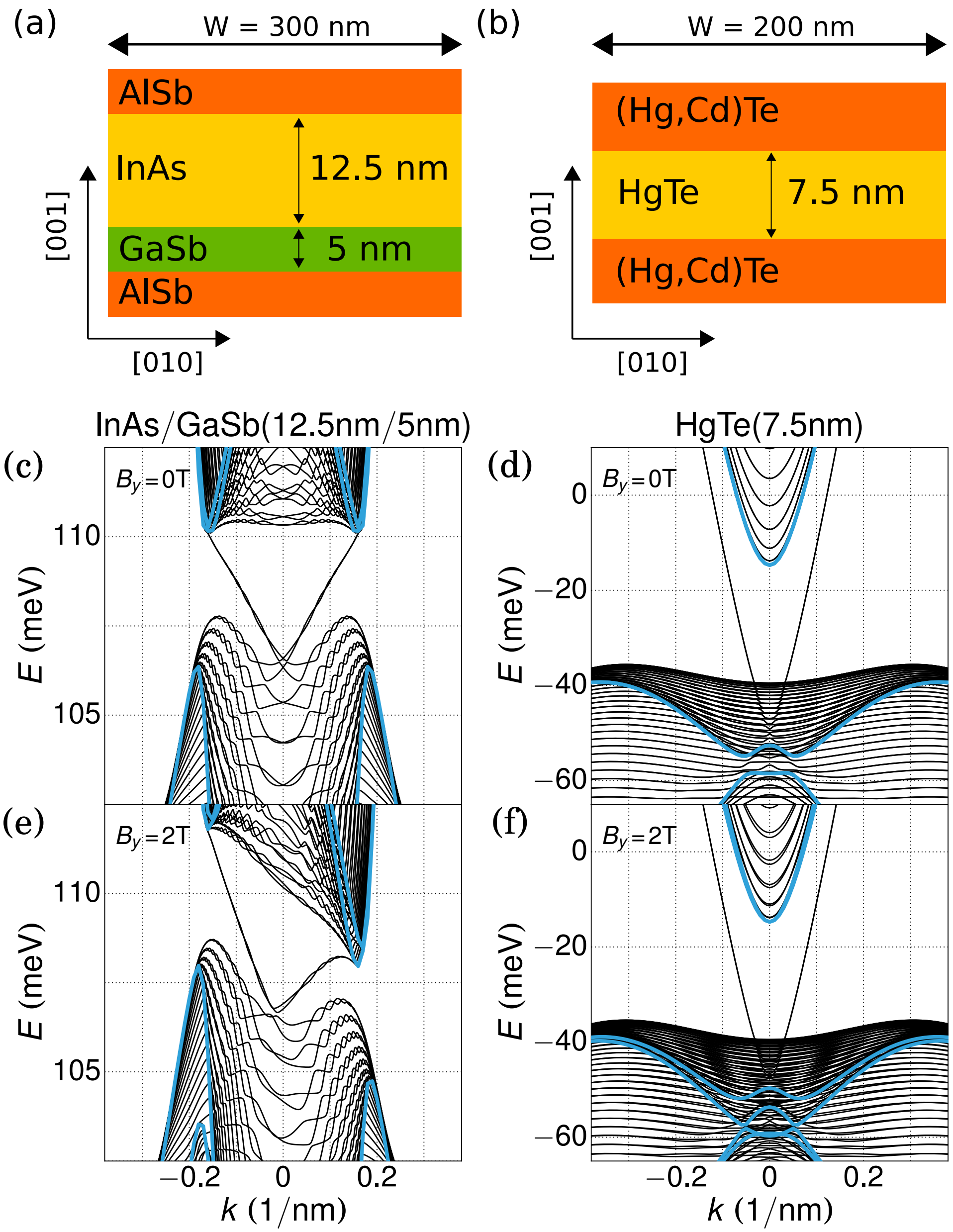

Figure 4.2: (a,b) system geometries used for **k·p** simulations. (c-f) Band structures for InAs/GaSb (c,e) and HgTe/CdTe (d,f). For both materials we observe Dirac points buried in a valence band, which obscures the opening of a Zeeman gap under applied in-plane magnetic fields as in (e) and (f).

layers [15, 30], this modification neither removes the edge states [31] nor the position of the edge-state crossing.[1]

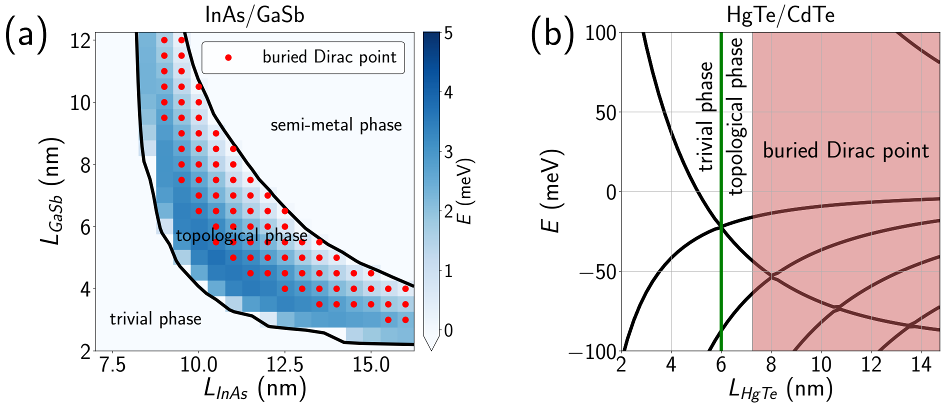

Figure 4.3: (a) Topological gap of InAs/GaSb as a function of InAs and GaSb well thicknesses. A red dot indicates a buried Dirac point. (b) Subband edges at the Γ-point of HgTe as a function of HgTe well thickness. The Dirac point is buried for thickness $L_{HgTe} \geq 7.25\,\mathrm{nm}$.

Figure 4.3 summarizes our simulations for different quantum-well thicknesses: Fig. 4.3(a) shows the topological phase diagram of InAs/GaSb as a function of layer thicknesses (a non-monotonic behaviour of the topological gap was also previously found in Ref. [32]), while Fig. 4.3(b) shows the HgTe band edges as a function of layer thickness (here we only have one parameter). In both cases we indicate when the edge-state Dirac point is buried—which occurs for most of the topological phase space as expected from our general arguments. The edge-state crossing remains in the gap only close to the topological phase transition; here only two bands interact in a small range of momentum and can be well-described by the BHZ model.

4.4. MODELLING DIRAC-POINT BURYING VIA EDGE POTENTIALS

So far we have considered the edge of the 2D QSH systems simply as a hard wall. However, several semiconducting surfaces additionally exhibit a band bending at the interface. A prominent example is InAs where the band bending can be of the order of 100 meV [33, 34]. In fact, band bending has been shown to have significant effects also in InAs/GaSb quantum wells [35, 36]. Apart from band bending due to details of the semiconductor surface, gating can also lead to a non-uniform electrostatic potential near the surface, e.g., due to the change of dielectric constant at the semiconductor/vacuum interface.

A position-dependent potential $V(y)$ that changes only close to the surface (edge potential) has a strong effect on the edge-state dispersion: within first-order perturbation theory it leads to a shift $\Delta E(k_x) = \langle \psi(k_x) \middle| V \middle| \psi(k_x) \rangle$. In particular, since bulk states are affected little by the edge potential, the edge-state crossing is shifted by $\Delta E(k_x = 0)$ with

---

[1] One can see from Fig. 4.2(e) that the parallel field generates indirect gapless bulk excitations. These bulk states are, however, expected to be more susceptible to localization compared to the edge states.

respect to the bulk bands. Thus, if the edge potential is much larger than the topological gap, it also leads to a burying of the Dirac point. (The edge potential may also give rise to trivial edge states that are also expected to be insensitive to a magnetic field. In contrast to topological edge states these are not expected to be protected from scattering, leading to a length dependence of the edge conductance [35].)

Figure 4.4 shows the burying of the edge-state Dirac point obtained from a finite-width BHZ model supplemented by an edge potential. We use the BHZ parameters for HgTe of Ref. [37] and a finite-difference tight-binding model, with an extra potential V_{edge} at the outermost lattice point. For $V_{\text{edge}} = 0$ (red lines) we find the usual dispersion with the edge-state crossing in the band gap. A finite $V_{\text{edge}} \neq 0$ (blue lines) leaves the bulk states nearly unchanged, but indeed moves the edge-state crossing into the bulk.

Apart from potentially being physically present in semiconductor devices, we can also use the edge potential purely as a tool that leads to a Dirac-point burying within the BHZ model. This is particularly advantageous for numerical calculations, which are far more costly for a 3D $\mathbf{k}{\cdot}\mathbf{p}$ model.

4.5. QUANTIZED CONDUCTANCE IN STRONG IN-PLANE MAGNETIC FIELDS

So far we have emphasized generic mechanisms for hiding the edge-state Zeeman gap within a bulk band. In such cases, observing a clear field-induced edge-state gap through transport would certainly be challenging. Yet, time-reversal symmetry is broken by an in-plane magnetic field, and backscattering from disorder is allowed also *outside* the edge-state Zeeman gap. Naively, a magnetic field should thus lead to an appreciable breakdown of the conductance quantization.

We will now argue that, in practice, conductance may stay nearly quantized even in very strong magnetic fields ($B \geq 10\text{T}$): from Fermi's golden rule we find that the mean free path of edge states in a disordered potential is given as [38]

$$l_{\text{tr}} = \frac{c\hbar^2 v_{\text{F}}}{V_{\text{dis}}^2 \xi} \left(\frac{\delta\mu}{g_{\text{eff}} B} \right)^2 . \tag{4.4}$$

Here, v_{F} is the edge-state velocity, c is a numerical factor ~ 1, $\delta\mu$ is the energy with respect to the edge-state crossing, and we assumed uncorrelated disorder $\langle V(x)V(x')\rangle = V_{\text{dis}}^2 \xi \delta(x - x')$. In the bulk-insulating regime, burying of the edge-state crossing implies that $\delta\mu$ must be of order or larger than the gap size. Together with the strong suppression of the edge-state g-factor g_{eff} discussed earlier, $(\delta\mu/g_{\text{eff}}B)^2$ then is a large factor. Physically, this suppression of backscattering away from Dirac point originates from the fact that kinetic energy efficiently anti-aligns spins of the edge state away from the Zeeman gap even in presence of magnetic field; recall Fig. 4.1(d). In practice, the suppression of scattering presented here may rival that arising from bona fide topological protection at zero magnetic field.

To further quantify the suppression of backscattering, we have performed conductance calculations for a disordered BHZ model, with and without edge potential, i.e., with and without burying of the Dirac point. As for the results sketched in Fig. 4.4(a), we use the HgTe parameters from Ref. [37], and compute transport through a rectangular region of

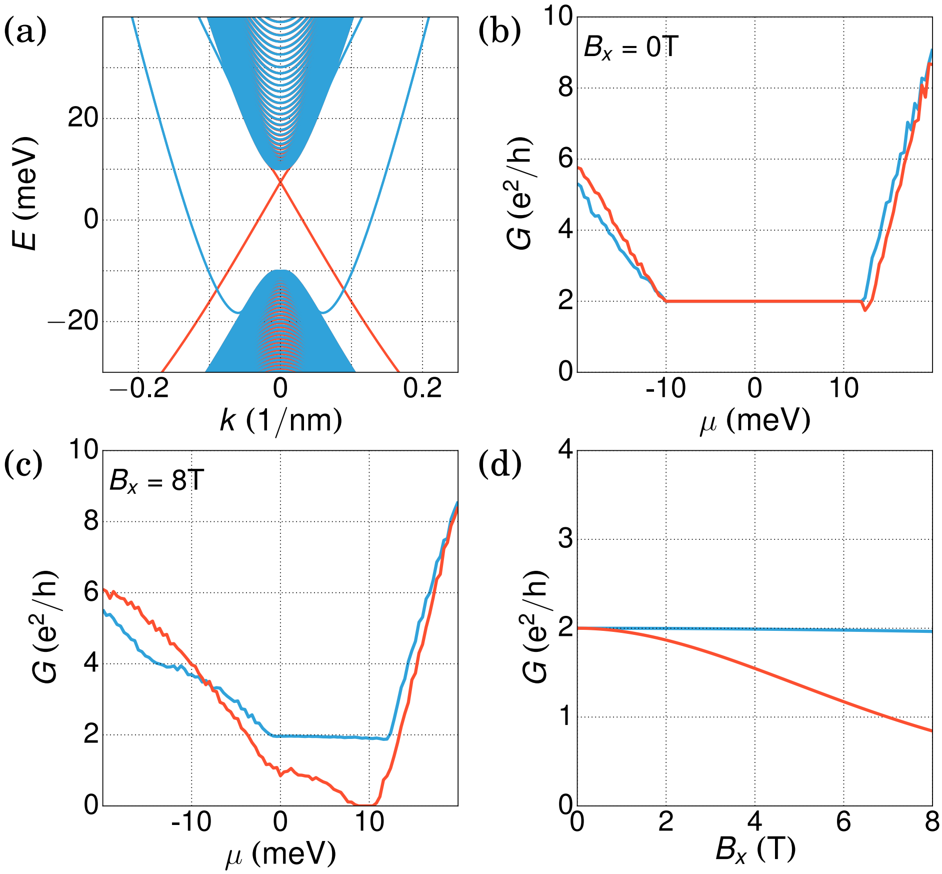

Figure 4.4: (a) Band structure and (b-d) transport calculations for the BHZ model with (blue) and without (red) an additional edge potential V_{edge}. Transport calculations were performed for a disordered system at (b) zero field and (c) with an in-plane field $B_x = 8\,\text{T}$. (d) Transport calculation at fixed $\mu = 3$ meV. All transport calculations are averaged over 50 different disorder realizations, with parameters $V_{\text{edge}} = -0.14\,\text{eV}$, $U_0 = 0.05\,\text{eV}$, $L = 4000\,\text{nm}$, $W = 1000\,\text{nm}$, and finite difference grid spacing $a = 4\,\text{nm}$.

length L and width W. We use a random disorder potential drawn independently for every lattice point from the uniform distribution $[-U_0/2, U_0/2]$, and compute the conductance using Kwant [29]. At zero magnetic field [Fig. 4.4(b)] both models show almost identical transport properties. In particular, the conductance in the gap is perfectly quantized due to topological protection. This behavior changes drastically once a strong in-plane magnetic field is applied [Fig. 4.4(c)]: Without edge potential, the conductance drops well below the quantized value of $2e^2/h$. Disorder leads to backscattering within the complete range of energies in the topological gap (not only the small Zeeman gap opened in the edge-state spectrum). When the edge-state crossing is buried, by contrast, conductance inside the gap stays almost perfectly quantized. This stark contrast can also be seen in Fig. 4.4(d) where we plot conductance as a function of magnetic field for a fixed chemical potential residing in the bulk gap.

4.6. CONCLUSIONS

In contrast to common expectation, we have shown that the edge-state conductance quantization in semiconductor QSH systems can be surprisingly robust against in-plane magnetic fields. This may be a possible explanation for the surprising findings of Ref. [13], and we could expect to find similar robustness in HgTe. Our findings also highlight a challenge for proposals to use QSH edges as a Majorana platform [39, 40]: Localizing Majorana zero modes requires the ability to align the chemical potential within the edge-state Zeeman gap, which could require exceedingly large fields if the Dirac point is buried in a bulk band. A good strategy to overcome this obstacle is to operate in a regime closer to the topological phase transition where the edge-state crossing remains in the gap (if edge potentials are unimportant). Alternative, a side-gate might be used to apply an electrostatic potential to move the Dirac point back in the topological gap. These strategies may also allow one to finally observe a strong in-plane magnetic field dependence that would distinguish topological from trivial edge states—the latter naturally exhibiting little field dependence.

While finishing this work, we became aware of a related preprint [41] that found a hidden Dirac point in the band structure of InAs/GaSb within an effective 6-band model, in qualitative agreement with our full **k·p** calculations.

4.7. SUPPLEMENTARY INFORMATION

4.7.1. **k·p** SIMULATIONS

We use the standard 8 × 8 Kane Hamiltonian [26–28] for semiconductors in our numerical band structure calculations, that we discussed in Section 2.3. The material parameters in this Hamiltonian are position-dependent due to the layered structure, and care has to be taken to symmetrize the Hamiltonian. Following the approach put forward by Burt and Foreman [42, 43], as described in Section 2.3.5.

The band parameters for InAs/GaSb and HgTe quantum wells are given in Table 2.5 and Tabe 2.6, respectively.

We perform all **k·p** simulations by discretizing the Hamiltonian (2.64) using a grid spacing of $a = 0.5\,\mathrm{nm}$. For 2D bulk dispersion we only discretize z-direction, when calculating the edge dispersion we discretize both y- and z-directions. We calculate all band structures by treating momentum k_x as number, which we simple denote as k in the figures.

In all simulations we consider magnetic field $\boldsymbol{B} = B\hat{y}$ along y-direction. We include magnetic field through Zeeman and orbital effect. We add the orbital effect through a vector potential

$$A_x = B(z - z_0)\,, \tag{4.5}$$

where z_0 is a coordinate offset which will be of relevance for finding effective models. We include the vector potential in Hamiltonian by making the substitution

$$k_x \rightarrow k_x + \frac{2\pi}{\phi_0} A_x\,, \tag{4.6}$$

where $\phi_0 = \frac{h}{e}$ is the flux quantum. In the regime of parameters used in simulation this method gives the same results as using Peierl's substitution on the tight-binding level. We decided to use for this route due to its advantages for obtaining effective models that we describe in next section.

4.7.2. HIGHER-ORDER EFFECTIVE MODELS FOR InAs/GaSb

We obtain effective models using quasi-degenerate perturbation theory, also known as Löwdin partitioning [25, 44–46], that we discussed in detail in Section 2.1.2. We use implementation discussed in Section 3.2. We have derived effective models for InAs/GaSb quantum well with layer thickness 12.5 nm/5 nm in Fig. 4.5.

In Fig. 4.5(a) we show the bulk **k**·**p** band structure of this quantum well on a larger energy range. As for the BHZ model, we choose the electron-like state E1 and the heavy-hole state HH1 as the basis of our perturbation theory. Other hole states such as LH1 and HH2 are close, but still further away in energy than the inversion gap. Still, as we will see, they have a significant influence.

We have numerically derived 4×4 effective models with momenta up to second order (this is equivalent to the BHZ model including linear and quadratic spin-orbit terms similar to [47]) and third order. The comparison of the full **k**·**p** band structure with the second order model in Fig. 4.5(b) shows the limits of this approximation clearly: in particular, the hybridization gap is far too small. Only after including third order terms (Fig. 4.5(c)) do we find a satisfactory agreement. These third-order terms are (at least partially) due to interactions with hole states that are further away in energy. These still have a significant influence on the band structure at finite momentum.

In Fig. 4.5(d) we show the dispersion in a strip of finite width W (black lines), with edges along the [100] direction. We observe that the Dirac point of the edge states is clearly buried in the bulk valence band. In particular, we observe that this burying is due to the anisotropy of the hole band structure: the hybridization gap in [110] direction is very different from the hybridization gap in [100] direction. As seen above, to describe this anisotropy faithfully, we needed to take into account the further-away hole bands in the form of higher-order momentum terms.

4.7.3. DERIVATION OF THE SUPPRESSION OF THE EDGE-STATE g-FACTOR

To derive the edge-state wavefunction we start from the BHZ model (4.1), (4.2). In this section we re-derive the results of [24], on which we build our g-factor derivation. The wavefunctions for the edge states decay into the bulk and can be written as

$$\Psi_{1,2} = \Psi_e^{\pm\lambda_{1,2} y}, \tag{4.7}$$

where:

$$\lambda_{1,2}^2 = k_x + F \pm \sqrt{F^2 - (M^2 - E^2)/B_+B_-}, \tag{4.8}$$

$$F = \frac{A^2 - 2(MB + ED)}{2B_+B_-}. \tag{4.9}$$

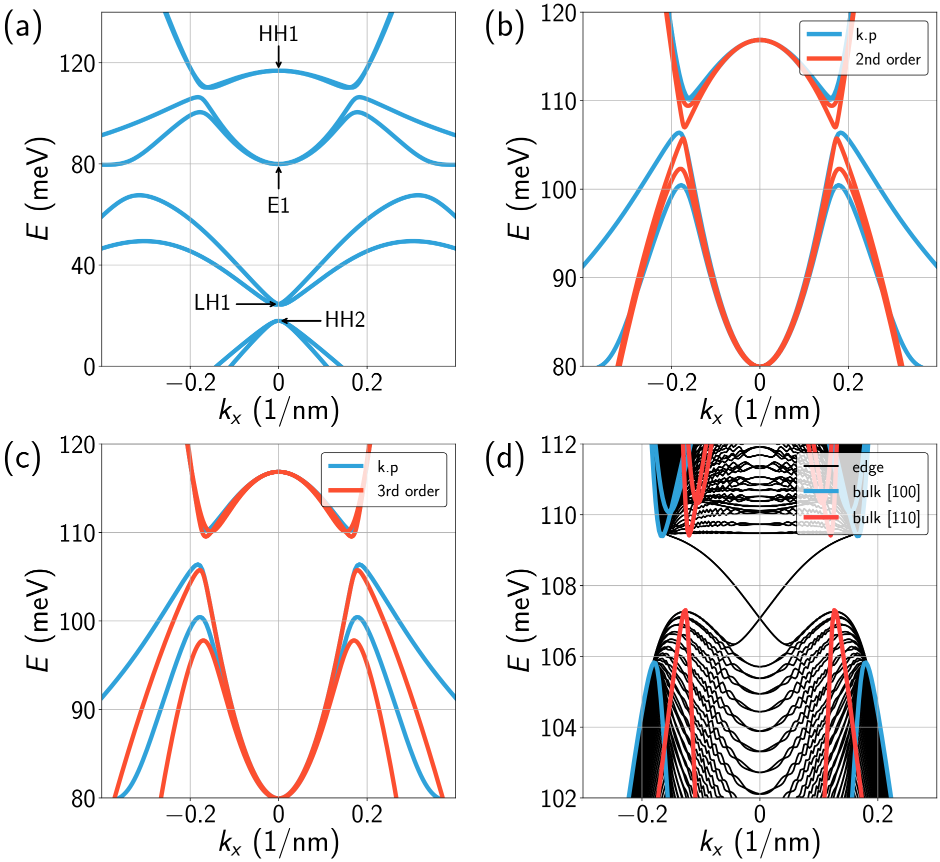

Figure 4.5: Effective models for InAs/GaSb quantum well with layer thickness 12.5 nm/5 nm. (a) **k**·**p** dispersion of 2D system with labelled bands. We compare 2nd order (b) and 3rd (c) continuous dispersions of effective models with exact **k**·**p** dispersion from plot (a). We see that 2nd order effective model underestimates the topological gap, and therefore does not describe properly investigated system. (d) Tight-binding dispersion of bulk (blue) and edge (black) system made from 3rd order effective model. We observe that Dirac point is buried in the valence band. We discretized effective model with grid spacing $a = 2\,\text{nm}$. Width of the system used to simulate edge states is $W = 800\,\text{nm}$.

Plugging this back into the BHZ model (4.1) and (4.2):

$$[M - B_+(k_x^2 - \lambda_{1,2}^2)]\psi_1 + A(k_x \mp \lambda_{1,2})\psi_2 = E\psi_1; \tag{4.10}$$

$$A(k_x \pm \lambda_{1,2})\psi_1 - [M - B_-(k_x^2 - \lambda_{1,2}^2)]\psi_2 = E\psi_2. \tag{4.11}$$

The two spin sectors are different by the sign of A, therefore the decay length is the same for the opposite spins.

Let us now solve for the decaying solutions in half-space $y > 0$ with hard-wall boundary conditions at $y = 0$. The condition that the wavefunction can vanish at the hard wall is the same as requiring linear dependence of the decaying solutions at $y = 0$:

$$(\psi_1/\psi_2)_1 = (\psi_1/\psi_2)_2, \tag{4.12}$$

where outer index is enumerating the decaying solutions $\Psi_{1,2}$. Therefore:

$$\frac{M + E - B_-(k_x^2 - \lambda_1^2)}{A(k_x - \lambda_1)} = \frac{M + E - B_-(k_x^2 - \lambda_2^2)}{A(k_x - \lambda_2)}. \tag{4.13}$$

Let us solve the equation for the crossing point of the edge dispersion, where due to time-reversal symmetry $k_x = 0$, therefore:

$$\lambda_2(M + E + B_0\lambda_1^2) = \lambda_1(M + E + B_0\lambda_2^2). \tag{4.14}$$

Then we use that $\lambda_1\lambda_2 = \sqrt{\frac{M^2-E^2}{B_+B_-}}$, and get:

$$\begin{aligned}(E + M)\lambda_2 + B_-\lambda_1\sqrt{\frac{M^2 - E^2}{B_+B_-}}\\ = (E + M)\lambda_1 + B_-\lambda_2\sqrt{\frac{M^2 - E^2}{B_+B_-}}.\end{aligned} \tag{4.15}$$

This equation has a solution if:

$$E + M - \sqrt{B_-/B_+}\sqrt{M^2 - E^2} = 0. \tag{4.16}$$

Therefore, the crossing is at $E = -M\frac{D}{B}$. Note that the result has correct limit $E = 0$ when the bandstructure is symmetric, $D = 0$.

We now proceed with the solution by computing the matrix element of the Zeeman energy between the two edge states at the crossing point, where the gap is opened. Let us denote $\psi_2/\psi_1 = r$. For opposite spin the ratio is $\psi_2'/\psi_1' = r^*$, therefore if we use the g_e and g_h (electron and hole bulk in-plane g-factors), the effective edge g-factor is:

$$g_{eff} = \frac{g_e + g_h|r|^2}{1 + |r|^2}. \tag{4.17}$$

For the parameters of the crossing point ($E = -MD/B$, $k_x = 0$) we get from (4.13) and (4.16):

$$|r|^2 = \left|\frac{MB_+ + BB_+\lambda_1^2}{MB_- + BB_-\lambda_1^2}\right| = \frac{B_+}{B_-}. \tag{4.18}$$

This gives simply (4.3) from the main text.

4.7.4. NUMERICAL VALUES FOR g-FACTORS IN InAs/GaSb AND HgTe/CdTe QUANTUM WELLS

Using Löwdin partitioning, we compute the g-factor of the electron states in the 4 × 4 model, by doing perturbation in B_y instead of momenta. This is a gauge-invariant quantity in the HgTe quantum wells due to inversion symmetry. However, it becomes gauge-dependent in InAs/GaSb due to the linear spin-orbit terms that are essential in this strongly asymmetric structure. We fix the gauge z_0 by demanding that the off-diagonal matrix elements between E1 and HH1 do not depend on B. This is the same gauge as used in [32].

In Fig. 4.6 we show the bulk g-factors as a function of quantum well width for both types of quantum wells, together with the value of the effective edge g-factor obtained from (4.3) using parameters B and D from the derived effective model. As discussed in the main text we observe a strong suppression of the effective edge g-factor compared to the bulk value.

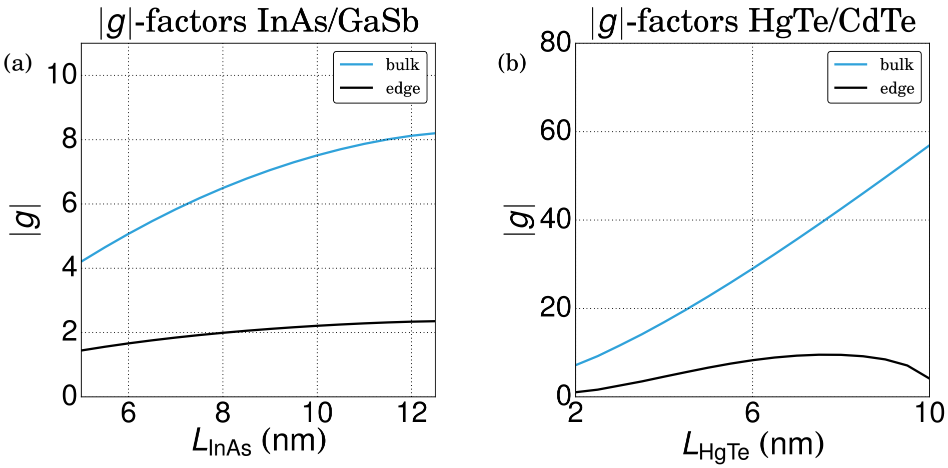

Figure 4.6: bulk and effective edge-state g-factors for (a) InAs/GaSb and (b) HgTe/CdTe quantum wells.

REFERENCES

[1] C. L. Kane and E. J. Mele, *Quantum Spin Hall Effect in Graphene,* Phys. Rev. Lett. **95**, 226801 (2005).

[2] M. Z. Hasan and C. L. Kane, *Colloquium: Topological insulators,* Rev. Mod. Phys. **82**, 3045 (2010).

[3] X.-L. Qi and S.-C. Zhang, *Topological insulators and superconductors,* Rev. Mod. Phys. **83**, 1057 (2011).

[4] B. A. Bernevig, T. L. Hughes, and S.-C. Zhang, *Quantum Spin Hall Effect and Topological Phase Transition in HgTe Quantum Wells,* Science **314**, 1757 (2006).

[5] M. König, S. Wiedmann, C. Brüne, A. Roth, H. Buhmann, L. W. Molenkamp, X.-L. Qi, and S.-C. Zhang, *Quantum Spin Hall Insulator State in HgTe Quantum Wells,* Science **318**, 766 (2007).

[6] A. Roth, C. Brüne, H. Buhmann, L. W. Molenkamp, J. Maciejko, X.-L. Qi, and S.-C. Zhang, *Nonlocal Transport in the Quantum Spin Hall State,* Science **325**, 294 (2009).

[7] C. Brüne, A. Roth, H. Buhmann, E. M. Hankiewicz, L. W. Molenkamp, J. Maciejko, X.-L. Qi, and S.-C. Zhang, *Spin polarization of the quantum spin Hall edge states,* Nat. Phys. **8**, 485 (2012).

[8] K. C. Nowack, E. M. Spanton, M. Baenninger, M. König, J. R. Kirtley, B. Kalisky, C. Ames, P. Leubner, C. Brüne, H. Buhmann, L. W. Molenkamp, D. Goldhaber-Gordon, and K. A. Moler, *Imaging currents in HgTe quantum wells in the quantum spin Hall regime,* Nat. Mater. **12**, 787 (2013).

[9] S. Hart, H. Ren, T. Wagner, P. Leubner, M. Mühlbauer, C. Brüne, H. Buhmann, L. W. Molenkamp, and A. Yacoby, *Induced superconductivity in the quantum spin Hall edge,* Nat. Phys. **10**, 638 (2014).

[10] C. Liu, T. L. Hughes, X.-L. Qi, K. Wang, and S.-C. Zhang, *Quantum Spin Hall Effect in Inverted Type-II Semiconductors,* Phys. Rev. Lett. **100**, 236601 (2008).

[11] I. Knez, R.-R. Du, and G. Sullivan, *Evidence for Helical Edge Modes in Inverted* InAs/GaSb *Quantum Wells,* Phys. Rev. Lett. **107**, 136603 (2011).

[12] I. Knez, C. T. Rettner, S.-H. Yang, S. S. Parkin, L. Du, R.-R. Du, and G. Sullivan, *Observation of Edge Transport in the Disordered Regime of Topologically Insulating* InAs/GaSb *Quantum Wells,* Phys. Rev. Lett. **112**, 026602 (2014).

[13] L. Du, I. Knez, G. Sullivan, and R.-R. Du, *Robust Helical Edge Transport in Gated* InAs/GaSb *Bilayers,* Phys. Rev. Lett. **114**, 096802 (2015).

[14] V. S. Pribiag, A. J. A. Beukman, F. Qu, M. C. Cassidy, C. Charpentier, W. Wegscheider, and L. P. Kouwenhoven, *Edge-mode superconductivity in a two-dimensional topological insulator,* Nat. Nano **10**, 593 (2015).

[15] F. Qu, A. J. Beukman, S. Nadj-Perge, M. Wimmer, B.-M. Nguyen, W. Yi, J. Thorp, M. Sokolich, A. A. Kiselev, M. J. Manfra, C. M. Marcus, and L. P. Kouwenhoven, *Electric and Magnetic Tuning Between the Trivial and Topological Phases in InAs/GaSb Double Quantum Wells,* Phys. Rev. Lett. **115**, 036803 (2015).

[16] S. Mueller, A. N. Pal, M. Karalic, T. Tschirky, C. Charpentier, W. Wegscheider, K. Ensslin, and T. Ihn, *Nonlocal transport via edge states in InAs/GaSb coupled quantum wells,* Phys. Rev. B **92**, 081303 (2015).

[17] F. Couëdo, H. Irie, K. Suzuki, K. Onomitsu, and K. Muraki, *Single-edge transport in an InAs/GaSb quantum spin Hall insulator,* Phys. Rev. B **94**, 035301 (2016).

[18] M. Karalic, S. Mueller, C. Mittag, K. Pakrouski, Q. Wu, A. A. Soluyanov, M. Troyer, T. Tschirky, W. Wegscheider, K. Ensslin, and T. Ihn, *Experimental signatures of the inverted phase in InAs/GaSb coupled quantum wells,* Phys. Rev. B **94**, 241402 (2016).

[19] L. Du, T. Li, W. Lou, X. Wu, X. Liu, Z. Han, C. Zhang, G. Sullivan, A. Ikhlassi, K. Chang, and R.-R. Du, *Tuning Edge States in Strained-Layer* InAs/GaInSb *Quantum Spin Hall Insulators,* Phys. Rev. Lett. **119**, 056803 (2017).

[20] L. Tiemann, S. Mueller, Q.-S. Wu, T. Tschirky, K. Ensslin, W. Wegscheider, M. Troyer, A. A. Soluyanov, and T. Ihn, *Impact of strain on the electronic properties of InAs/GaSb quantum well systems,* Phys. Rev. B **95**, 115108 (2017).

[21] H. Zhang, C.-X. Liu, X.-L. Qi, X. Dai, Z. Fang, and S.-C. Zhang, *Topological insulators in* Bi_2Se_3, Bi_2Te_3 *and* Sb_2Te_3 *with a single Dirac cone on the surface,* Nat. Phys. **5**, 438 (2009).

[22] D. Hsieh, Y. Xia, D. Qian, L. Wray, F. Meier, J. H. Dil, J. Osterwalder, L. Patthey, A. V. Fedorov, H. Lin, A. Bansil, D. Grauer, Y. S. Hor, R. J. Cava, and M. Z. Hasan, *Observation of Time-Reversal-Protected Single-Dirac-Cone Topological-Insulator States in* Bi_2Te_3 *and* Sb_2Te_3, Phys. Rev. Lett. **103**, 146401 (2009).

[23] C. Brüne, C. X. Liu, E. G. Novik, E. M. Hankiewicz, H. Buhmann, Y. L. Chen, X. L. Qi, Z. X. Shen, S. C. Zhang, and L. W. Molenkamp, *Quantum Hall Effect from the Topological Surface States of Strained Bulk HgTe,* Phys. Rev. Lett. **106**, 126803 (2011).

[24] B. Zhou, H.-Z. Lu, R.-L. Chu, S.-Q. Shen, and Q. Niu, *Finite Size Effects on Helical Edge States in a Quantum Spin-Hall System,* Phys. Rev. Lett. **101**, 246807 (2008).

[25] R. Winkler, *Spin-Orbit Coupling Effects in Two-Dimensional Electron and Hole Systems* (Springer, Berlin, Heidelberg, 2003).

[26] E. O. Kane, *Band structure of indium antimonide,* J Phys Chem Solids **1**, 249–261 (1957).

[27] E. O. Kane, *Semiconductors and Semimetals,* in *Physics of III-V-Compounds*, Vol. 1, edited by R. K. Willardson and A. C. Beer (Academic Press, New York, London, 1966) pp. 75–100.

[28] G. Bastard, *Wave Mechanics Applied to Semiconductor Heterostructures* (Wiley, New York, 1988).

[29] C. W. Groth, M. Wimmer, A. R. Akhmerov, and X. Waintal, *Kwant: a software package for quantum transport,* New J. Phys. **16**, 063065 (2014).

[30] M. J. Yang, C. H. Yang, B. R. Bennett, and B. V. Shanabrook, *Evidence of a Hybridization Gap in "Semimetallic" InAs/GaSb Systems,* Phys. Rev. Lett. **78**, 4613 (1997).

[31] L.-H. Hu, D.-H. Xu, F.-C. Zhang, and Y. Zhou, *Effect of in-plane magnetic field and applied strain in quantum spin Hall systems: Application to InAs/GaSb quantum wells,* Phys. Rev. B **94**, 085306 (2016).

[32] L.-H. Hu, C.-X. Liu, D.-H. Xu, F.-C. Zhang, and Y. Zhou, *Electric control of inverted gap and hybridization gap in type-II InAs/GaSb quantum wells,* Phys. Rev. B **94**, 045317 (2016).

[33] D. C. Tsui, *Observation of Surface Bound State and Two-Dimensional Energy Band by Electron Tunneling,* Phys Rev Lett **24**, 303–306 (1970).

[34] M. Noguchi, K. Hirakawa, and T. Ikoma, *Intrinsic electron accumulation layers on reconstructed clean InAs(100) surfaces,* Phys Rev Lett **66**, 2243–2246 (1991).

[35] F. Nichele, H. J. Suominen, M. Kjaergaard, C. M. Marcus, E. Sajadi, J. A. Folk, F. Qu, A. J. A. Beukman, F. K. d. Vries, J. v. Veen, S. Nadj-Perge, L. P. Kouwenhoven, B.-M. Nguyen, A. A. Kiselev, W. Yi, M. Sokolich, M. J. Manfra, E. M. Spanton, and K. A. Moler, *Edge transport in the trivial phase of InAs/GaSb,* New J. Phys. **18**, 083005 (2016).

[36] S. Mueller, C. Mittag, T. Tschirky, C. Charpentier, W. Wegscheider, K. Ensslin, and T. Ihn, *Edge transport in InAs and InAs/GaSb quantum wells,* Phys. Rev. B **96**, 075406 (2017).

[37] M. König, H. Buhmann, L. W. Molenkamp, T. Hughes, C.-X. Liu, X.-L. Qi, and S.-C. Zhang, *The Quantum Spin Hall Effect: Theory and Experiment,* J. Phys. Soc. Jpn. **77**, 031007 (2008).

[38] D. Pikulin and T. Hyart, *Interplay of Exciton Condensation and the Quantum Spin Hall Effect in* InAs/GaSb *Bilayers,* Phys. Rev. Lett. **112**, 176403 (2014).

[39] L. Fu and C. L. Kane, *Josephson current and noise at a superconductor/quantum-spin-Hall-insulator/superconductor junction,* Phys. Rev. B **79**, 161408 (2009).

[40] J. Alicea, *New directions in the pursuit of Majorana fermions in solid state systems,* Rep. Prog. Phys. **75**, 076501 (2012).

[41] C.-A. Li, S.-B. Zhang, and S.-Q. Shen, *Hidden edge Dirac point and robust quantum edge transport in InAs/GaSb quantum wells,* ArXiv170901645 Cond-Mat (2017), arXiv:1709.01645 [cond-mat] .

[42] M. G. Burt, *The justification for applying the effective-mass approximation to microstructures,* J. Phys. Condens. Matter **4**, 6651 (1992).

[43] B. A. Foreman, *Elimination of spurious solutions from eight-band $k \cdot p$ theory,* Phys. Rev. B **56**, R12748–R12751 (1997).

[44] P. Löwdin, *A Note on the Quantum-Mechanical Perturbation Theory,* J. Chem. Phys. **19**, 1396–1401 (1951).

[45] J. M. Luttinger and W. Kohn, *Motion of Electrons and Holes in Perturbed Periodic Fields,* Phys Rev **97**, 869–883 (1955).

[46] G. L. Bir and G. Pikus, *Symmetry and strain-induced effects in semiconductors* (New York, Wiley, 1974).

[47] D. G. Rothe, R. W. Reinthaler, C.-X. Liu, L. W. Molenkamp, S.-C. Zhang, and E. M. Hankiewicz, *Fingerprint of different spin–orbit terms for spin transport in HgTe quantum wells,* New J. Phys. **12**, 065012 (2010).

5

SPIN-ORBIT INTERACTION IN A DUAL GATED InAs/GaSb QUANTUM WELL

This chapter, with exception of Section 5.3.2, has been previously published as Arjan J. A. Beukman, Folkert K. de Vries, Jasper van Veen, **Rafal Skolasinski**, Michael Wimmer, Fanming Qu, David T. de Vries, Binh-Minh Nguyen, Wei Yi, Andrey A. Kiselev, Marko Sokolich, Michael J. Manfra, Fabrizio Nichele, Charles M. Marcus, Leo P. Kouwenhoven, *Spin-orbit interaction in a dual gated InAs/GaSb quantum well*, Phys. Rev. B **96**, 241401(R) (2017).

5.1. INTRODUCTION

The semiconductors InAs and GaSb have small band gaps together with a crystal inversion asymmetry resulting from their zincblende structure. These materials are therefore predicted to have strong spin-orbit interaction (SOI) [1, 2] which has been measured experimentally [3]. Moreover, tuning of the Rashba strength by electrostatic gating has been shown for InAs quantum wells [4, 5]. Strong and in-situ control over SOI is a promising route towards novel spintronic devices [2, 6, 7], and strong SOI together with a large g-factor and induced superconductivity are ingredients for a topological superconducting phase [8].

Combining InAs and GaSb in a quantum well gained much interest because of the type-II broken-gap band alignment [9]. As a result, the GaSb valence band maximum is higher in energy than the InAs conduction band minimum, opening a range of energies where electrons in the InAs coexist with holes in the GaSb. The spatial separation of these electron and hole gases allows for tunability of the band alignment using an electric field. Therefore, a rich phase diagram can be mapped out using dual gated devices [10, 11]. Although spatially separated, strong coupling between the materials allows for electron-hole hybridization which opens a gap in the energy spectrum when the density of electrons equals that of holes [12, 13], driving the band structure topologically non-trivial [10].

Interestingly, the magnitude of this hybridization gap is spin dependent due to SOI [14–16]. Therefore, a spin polarized state is seen at energies close to the hybridization gap [17] and at higher energies a dip in the spin-splitting is expected [18]. The latter has yet to be observed and indicates a competition between electron-hole hybridization and spin-orbit interaction. Here, we experimentally study SOI through the difference in density of the spin-orbit split bands of an InAs/GaSb quantum well. This zero-field density difference (Δn_{ZF}) is extracted from magnetoresistance measurements. First, SOI is investigated in the regime where the GaSb is depleted from carriers. Rashba and Dresselhaus SOI strengths can be extracted from measurements of Δn_{ZF}. Second, SOI is investigated just above the hybridization gap where Δn_{ZF} almost vanishes, consistent with band structure calculations.

5.2. EXPERIMENT DETAILS

5.2.1. MATERIAL

A 20 µm wide and 80 µm long Hall bar device is defined using chemical wet etching techniques. A top gate is separated from the mesa by a 80 nm thick $\mathrm{SiN_x}$ dielectric layer. The Hall bar is fabricated from the same wafer used in Ref. [11, 19]. The quantum well consists of 12.5 nm InAs and 5 nm GaSb between 50 nm AlSb barriers. The doped GaSb substrate acts as a back gate. All measurements are done at 300 mK using standard lock-in techniques with an excitation current of 50 nA.

5.2.2. PHASE DIAGRAM

Figure 5.1 presents the longitudinal resistance of the Hall bar device as a function of top gate voltage V_{tg} and back gate voltage V_{bg}. The measurement is performed in 2 T perpendicular magnetic field and therefore shows quantum oscillations resulting from

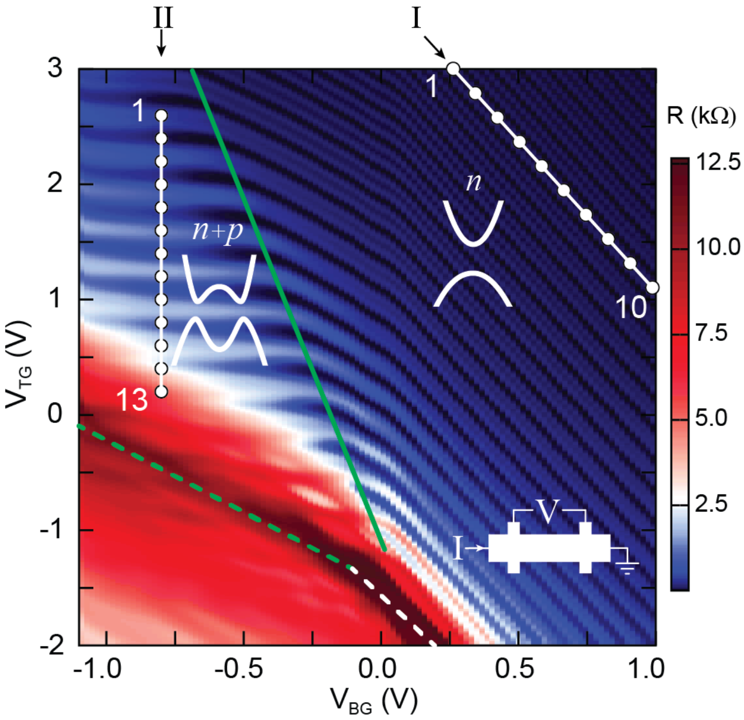

Figure 5.1: Longitudinal resistance of the Hall bar device (see bottom right inset) as a function of top gate voltage (V_{tg}) and back gate voltage (V_{bg}) at 2 T out of plane magnetic field. Oscillations in resistance originate from Landau levels and denote lines of constant electron density. The dashed green and white lines indicate regions with the Fermi level located inside an energy gap. The solid green line separates the region with electrons as carriers (right) from a region where electrons and holes coexist (left). Line I is situated in the electron regime and Line II in the two-carrier regime. The insets show the schematic band alignment for both cases.

the changing electron density. Quantum oscillations corresponding to holes are less pronounced as the mobility of holes in this system is much lower than the mobility of electrons [11]. For lines parallel to these oscillations, such as line I in Fig. 1a, the electron density is constant while the electric field changes. Regions of high resistance, indicated by the dashed white and green lines, correspond to having the Fermi level inside an energy gap. A detailed description of the phase diagram obtained from measurements on the same wafer was reported by Qu et al. [11].

The green solid line in Fig. 5.1 divides the phase diagram in two regimes. Right of this line is the electron-only regime, where the GaSb is depleted. The system effectively is an asymmetric InAs quantum well with a trivial band alignment and a Fermi level residing in the conduction band (see inset of Fig. 1a). In this regime we investigate Δn_{ZF} along line I, where the electron mobility is highest while only the lowest subband remains occupied. The regime at the left of the green line is the two-carriers regime where electrons and holes coexist. Line II is chosen to evaluate Δn_{ZF} close to the hybridization gap (highlighted by the dashed green line). Before discussing the spin-orbit interaction in the two-carriers regime (along line II) we first study the electron-only regime (line I).

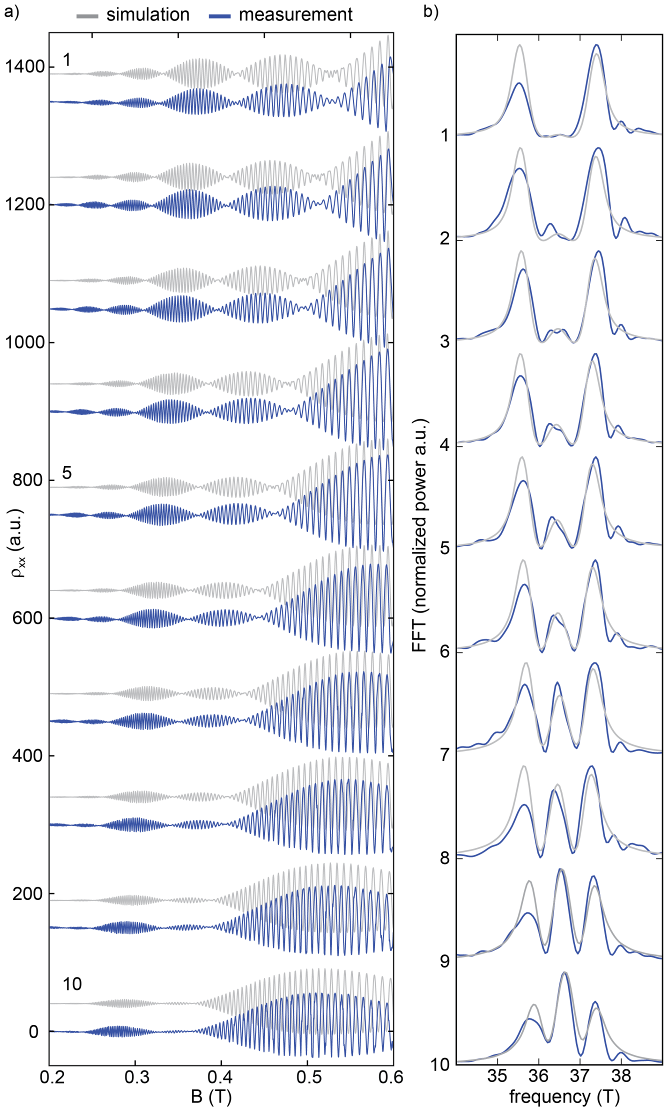

Figure 5.2: (a) Measured magnetoresistance traces (blue) for points 1-10 along line I together with the simulated traces (gray). The simulated traces are offset 40 a.u. from the measured traces; the measured traces are offset by 150 a.u. from each other. The value of Rashba spin-orbit interaction strength α is linearly changed from 73 to 53 mVÅ going from trace 1 to 10. The linear and cubic Dresselhaus interaction strength are kept constant at $\beta = 28.5$ mVÅ and $\gamma = 0$ mVÅ^3. (b) Corresponding Fourier transforms of the measured traces (blue) and simulated traces (gray), i.e. a reproduction of Fig. 3c.

5.3. ELECTRON REGIME

Figure 5.2 (a) shows magnetoresistance traces for 10 points along line I. The density of electrons is fixed, while the electric field is changed. We first consider trace 1. Clear oscillations in the longitudinal resistance R_{xx} are observed as a function of perpendicular magnetic field B modulated by a beat pattern. These Shubnikov-de Haas (SdH) oscillations appear for each single spin band and are periodic in $1/B$ with a frequency that relates to the carrier density via $n = e/h \cdot f$ [3, 20]. The beat modulation observed in trace 1 is caused by two slightly different SdH frequencies f_1 and f_2. This is also evident from the fast Fourier transform (FFT) of the magnetoresistance trace $\mathcal{F}[R_{xx}(1/B)]$ presented in the first curve of Fig. 5.2 (b). These two SdH frequencies indicate two distinct densities n_1 and n_2, that corresponds to different spin species.

Upon moving from point 1 to 10 along line I, two trends are observed. First, an extra frequency peak emerges in the FFTs at $(f_1 + f_2)/2$. This originates from the asymmetry between adjacent beats in the SdH oscillations, visible both in amplitude and number of oscillations of beats A and B in Fig. 5.2 (a). Second, the spacing between the outer peaks in the FFT spectrum decreases, evident from decreasing Δn_{ZF} over line I in Fig. 5.2 (c). This arises from an increasing number of oscillations in both beats A and B, which also pushes the beat nodes to lower magnetic fields. Before we extract the actual SOI strengths and show its electric field dependence, we first elucidate the origin of the emerging center frequency peak.

The center frequency, interestingly, does not correspond to an actual density. The sum of the densities n_1 and n_2 (corresponding to the outer peaks in the FFT) still equals the Hall density. There are, however, mechanisms involving scattering between Fermi-surfaces that can result in extra frequency components. Such mechanisms are magnetic inter subband scattering (MIS) [21, 22], magnetophonon resonances (MPR) [23, 24] and magnetic breakdown (MB) [25–27].

We exclude MIS and MPR. By changing electron density all the frequency peak positions shift with equal strength. However, the oscillation frequency of MIS and MPR is determined by the subband spacing and a specific phonon frequency, respectively. Both do not depend on the electron density. In contrast, for MB the spurious peak always appears in between f_1 and f_2. Magnetic breakdown explains this spurious central peak as carriers tunneling between spin polarized Fermi-surfaces at spin-degeneracy points. The interplay of Dresselhaus and Rashba SOI in our heterostructure could lead to such an anisotropic Fermi surface [25, 28]. As the ratio of Rashba and Dresselhaus SOI strengths approaches 1 magnetic breakdown is enhanced and a central peak is expected [25]. In order to confirm this hypothesis, we extract the individual Rashba and Dresselhaus contributions by comparing our data to quantum mechanical Landau level simulations that include the MB mechanism.

5.3.1. LANDAU LEVEL SIMULATION

The quantum well in this electron-only regime is modeled by a Hamiltonian with spin-orbit interaction in 2D electron systems subject to a perpendicular magnetic field B, as given by [1, 2]:

$$
\begin{aligned}
H = &\frac{\hbar^2}{2m^*}(k_x^2 + k_y^2)\sigma_0 + \alpha(k_y\sigma_x - k_x\sigma_y) + \beta(k_x\sigma_x - k_y\sigma_y) \\
&+ \gamma(k_y k_x k_y \sigma_x - k_x k_y k_x \sigma_y) + \frac{1}{2} g\mu_B B_z \sigma_z,
\end{aligned} \tag{5.1}
$$

where $k_i \to k_i + (e/\hbar)A_i$ is the canonical momentum, σ_i Pauli spin matrices, α, β, γ the Rashba, linear Dresselhaus and cubic Dresselhaus coefficients, respectively, $\hbar$ the reduced Planck's constant, μ_B the Bohr magneton. An electron effective mass of $m^* = 0.04m_0$ is measured from the temperature dependence of the SdH oscillations and a g-factor of -11.5 is used in the calculations [29].[1] We solve for the Landau level energies in a perpendicular magnetic field B_z and extract the resistivity as a function of magnetic field. For calculations used to simulate the magnetoresistance traces to extract the Rashba and Dresselhaus coefficients as shown in Fig. 5.2, we closely follow the method present in Ref. [30] and Chapter 4 of Ref. [1].

For the perpendicular magnetic field $B = (0, 0, B_z)$, the symmetric gauge $\mathbf{A}(x, y) = \frac{B_z}{2}(-y, x, 0)$ is used. The canonical momentum can be written as

$$
k_i = -\mathrm{i}\partial_i + (e/\hbar)\mathbf{A}_i. \tag{5.2}
$$

Raising and lowering operators are defined as

$$
\begin{aligned}
a^\dagger &= \frac{\lambda_c}{\sqrt{2}}\left(k_x + i k_y\right), \\
a &= \frac{\lambda_c}{\sqrt{2}}\left(k_x - i k_y\right),
\end{aligned} \tag{5.3}
$$

where $\lambda_c = \sqrt{\hbar/eB}$ is the magnetic length. The raising operators act on the Landau levels, i.e. $a^\dagger|n,\uparrow\rangle = \sqrt{n+1}|n+1,\uparrow\rangle$. The momentum operators are rewritten in the raising and lowering operators, which are then substituted into the Hamiltonian. We take a basis of $N = 400$ Landau levels in order to capture magnetic fields $\gtrsim 0.1$ T for the electron density $n_s \simeq 17.6 \cdot 10^{15}$ m^{-2}. Solving the Hamiltonian results in the Landau level energies at a particular magnetic field $E(n, B_z)$.

Following Luo et al. [30] the conductance is written as:

$$
\sigma_{xx} = \frac{e^2}{\pi^2\hbar} \sum_{n,\uparrow\downarrow} \left(n \pm \frac{1}{2}\right) \exp\left(-\frac{(E_f - E_{n,\uparrow\downarrow})^2}{\Gamma^2}\right). \tag{5.4}
$$

We assume a fixed Fermi energy at $E_f = (\pi\hbar^2 n_s)/m^*$. To obtain the resistivity we use the approximation that for quantizing magnetic fields $\left(\sigma_{xy}^2 \gg \sigma_{xx}^2\right)$ the transverse resistivity ρ_{xx} is given as [30]:

$$
\rho_{xx} = \sigma_{xx}/(\sigma_{xy}^2 + \sigma_{xx}^2) \approx \sigma_{xx}/\sigma_{xy}^2 \approx \sigma_{xx}(B_z/en_s)^2 \tag{5.5}
$$

---

[1] Note that this g-factor value of -11.5 is measured on a slightly different stack with an InAs layer of 11.0 nm thick. We have checked in the simulations that changing the g-factor to -5 or -15 has negligible influence on the SdH oscillations.

The parameters α, β, γ in the model are estimated and fine tuned to match the node positions and the number of oscillations in a beat of the measured SdH traces. Figure 5.2 (a, b) shows the measured SdH data together with the simulated data for traces 1 and 10. Trace 1 is fitted with $\alpha_1 = 75$ meVÅ, $\beta_1 = 28.5$ meVÅ, $\gamma_1 = 0$ meVÅ^3 and trace 10 is fitted with $\alpha_{10} = 53$ meVÅ , $\beta_{10} = 28.5$ meVÅ ,$\gamma_{10} = 0$ meVÅ^3. The node positions and amplitude modulation of the simulated data agrees well with the measured SdH oscillations.

Curiously, only good fits are obtained when setting the cubic Dresselhaus term γ to zero. In 2D systems, β is related to γ via $\beta = \langle k_z^2 \rangle \gamma$, where $\langle k_z^2 \rangle \approx (\pi/d)^2$ is the expectation value of the transverse momentum [1, 2] in a quantum well of thickness d. So γ should be non-zero. Currently we do not understand this discrepancy. A recent experimental study on a similar material system also found that the cubic Dresselhaus term could be neglected [31].

Now we consider all traces (1-10) and show that the two trends of Fig. 5.2 (emerging center FFT peak and approaching outer FFT peaks) are reproduced by changing only the Rashba SOI strength. Figure 5.2 (c) shows the FFTs of the simulated traces where α is linearly interpolated between α_1 and α_{10} while fixing $\beta = 28.5$ meVÅ and $\gamma = 0$ meVÅ^3. Linear interpolation is used because the electric field changes linearly along line I, and Rashba SOI strength depends linearly on electric field [1, 32, 33]. All simulated FFTs and the SdH traces match the measured data very well, clearly reproducing the emerging central peak and the approaching outer peaks.

5.3.2. **k·p** SIMULATION

We now model the system using **k·p**-method, that we discussed in Section 2.3, adding to the Hamiltonian previously omitted Dresselhaus term [1]. The system consists of 12.5/5 nm InAs/GaSb quantum well, surrounded by 5 nm of AlSb. We tune the system into the single carrier regime by applying a constant electric field along the growth direction.

In Figure 5.3 (a) and (b) we show band structure of the system far and close to phase transition, respectively. We read the spin-orbit coefficients α and β from the effective models obtained using quasi-degenerate perturbation theory with method described in Section 3.2. The **k·p**-simulation stands in qualitative agreement with the results of the Landau level simulation—the Rashba coefficient α can be tuned by the electric field, whereas effect on the linear Dresselhaus coefficient β is neglectable.

5.4. TWO-CARRIERS REGIME

In the remainder of this paper we switch to the two-carriers regime, located left of the solid green line in Fig. 5.1. Electrons in InAs are present alongside with holes in GaSb (n+p). Here we study the influence of the hybridization of electrons with holes on Δn_{ZF} by investigating magnetoresistance traces on the points 1-13 along line II.

Before continuing with the measured magnetoresistance traces, it is insightful to examine the expected band structures at points 1 and 13, as illustrated in Fig. 5.4 (b). The first point of line II is located near the boundary between the two-carrier and single carrier regimes. A small amount of holes with a large amount of electrons is present. At point 13, close to the hybridization gap, the electron and hole densities are roughly equal, hence the Fermi level E_f is close to the hybridization gap. Note also that k_{cross} decreases

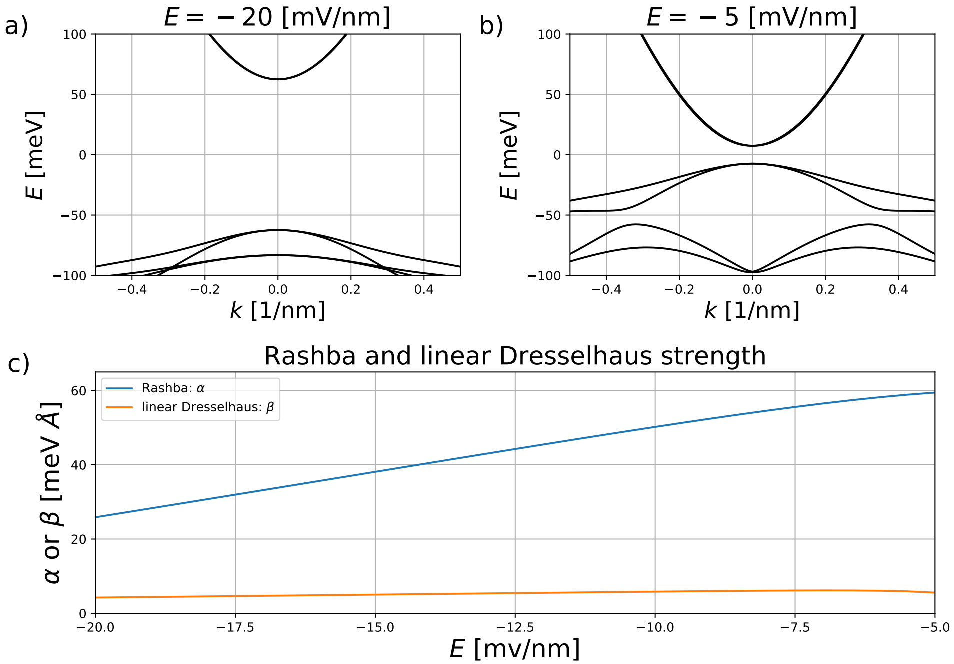

Figure 5.3: Numerical calculation of the spin-orbit interaction in InAs/GaSb quantum well. Applied electric field tunes system into the single-carrier regime (non inverted band structure). (a, b) Band structure along the [100] direction. (c) Strength of the Spin-orbit interaction in function of applied electric field. Rashba coefficient α (blue) reacts strongly to applied electric field, whereas effect on linear Dresselhaus coefficient β (yellow) is almost neglectable.

from 1 to 13, since the electric field changes.

Figure 5.4 (a) shows the magnetoresistance traces 1-13 along line II. Starting from trace 1 towards trace 13 we find series of traces with or without beating, depicted in blue and red respectively. For traces 1 to 3, at large electron density, beating is observed from which we extract $\Delta n_{ZF} = 1.7 \cdot 10^{14}$ m^{-2}.[2] Remarkably trace 4 and 5 do not show any beating, therefore no zero-field density difference can be extracted. For traces 6 to 10, the beating revives showing strong beating. Finally, traces 11-13 show no beating. Figure 5.4 (c) depicts the extracted Δn_{ZF} along line II, which shows a non-monotonic behaviour as a function of gate voltage along line II.

In order to understand this non-monotonic Δn_{ZF} near the hybridization gap (points 1-10) we performed band structure calculations of our InAs/GaSb quantum well. The Δn extracted from these calculations is plotted in Fig. 5.4 (d), which qualitatively agree with the observed dip in Δn_{ZF} at points 4 and 5, Fig. 5.4 (c). In order to understand the simulated Δn, the band structure near the hybridization gap is depicted in the inset of Fig. 5.4 (d) (zoom-in in Fig. 5.4 (b) indicated by the red box). The blue and red lines repre-

---

[2] We cannot directly extract the spin-orbit strength from this Δn by comparing to the single-carrier case, since the effective mass in this region is unknown.

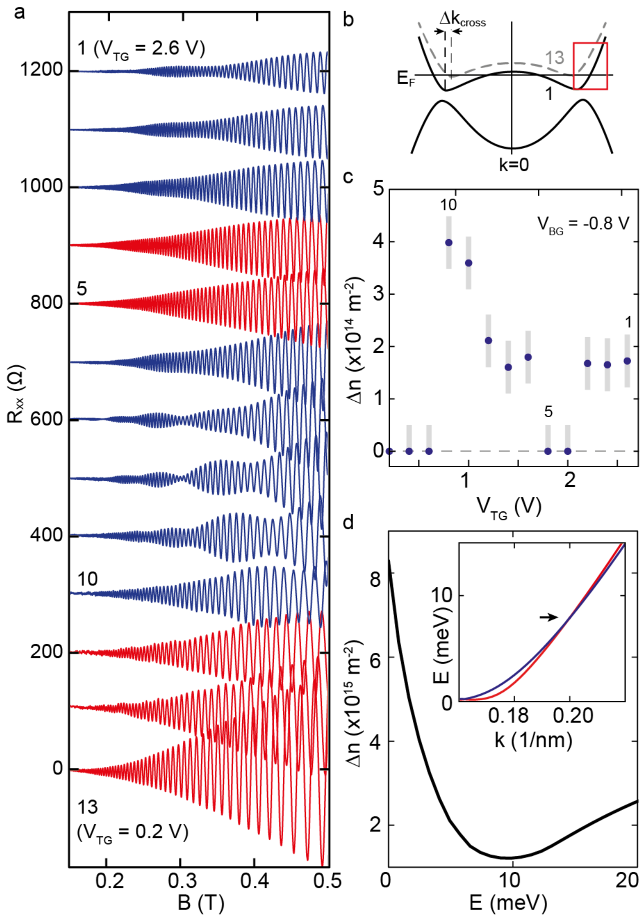

Figure 5.4: Spin-splitting in the two-carrier regime. (a) Magnetoresistance traces for points 1 to 13 along line II indicated in Fig. 1. For each trace the $R_{xx}(B = 0)$ background resistance is subtracted and afterwards the traces are offset by 100 Ω. Beating is (not) observed for (red) blue colored traces. (b) Schematic band structure tuning when moving from point 1 to 13. (c) Δn_{ZF} extracted from the Fourier transform of magnetoresistance traces of (a). Error bars are indicated by the light blue bar. (d) Δn_{ZF} extracted from band structure calculation for our InAs/GaSb quantum well at zero electric field. The inset shows the corresponding band structure in the [100] direction.

sent different spin bands. The bands cross at the black arrow, indicating the vanishing of Δn, such as observed in the experiment. We found this feature to be robust for different electric fields and crystal directions. Interestingly, the crossing of spin bands implies a sign change in SOI strength. Opposite signs of SOI can thus be reached by adjusting the chemical potential. Usually, electric fields are applied to reach such a sign change [34].

Note that only qualitative comparison between experiment and calculations is possible as only the Fermi-energy is varied in the simulation, while in the experiment the band structure (k_{cross}) and Fermi-energy are expected to change. The fact that Δn_{ZF} in

Fig. 5.4 (d) does not completely vanish is because the crossing of the spin bands in the [110] occurs at a slightly different energy than in the [100] direction.

The lack of beating of traces 11-13 is not captured with the simulation. There are two possible reasons for this deviation. First, a strong asymmetry in SdH amplitudes of the two spin species ($A_{\mathrm{up}} \gg A_{\mathrm{down}}$) determines the visibility of the beating pattern. The single spin band SdH oscillation amplitude depends on effective mass m^* and scattering time according to $A_{\mathrm{SdH}} \sim (eB/m^*)^3 \exp(-\pi/\omega_c\tau)$ [30]. Both effective mass and scattering time for the two spin bands become very dissimilar when approaching the hybridization gap, as a result that the beating visibility is reduced to below the experimentally detectable visibility. Second, Nichele et al. [17] shows there is an energy window with only one single spin band present. In such spin polarized state no beating can occur. Here, we cannot discriminate between these two reasons that explain the lack of beating in traces 11-13.

5.5. CONCLUSIONS

In conclusion, we presented a study of the spin-orbit interaction in an InAs/GaSb double quantum well. The Fermi-level and band structure are altered by top and bottom gates. In the electron-only regime we find a electric field tunable spin-orbit interaction, and extract the individual Rashba and Dresselhaus terms. In the two-carriers regime we observe a non-monotonic behavior of the spin splitting which we trace back to the crossing of the spin bands due to the hybridization of electrons and holes.

5.6. SUPPLEMENTARY INFORMATION

5.6.1. FOURIER TRANSFORMS

The Fourier transforms in this manuscript are obtained using the method described here. Starting from a magnetoresistance curve, first a magnetic field range is chosen. The lower bound is fixed at 0.15 T. The upper bound is chosen such that the interval ends at 40% of a beat maximum. Truncating the signal in this way causes minimal deviation from the true frequency components. Next, the background resistance is estimated using a 6th order polynomial fit, which subsequently is subtracted from the signal. The remaining signal is interpolated on a uniform grid in $1/B$ and padded with zeros on both sides. No extra window function is applied. A fast Fourier transform converts the signal to the frequency domain $R(\omega)$ and the power spectrum is obtained using $P(\omega) = R(\omega) \times R^*(\omega)$. All Fourier transforms are normalized such that the maximum is 0.8 a.u.

5.6.2. BAND STRUCTURE CALCULATIONS FOR MULTIPLE ELECTRIC FIELDS

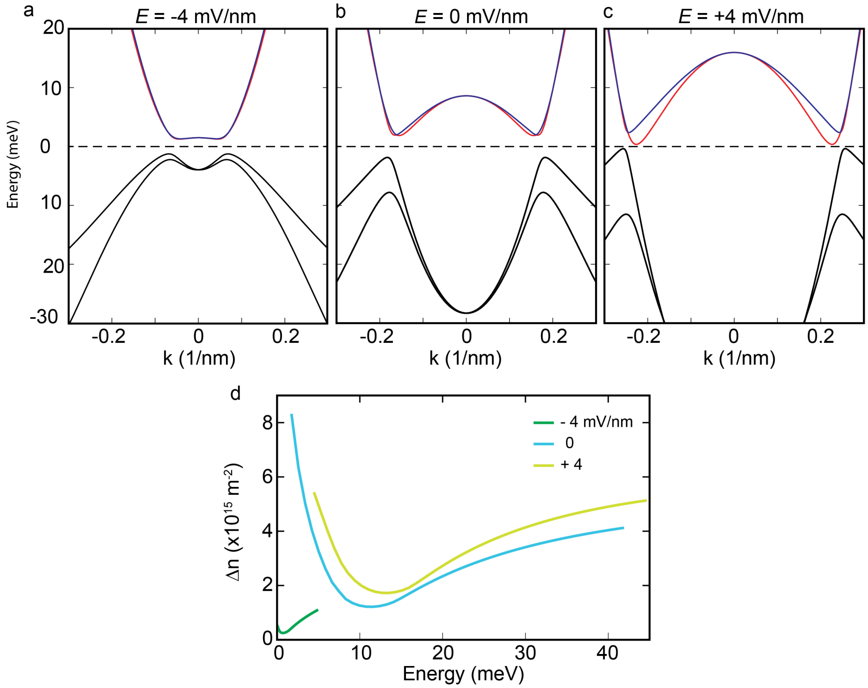

Figure 5.5: (a-c). Result of band structure calculations along [100] for electric fields $\vec{E} = -4$ mV/nm, 0 mV/nm and +4 mV/nm respectively. The spin-split bands of the conduction band are colored red and blue for clarity. (d) The ZFSS extracted from these band structures. For all electric fiels a minimum in spin-splitting is found, making this a robust feature of an inverted band structure.

REFERENCES

[1] R. Winkler, *Spin-Orbit Coupling Effects in Two-Dimensional Electron and Hole Systems* (Springer, Berlin, Heidelberg, 2003).

[2] J. Fabian, A. Matos-Abiague, C. Ertlera, P. Stano, and I. Žutić, *Semiconductor Spintronics,* Acta Phys. Slovaca **57**, 565 (2007).

[3] J. Nitta, T. Akazaki, H. Takayanagi, and T. Enoki, *Gate Control of Spin-Orbit Interaction in an Inverted* $\mathrm{In}_{0.53}\mathrm{Ga}_{0.47}$*As/*$\mathrm{In}_{0.52}\mathrm{Al}_{0.48}$*As Heterostructure,* Phys. Rev. Lett. **78**, 1335 (1997).

[4] D. Grundler, *Large Rashba Splitting in InAs Quantum Wells due to Electron Wave Function Penetration into the Barrier Layers,* Phys. Rev. Lett. **84**, 6074 (2000).

[5] B. Shojaei, P. J. J. O'Malley, J. Shabani, P. Roushan, B. D. Schultz, R. M. Lutchyn, C. Nayak, J. M. Martinis, and C. J. Palmstrøm, *Demonstration of gate control of spin*

splitting in a high-mobility InAs/AlSb two-dimensional electron gas, Phys. Rev. B **93**, 075302 (2016).

[6] I. Žutić, J. Fabian, and S. Das Sarma, *Spintronics: Fundamentals and applications,* Rev. Mod. Phys. **76**, 323 (2004).

[7] S. Datta and B. Das, *Electronic analog of the electro-optic modulator,* Appl. Phys. Lett. **56**, 665 (1990).

[8] J. Alicea, *New directions in the pursuit of Majorana fermions in solid state systems,* Rep. Prog. Phys. **75**, 076501 (2012).

[9] H. Kroemer, *The 6.1Å family (InAs, GaSb, AlSb) and its heterostructures: a selective review,* Physica E: Low-dimensional Systems and Nanostructures Proceedings of the 11th International Conference on Narrow Gap Semiconductors, **20**, 196 (2004).

[10] C. Liu, T. L. Hughes, X.-L. Qi, K. Wang, and S.-C. Zhang, *Quantum Spin Hall Effect in Inverted Type-II Semiconductors,* Phys. Rev. Lett. **100**, 236601 (2008).

[11] F. Qu, A. J. Beukman, S. Nadj-Perge, M. Wimmer, B.-M. Nguyen, W. Yi, J. Thorp, M. Sokolich, A. A. Kiselev, M. J. Manfra, C. M. Marcus, and L. P. Kouwenhoven, *Electric and Magnetic Tuning Between the Trivial and Topological Phases in InAs/GaSb Double Quantum Wells,* Phys. Rev. Lett. **115**, 036803 (2015).

[12] E. A. de Andrada e Silva, G. C. La Rocca, and F. Bassani, *Spin-split subbands and magneto-oscillations in III-V asymmetric heterostructures,* Phys. Rev. B **50**, 8523 (1994).

[13] L. J. Cooper, N. K. Patel, V. Drouot, E. H. Linfield, D. A. Ritchie, and M. Pepper, *Resistance resonance induced by electron-hole hybridization in a strongly coupled InAs/GaSb/AlSb heterostructure,* Phys. Rev. B **57**, 11915 (1998).

[14] A. Zakharova, S. T. Yen, and K. A. Chao, *Hybridization of electron, light-hole, and heavy-hole states in InAs/GaSb quantum wells,* Phys. Rev. B **64**, 235332 (2001).

[15] E. Halvorsen, Y. Galperin, and K. A. Chao, *Optical transitions in broken gap heterostructures,* Phys. Rev. B **61**, 16743 (2000).

[16] W. Xu, L. L. Li, H. M. Dong, G. Gumbs, and P. A. Folkes, *Band hybridization and spin-splitting in InAs/AlSb/GaSb type II and broken-gap quantum wells,* J. Appl. Phys. **108**, 053709 (2010).

[17] F. Nichele, M. Kjaergaard, H. J. Suominen, R. Skolasinski, M. Wimmer, B.-M. Nguyen, A. A. Kiselev, W. Yi, M. Sokolich, M. J. Manfra, F. Qu, A. J. Beukman, L. P. Kouwenhoven, and C. M. Marcus, *Giant Spin-Orbit Splitting in Inverted InAs/GaSb Double Quantum Wells,* Phys. Rev. Lett. **118**, 016801 (2017).

[18] J. Li, K. Chang, G. Q. Hai, and K. S. Chan, *Anomalous Rashba spin-orbit interaction in InAs/GaSb quantum wells,* Appl. Phys. Lett. **92**, 152107 (2008).

[19] B.-M. Nguyen, W. Yi, R. Noah, J. Thorp, and M. Sokolich, *High mobility back-gated InAs/GaSb double quantum well grown on GaSb substrate,* Appl. Phys. Lett. **106**, 032107 (2015).

[20] L. Onsager, *Interpretation of the de Haas-van Alphen effect,* Lond. Edinb. Dublin Philos. Mag. J. Sci. **43**, 1006 (1952).

[21] T. H. Sander, S. N. Holmes, J. J. Harris, D. K. Maude, and J. C. Portal, *Determination of the phase of magneto-intersubband scattering oscillations in heterojunctions and quantum wells,* Phys. Rev. B **58**, 13856 (1998).

[22] A. C. H. Rowe, J. Nehls, R. A. Stradling, and R. S. Ferguson, *Origin of beat patterns in the quantum magnetoresistance of gated InAs/GaSb and InAs/AlSb quantum wells,* Phys. Rev. B **63**, 201307 (2001).

[23] D. C. Tsui, T. Englert, A. Y. Cho, and A. C. Gossard, *Observation of Magnetophonon Resonances in a Two-Dimensional Electronic System,* Phys. Rev. Lett. **44**, 341 (1980).

[24] V. Gurevich and Y. A. Firsov, *On the theory of the electrical conductivity of semiconductors in a magnetic field,* Sov. Phys JETP **13** (1961).

[25] N. S. Averkiev, M. M. Glazov, and S. A. Tarasenko, *Suppression of spin beats in magneto-oscillation phenomena in two-dimensional electron gas,* Solid State Communications **133**, 543 (2005).

[26] D. M. Symons, M. Lakrimi, R. J. Nicholas, D. K. Maude, J. C. Portal, N. J. Mason, and P. J. Walker, *Magnetic breakdown in the semimetallic InAs/GaSb system,* Phys. Rev. B **58**, 7292 (1998).

[27] D. Shoenberg, *Magnetic Oscillations in Metals* (Cambridge, U.K., 1984).

[28] S. D. Ganichev, V. V. Bel'kov, L. E. Golub, E. L. Ivchenko, P. Schneider, S. Giglberger, J. Eroms, J. De Boeck, G. Borghs, W. Wegscheider, D. Weiss, and W. Prettl, *Experimental Separation of Rashba and Dresselhaus Spin Splittings in Semiconductor Quantum Wells,* Phys. Rev. Lett. **92**, 256601 (2004).

[29] X. Mu, G. Sullivan, and R.-R. Du, *Effective g-factors of carriers in inverted InAs/GaSb bilayers,* Appl. Phys. Lett. **108**, 012101 (2016).

[30] J. Luo, H. Munekata, F. F. Fang, and P. J. Stiles, *Effects of inversion asymmetry on electron energy band structures in GaSb/InAs/GaSb quantum wells,* Phys. Rev. B **41**, 7685 (1990).

[31] F. Herzog, T. Schäpers, D. Grundler, and M. A. Wilde, *Experimental determination of Rashba and Dresselhaus parameters and g*-factor anisotropy via Shubnikov-de Haas oscillations,* New J. Phys. **19**, 103012 (2017).

[32] Y. A. Bychkov and E. I. Rashba, *Oscillatory effects and the magnetic susceptibility of carriers in inversion layers,* J. Phys. C: Solid State Phys. **17**, 6039 (1984).

[33] Y. A. Bychkov and E. I. Rashba, *Properties of a 2D electron gas with lifted spectral degeneracy,* JETP Lett. **39**, 78 (1984).

[34] M. Studer, G. Salis, K. Ensslin, D. C. Driscoll, and A. C. Gossard, *Gate-Controlled Spin-Orbit Interaction in a Parabolic* GaAs/AlGaAs *Quantum Well,* Phys. Rev. Lett. **103**, 027201 (2009).

6

GIANT SPIN-ORBIT SPLITTING IN INVERTED InAs/GaSb DOUBLE QUANTUM WELLS

This chapter has been previously published as Fabrizio Nichele, Morten Kjaergaard, Henri J. Suominen, **Rafal Skolasinski**, Michael Wimmer, Binh-Minh Nguyen, Andrey A. Kiselev, Wei Yi, Marko Sokolich, Michael J. Manfra, Fanming Qu, Arjan J.A. Beukman, Leo P. Kouwenhoven, Charles M. Marcus, *Giant spin-orbit splitting in inverted InAs/GaSb double quantum wells*, Phys. Rev. Lett. **118**, 016801 (2017).

6.1. INTRODUCTION

The InAs/GaSb double quantum well (QW) shows a peculiar band alignment, with the InAs conduction band and the GaSb valence band residing very close in energy. Shifting the bands by tuning the QW thickness or applying perpendicular electric field yields a rich electronic phase diagram [1–4]. When the InAs conduction band resides higher than the GaSb valence band, the band structure of a trivial insulator is obtained. By lowering the InAs conduction band below the GaSb valence band, a small hybridization gap opens at finite k-vectors [1]. Beyond topological-insulator behavior, expected to emerge in the hybridization gap [2, 5–9], the impact of the inverted band structure on transport remains largely unexplored.

Here, we investigate experimentally and numerically how the combination of spin-orbit coupling (SOC) and electron-hole mixing results in a giant band splitting in InAs/GaSb heterostructures close to the hybridization gap. The two resulting subbands, with opposite spin-orbit eigenvalue and different carrier densities, contribute to transport in parallel, and can be detected via magnetotransport measurements. These results are of potential value to semiconductor spintronics, where two-dimensional electron gases (2DEGs) with sizable spin-orbit splittings at low density are desirable [10].

To quantify SOC directly from experimental data, without relying on any particular model, we use the spin-orbit polarization $(n_1 - n_2)/(n_1 + n_2)$, with $n_{1,2}$ the carrier densities of the split spin-orbit subbands[1]. In Rashba systems, the larger the SOC parameter α, the larger the density difference of the subbands at the Fermi energy, with α typically increasing with density [11]. However, the spin-orbit polarization is usually smaller than 15%, even for 2DEGs with large SOC such as InAs, InSb or HgTe [12–17], while values up to 40% are reached in GaAs or HgTe hole gases [18–21]. In contrast, we find that the hybridized band structure of InAs/GaSb results in two striking peculiarities. First, the spin-orbit polarization increases approaching the charge neutrality point (CNP); second, the spin-orbit polarization reaches 100%.

6.2. EXPERIMENTAL DETAILS

Experiments were performed on a 12.5 nm InAs, 5 nm GaSb structure patterned in a $100 \times 50\ \mu\text{m}^2$ Hall bar geometry oriented along the [110] crystallographic direction and covered with a global top gate. Magnetotransport measurements used conventional low-frequency lock-in techniques at a temperature of 50 mK. Additional information on the wafer structure, sample fabrication and measurement techniques are provided in Chapter 6.7.1.

6.3. THEORY DISCUSSION ON THE BAND STRUCTURE

To realistically model our device, we first determine the band alignment as a function of top gate voltage, V_{TG}, using a parallel plate capacitor model [3] discussed in Chapter 6.7.2. The model predicts the density dependence for electrons (n) and holes (p) shown in Fig. 6.1(a). For $V_{\text{TG}} > -0.2$ V only electrons are present in the system, with the kink in n at $V_{\text{TG}} = -0.2$ V coinciding with the onset of hole accumulation. Once the hole layer

---

[1] We use the same subband definition as in Sec. 6.3.1 of Ref. [11].

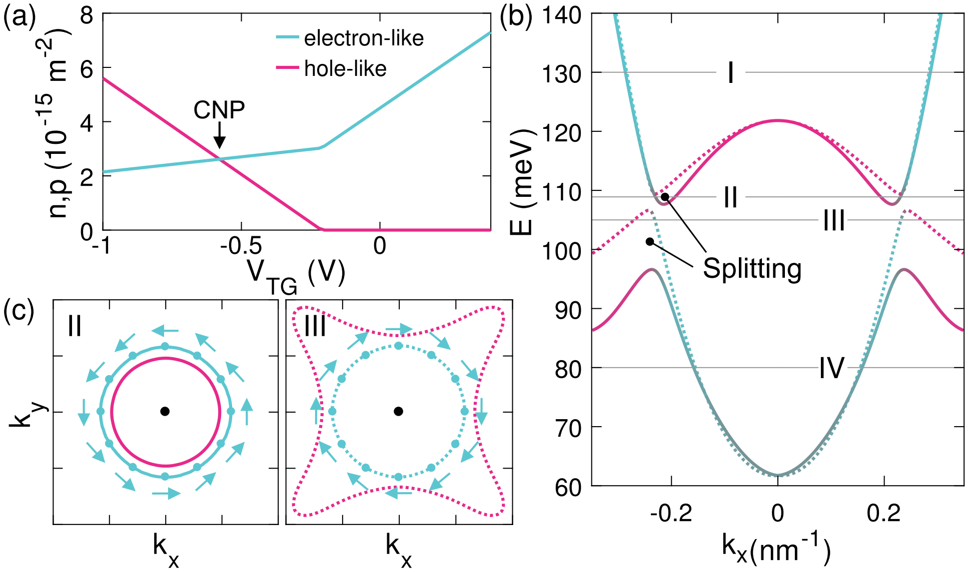

Figure 6.1: (a) Expected electron and hole densities dependence on V_{TG}. (b) Numerical band structure calculation for $V_{\text{TG}} = -0.4$ V. The color indicates the wavefunction main character, solid and dotted lines distinguish two spin-orbit split subbands. (c) Fermi contours and spin-texture of electron-like states for the Fermi energies II and III indicated in (b). The axis divisions are 0.2 nm^{-1}, with the black dot indicating the origin. Fermi pockets at large k-vector are ignored, but further discussed in Chapter 6.7.4.

is populated, it partially screens the electrons from being further depleted via the top gate. The hybridization gap is expected at CNP, when $n = p$. The calculated electrostatic potential is then used for a V_{TG} dependent band structure simulation using standard $\boldsymbol{k} \cdot \boldsymbol{p}$ theory, Chapter 6.7.3. In particular, we are interested in the band structure of our system close to CNP.

The band structure for $V_{\text{TG}} = -0.4$ V is presented in Fig. 6.1(b). The band coloring represents the calculated wavefunction character (blue for electron-like and pink for hole-like states, also recognizable from the band curvature) while solid and dotted lines distinguish the spin-orbit species. In this configuration electron and hole bands are inverted and hybridized, with a small gap at finite k-vectors. Results for different gate voltages, shown on Fig. 6.6 in Chapter 6.7.4, are qualitatively similar but with a varying band overlap. Remarkably, SOC vertically splits the hybridized bands by a sizable amount resulting in a spin dependent hybridization gap. In this unique band structure, the Fermi energy can cross a *single* branch of the spin split bands, as indicated by the energy levels II and III in Fig. 6.1(b). In these situations the system contains both electron- and hole-like carriers, and the carriers of the same kind are *fully spin-orbit polarized*. This effect is prominent close to the band crossing and negligible far from the hybridization gap [see I and IV in Fig. 6.1(b)], as expected for individual InAs and GaSb QWs. While the gap size and the bands overlap depend on V_{TG}, the giant splitting at the CNP is a generic feature of the model. Qualitatively similar results were also obtained in previous calculations [2, 22–24]. The simulation is consistent with our experiments, where we measure no clear gapped region at the CNP, but a giant spin-orbit splitting of electron- and hole-like states.

Fermi contours for energy levels II and III are shown in Fig. 6.1(c), together with the calculated spin texture of electron-like states. The model indicates Rashba-like spin orientation with spins nearly perpendicular to the momentum direction, with small deviations due to the absence of axial symmetry. This situation is reminiscent of Dirac materials such as graphene or three-dimensional topological insulators, and signatures of Berry phase effects can be expected. Hole-like states are instead highly anisotropic.

6.4. MAGNETOTRANSPORT MEASUREMENTS

6.4.1. LOW FIELD R_{xx} AND R_{xy} DATA

Magnetotransport measurements, shown in Fig. 6.2, confirm the sample has an inverted band structure, and is tunable from a pure electron regime to a mixed electron-hole regime. Typical for high mobility structures [3, 25], the longitudinal resistivity ρ_{xx} exhibits a series of peaks and dips as a function of V_{TG}, as shown in Fig. 6.2(a). The resistance peaks at $V_{\mathrm{TG}} = -0.60$ V and $V_{\mathrm{TG}} = -0.35$ V are interpreted with the Fermi energy crossing the CNP and the valence band top respectively [3], as discussed in reference to Fig. 6.3(c). In Ref. [25] a resistance dip in the hole-dominated region, similar to what we observe at $V_{\mathrm{TG}} = -0.75$ V, was identified as a van Hove singularity at the bottom of the hybridization gap.

Figure 6.2(b) shows the transverse resistivity ρ_{xy} as a function of perpendicular field $B_\perp$ for different values of V_{TG}. For $V_{\mathrm{TG}} > -0.4$ V, ρ_{xy} has a positive slope, indicative of exclusively electron-like transport. For $V_{\mathrm{TG}} \leq -0.75$ V, the ρ_{xy} slope reverses at finite $B_\perp$, a hallmark of the simultaneous presence of electrons and holes in the system. This behavior persists down to $V_{\mathrm{TG}} = -1.2$ V, indicating a pure hole state is not reached in the gate range of operation, consistent with the calculation of Fig. 6.1(a).

6.4.2. HIGH FIELD R_{xx} DATA

The ambipolar behavior discussed above in terms of ρ_{xy} also becomes apparent in ρ_{xx} in large perpendicular magnetic fields, where Shubnikov-de Haas (SdH) oscillations and quantum Hall states develop in the entire gate range [Fig. 6.2(c)]. For $V_{\mathrm{TG}} \geq -0.2$ V we observe regular electron-like Landau levels (LLs) with Zeeman splitting at high field, as indicated by the numbering in Fig. 6.2(c), obtained from ρ_{xy}. The large resistance increase as a function of $B_\perp$ for $V_{\mathrm{TG}} \approx -0.6$ V is consistent with an identical number of electron and hole LLs at the CNP [26, 27].

For $V_{\mathrm{TG}} \leq -0.5$ V electron-like and hole-like LLs coexist, as also evident from the non-monotonic ρ_{xy} [see Fig. 6.2(b)]. In this regime, signatures of electron-hole hybridization are visible as avoided-crossings between LLs, as previously observed via cyclotron resonances [28, 29]. Based on the analysis presented in Fig. 6.3(c), we assign to the hole-like LLs the filling factors indicated with negative numbering. Approaching the CNP from the electron regime, a peculiar closing and reopening of spin-split levels takes place, as marked with primed numbers. This is associated with the spin-orbit splitting becoming larger than the LL separation. An additional evolution of the LLs takes places for $V_{TG} \approx -0.4$ V as indicated with double-primed numbering. As discussed in the following, this is associated with the depopulation of one split subband. Filling factors assigned to

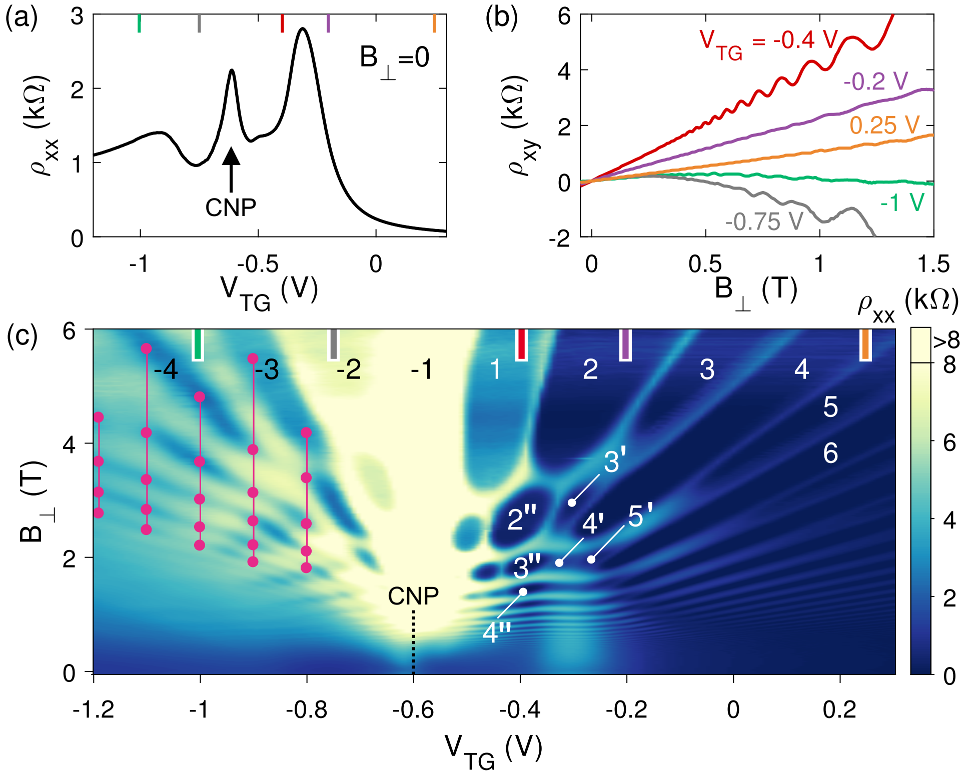

Figure 6.2: (a) Longitudinal resistivity ρ_{xx} as a function of top gate voltage for $B_\perp = 0$, with the position of the charge neutrality point indicated. (b) Transverse resistivity ρ_{xy} as a function of $B_\perp$ for different values of V_{TG}, as also indicated by the markers in (a) and (c). (c) ρ_{xx} as a function of V_{TG} and $B_\perp$, with positive (negative) numbering indicating electron-like (hole-like) LLs. Pink dots denotes h-like filling factors and are used to extract the hole density shown in Fig. 6.3(c).

primed and double primed LLs are confirmed by ρ_{xy} measurements.

6.5. ANALYSIS

6.5.1. ELECTRON REGIME

We now address the electron-like states close to the hybridization gap. Low-field SdH oscillations are a powerful tool to study properties at the Fermi surface such as electron density and effective mass [30, 31]. In systems where two subbands contribute to transport in parallel, as 2DEGs with strong SOC, the SdH oscillations manifest a beating pattern given by the superposition of two sets of oscillations with different $1/B_\perp$ periodicity [12–17, 32]. The power spectrum of ρ_{xx} $(1/B_\perp)$ then allows one to extract the density components n_i from the peak frequencies f_i as $n_i = ef_i/h$ [11]. The SdH analysis gives the densities of the individual subbands and the Hall slope gives the net free charge of the system n_{Hall}. For two spin-split electron-like subbands we expect $n_{\mathrm{Hall}} = n_1 + n_2$.

Figure 6.3(a) shows a zoom-in of Fig. 6.2(c) for the electron regime with the vertical

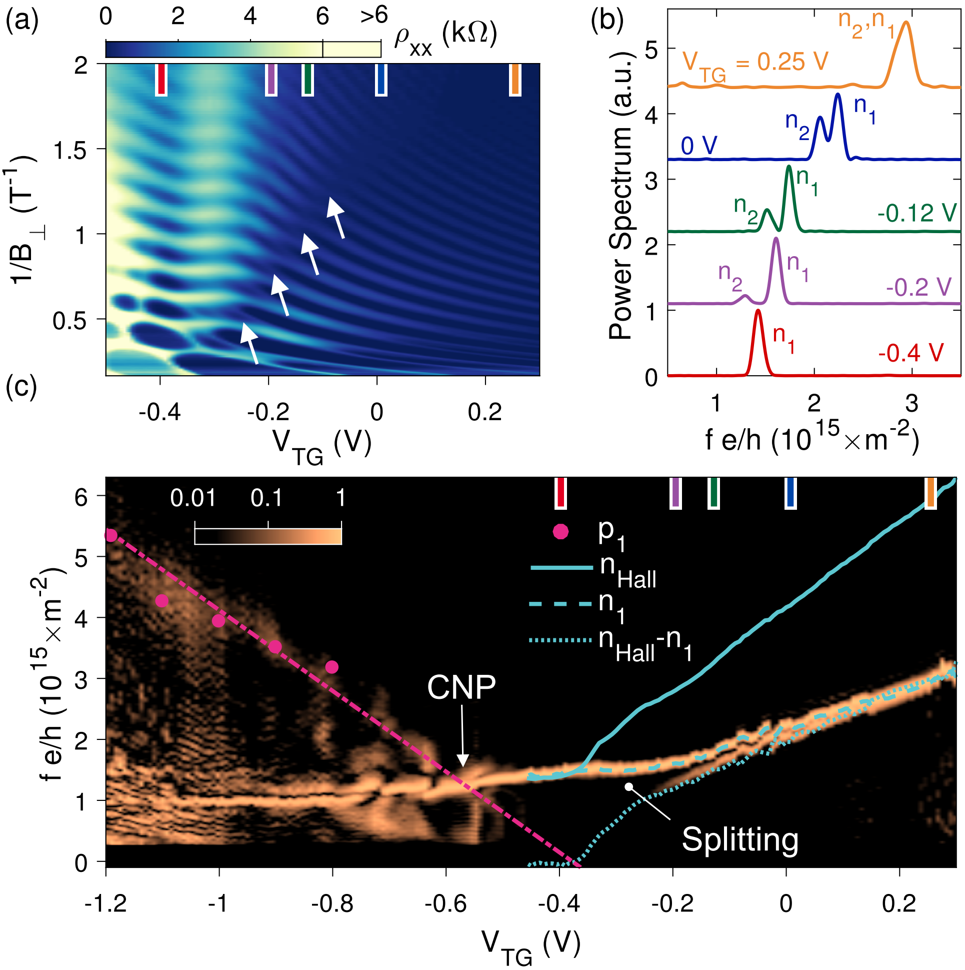

Figure 6.3: (a) Longitudinal resistivity ρ_{xx} as in Fig. 6.2(c) for $V_{TG} \geq -0.5$ V as a function of $1/B_\perp$. The arrows indicate a beating in the SdH oscillations, visible as a π phase shift. (b) Normalized power spectrum of $\rho_{xx}(1/B_\perp)$ for various gate voltages (data offset for clarity). The frequency axis has been multiplied by e/h to directly show the subband densities. (c) Color map of the power spectrum as in (b) as a function of V_{TG}. The amplitude of the power spectrum has been normalized, column by column, to the n_1 peak. The solid blue line indicates the density obtained from the Hall slope, the dashed line marks the n_1 peak and the dotted line gives the difference between the two. Dots indicate the hole density obtained from hole-like LLs in Fig. 6.2(c) with the dashed-dotted line being a guide to the eye.

axis scaled as $1/B_\perp$ to make the SdH oscillations periodic. A beating, visible as a π phase slip, is indicated with arrows. Figure 6.3(b) shows the power spectrum of the data in Fig. 6.3(a) for five gate voltage values. The frequency axis f has been multiplied by e/h to directly show the subband densities. At positive V_{TG}, the power spectrum reveals a single oscillation frequency. Decreasing V_{TG}, the peak moves to lower electron densities and gradually splits into two components. The amplitude of the low-density peak decreases with respect to its high density counterpart (n_1) until it disappears in the background for $V_{\mathrm{TG}} < -0.25$ V. The quench of the n_2 peak at finite density is compatible with a $k \neq 0$ minimum in the dispersion relation of the high energy split band, as just above energy II in Fig. 6.1(a).

Additional insight into the data is gained by comparing the peak positions with the Hall density. The same analysis as in Fig. 6.3(b) is shown in the color plot of Fig. 6.3(c) as a function of V_{TG}. The solid blue line indicates the density n_{Hall}, extracted from ρ_{xy}. The dashed line tracks the position of the n_1 peak in the power spectrum while the dotted line shows the quantity $n_{\mathrm{Hall}} - n_1$. For $V_{\mathrm{TG}} > 0$ a single peak is visible in the spectrum with $fe/h = n_{\mathrm{Hall}}/2$. This is consistent with two spin degenerate bands with $n_1 = n_2$, as in scenario I in Fig. 6.1(a). Once the splitting develops, as highlighted in Fig. 6.3(c), $n_{\mathrm{Hall}} - n_1$ matches the position of the measured n_2 peak. The analysis is extended down to $V_{\mathrm{TG}} = -0.46$ V, where ρ_{xy} does not show indication of hole transport yet. The density difference between the two subbands gradually increases until $n_{\mathrm{Hall}} = n_1$ at $V_{\mathrm{TG}} \approx -0.4$ V, i.e. all mobile charge resides in a *single* band with $n_1 = 1.4 \times 10^{15}\ \mathrm{m}^{-2}$. This is compatible with situation II in Fig. 6.1(a).

6.5.2. ELECTRON-HOLE REGIME

Below the CNP, the electron-like n_1 peak coexists with a hole-like state, highlighted with a dotted-dashed line in Fig. 6.3(c). We confirmed that its position matches the periodicity of the hole-like LLs [cf. dots in Figs. 6.2(c) and Figs. 6.3(c)]. The hole signature in the spectrum can either be interpreted as two degenerate subbands $p_1 = p_2$, or one spin-orbit polarized subband p_1. Extracting the total density from the Hall slope is less accurate in this regime due to the non-linearity of $\rho_{xy}(B)$, preventing further analysis. Nevertheless, assuming a single subband p_1, as predicted by our model for situation III in Fig. 6.1(b), the top gate capacitance in the hole regime ($-\partial p_1/\partial V_{\mathrm{TG}}$) matches that in the electron regime ($\partial n_{\mathrm{Hall}}/\partial V_{\mathrm{TG}}$), as expected from the electrostatic model of Fig. 6.1(a). Furthermore, the absence of Zeeman splitting in the hole-like LL up to high field supports the interpretation that holes are also fully spin-orbit polarized. Assuming a single hole-like band, the filling factors indicated in Fig. 6.3(c) with negative numbering are calculated for the hole-like LLs, consistent with identical filling factor for electron- and hole-like LL (1 and −1 respectively) being populated at the CNP [26, 27]. From these observation we conclude that a *single* and *fully spin-orbit polarized* hole band p_1 is occupied below the CNP, consistent with scenario III in Fig. 6.1(b).

The intersection between p_1 and n_1 at $V_{\mathrm{TG}} \approx -0.6$ V determines the CNP, consistent with Fig. 6.2(b). The crossing of the Fermi energy with the top of the valence band is inferred to be at $V_{\mathrm{TG}} = -0.35$ V. This matches the peak in ρ_{xx}, as seen in Fig. 6.2(a), and the kink in n_{Hall} visible in Fig. 6.3(c) marking a change in gate capacitance as a screening layer is populated.

6.5.3. NON-DEGENERATE 2DEG

After demonstrating the large splitting at the CNP, we investigate how the large spin-orbit polarization affects transport phenomena. The zero field polarization of electron-like states, quantified as $(n_1 - n_2)/(n_1 + n_2)$, saturates at 100% for $V_{\mathrm{TG}} = -0.4$ V [Fig. 6.4(a)]. Despite expecting hole-like states in this regime, hole conduction is not experimentally

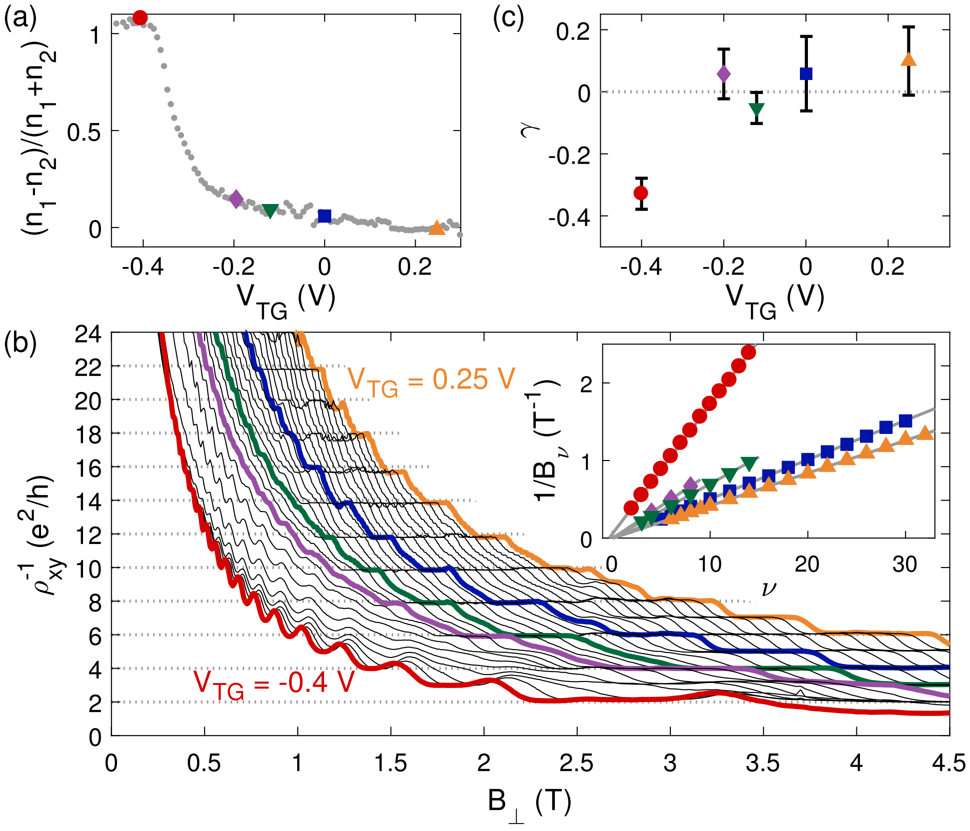

Figure 6.4: (a) Spin-orbit polarization of electron-like states as a function of V_{TG}, with markers defined as in (b). (b) Inverse transverse resistivity, ρ_{xy}^{-1}, for different top gate voltages, V_{TG}. Inset: Inverse magnetic field positions of the filling factors ν for different V_{TG} values. Solid lines are linear fits to the data. (c) Phase offset γ of the data in the inset of (b) extrapolated for $1/B \to 0$.

detected, either by a slope reversal in ρ_{xy} [Fig. 6.2(b)] or additional LLs in ρ_{xx} [Fig. 6.2(c)]. This behavior is presumably due to the low mobility of holes in GaSb which, for densities lower than $5 \times 10^{14}\ \mathrm{m}^{-2}$ may localize. As only electron-like states contribute to transport, this situation effectively realizes a helical 2DEG. Such a system is reminiscent of the surface of three-dimensional topological insulators, where the Fermi energy crosses a single spin resolved band, and might have potential interest for studying topological states of matter.

The full spin-orbit polarization for $V_{\mathrm{TG}} \approx -0.4$ V is further confirmed by the quantum Hall plateaus of ρ_{xy}^{-1}, shown in Fig. 6.4(b). At high electron density (orange line, $V_{\mathrm{TG}} = 0.25$ V) the plateaus evolve in steps of $2e^2/h$, as expected for a conventional 2DEG. For $B_\perp > 3$ T, Zeeman splitting lifts spin degeneracy resulting in e^2/h plateaus. In the fully polarized regime (red line, $V_{\mathrm{TG}} = -0.4$ V) the plateaus exquisitely evolve as integer multiples of e^2/h from the first visible steps at $B_\perp \approx 400$ mT. This is further evidence of the helical nature of electron-like states, extending also to small magnetic fields. The oscillations in the low density plateaus [also visible in Fig. 6.2(b)] are attributed to disorder, resulting in a broadening of LLs and an eventual mixing between ρ_{xx} and ρ_{xy} [33]. We note that the overshoots in ρ_{xy}^{-1} or an eventual presence of hole-like states do not compromise the analysis. In fact the density of the system for $V_{\mathrm{TG}} = -0.4$ V is confirmed within 5% by three independent checks: (i) The slope of ρ_{xy}, constant up to $B_\perp = 5$ T, (ii) The periodicity of the low-field SdH oscillations, (iii) The magnetic field position B_ν of the $\nu e^2/h$ plateaus in ρ_{xy}^{-1}, satisfying $n_1 = \nu e B_\nu / h$.

6.5.4. BERRY PHASE

The unique Fermi level crossing present in our system, together with strong SOC, can result in a non-trivial Berry phase acquired by electrons on a closed cyclotron orbit, such as in Fig. 6.1(c). To check this eventuality, we measured the phase offset φ of the SdH oscillations for $1/B \to 0$, similar to earlier work on graphene [34, 35] and 3D topological insulators [36, 37]. While conventional 2DEGs have $\varphi = 0$, materials with a symmetric Dirac cone exhibit $\varphi = 1/2$. In a complex band structure as in the present case, the Berry phase is not expected to be quantized but to vary depending on the details of the dispersion relation [38]. The inset of Figure 6.4(b) shows the $1/B_\nu$ positions of the ν filling factors for various top gate voltages (markers) together with linear fits (lines) extrapolating to $1/B \to 0$. The result of the extrapolation is shown in Fig. 6.4(c). For $V_{\mathrm{TG}} \geq -0.2$ V, all the curves consistently give $\varphi \approx 0$, as expected for normal fermions. For $V_{\mathrm{TG}} = -0.4$ V the extrapolation leads a phase shift $\varphi = -0.33 \pm 0.05$, consistent with a non-zero Berry phase.

6.6. CONCLUSIONS

In conclusion, we studied the band structure of inverted InAs/GaSb QWs via magneto-transport measurements. Consistent with simulations, electron-like and hole-like states are fully spin-orbit polarized in proximity of the CNP. We identify a regime where a single electron-like band with helical spin texture contributes to transport. The 100% spin-orbit polarization of the system is confirmed by quantum Hall plateaus evolving in e^2/h steps and a non-trivial Berry phase.

6.7. SUPPLEMENTARY INFORMATION

6.7.1. MATERIAL AND METHODS

The wafer structure was grown by molecular beam epitaxy on a [001] oriented GaSb substrate. From top to bottom it consists of a 3 nm GaSb capping layer, a 50 nm AlSb insulating barrier, a 5 nm GaSb QW grown on top of a 12.5 nm InAs QW, a second AlSb barrier and a thick GaSb buffer layer. More information on wafer growth are reported in Ref. [3, 4, 39].

A $100 \times 50\ \mu\mathrm{m}^2$ Hall bar structure was patterned with conventional electron beam lithography techniques and wet etching. The Hall bar structure was oriented along the [110] crystallographic direction. For wet etching we used a general III-V etching solution consisting of $H_2O : C_6H_8O_7 : H_3PO_4 : H_2O_2$ in concentration 220 : 55 : 3 : 3. The solution was kept at room temperature and well stirred, resulting in an etching rate of approximately 1 nm s^{-1}. Ohmic contacts were defined by etching the wafer down to the InAs quantum well and depositing Ti/Au electrodes, without any annealing. The sample was covered with a 40 nm HfO_2 insulating layer grown by atomic layer deposition and a global Ti/Au top gate.

Transport measurements were performed in a dilution refrigerator with a base temperature of 50 mK using low frequency (< 100 Hz) lock-in techniques. The amplitude of the AC currents was always kept small enough (≤ 20 nA) to prevent sample heating. Due to the onset of leakage currents at finite bias, the device was operated at zero back gate voltage, where the resistance between the 2DEG and the back gate was in excess of 10 GΩ.

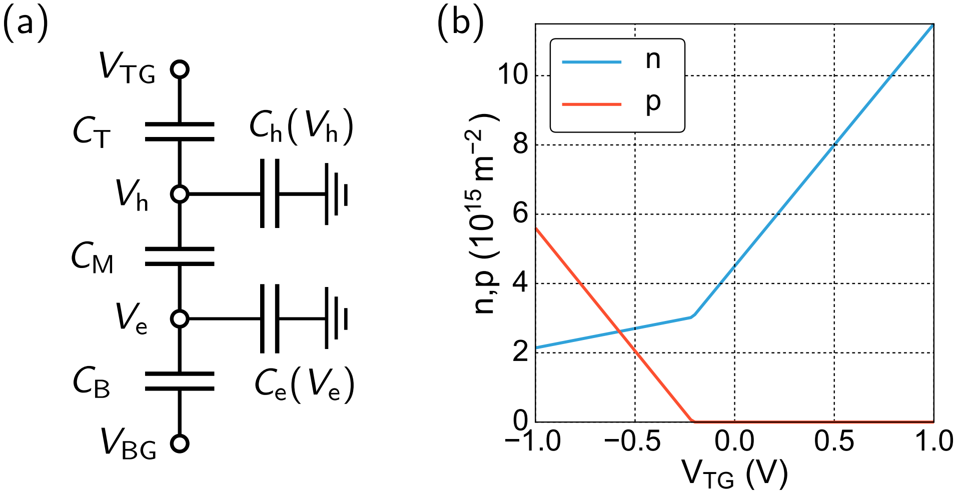

Figure 6.5: (a) Schematic of the capacitor model for InAs/GaSb quantum wells. (b) Electron (n) and hole (p) densities obtained from the capacitor model as a function of the top-gate voltage V_{TG}

6.7.2. CAPACITOR MODEL

To estimate the electric fields in the quantum well we use the capacitor model introduced in Ref. [3] (see Fig. 6.5(a). With the material parameters from Ref. [3] and assuming the dielectric constant of HfO_2 as $\epsilon_{HfO_2} = 25$ we find the geometric capacitances for our quantum well structure as $C_T = 135\,\mathrm{nF/cm^2}$, $C_M = 1.6\,\mu\mathrm{F/cm^2}$, and $C_B = 177\,\mathrm{nF/cm^2}$. The quantities C_e and C_h are quantum capacitances [40] that are non-zero only if there is a finite carrier density. The capacitor model neglects the intrinsic inversion of electron and hole bands in the InAs/GaSb quantum well, but assumes that the Fermi energy is aligned with the electron and hole band bottom when the potential in the respective layer is 0V. Hence, $C_e = 2.7\,\mu\mathrm{F/cm^2}$ if $V_e > 0$ and zero else, whereas $C_e = 6\,\mu\mathrm{F/cm^2}$ if $V_h < 0$ and zero else. V_e and V_h are the potential values in the middle of the InAs and GaSb layers.

In our experiments, the back gate is always kept at $V_{BG} = 0$V. The assumptions of the capacitor model then imply that for $V_{TG} = 0$V both electron and hole density are zero. In the experiment, we however find a nonzero electron density in this case, due to in-built electric fields. We approximate these electric fields by a finite fictitious back gate voltage V_{BG} that we fix such that we recover the experimentally measured electron density of $n \approx 4.5 \times 10^{15} m^{-2}$ for $V_{TG} = 0$V (see Fig. 3 in the main text).

Even with its simplifications, the capacitor model captures essential features of the experiment: Fig. 6.5(b) shows electron and hole densities as a function of top gate voltage. Equal densities of electrons and holes are found around $V_{\mathrm{TG}} = -0.6\,\mathrm{V}$ which agrees with the voltage where the charge neutrality point is found experimentally. Additionally, we observe that the gate-tunability of the electron density is strongly reduced when holes are occupied. The finite density of charge carriers in the GaSb (hole) layer lieing between top gate and (electron) InAs layer screens the electric field. A similar feature is seen in Fig. 3 of the main text. The screening by the hole layer also explains why experimentally the second electron Fermi surface is never recovered within our gate voltage range.

We note that the capacitor model assumes constant density of states of the electron and hole layer, and no electron-hole mixing. For this reason, the quantitative results of Fig. 6.5 are valid in the high density limit, but should be taken with care close to the CNP, where the density of states shows gaps and singularities.

6.7.3. k·p SIMULATIONS

The numerical band structure simulations use the standard semiconductor $\boldsymbol{k}\cdot\boldsymbol{p}$ model [41, 42], that we discussed in Section 2.3.

For our simulations, we take the band structure parameters from [43, 44] (summarized in Table 6.1). The valence band offsets [43] are 0.56 eV for GaSb-InAs, 0.18 eV for AlSb-InAs and −0.38 eV for AlSb-GaSb.

Table 6.1: Band structure parameters for InAs, GaSb and AlSb at $T = 0$ K. (Ref. [43, 44])

	E_g [eV]	Δ [eV]	E_P [eV]	m_c/m_0	γ_1	γ_2	γ_3	κ
InAs	0.41	0.38	22.2	0.024	19.67	8.37	9.29	7.68
GaSb	0.8128	0.752	22.4	0.042	11.8	4.03	5.26	3.18
AlSb	2.32	0.75	18.7	0.18	4.15	1.01	1.75	0.31

6.7.4. GATE DEPENDENCE OF THE BAND STRUCTURE

Computing the gate dependence of the band structure of InAs/GaSb quantum wells quantitatively requires a self-consistent solution of the 8×8 Kane Hamiltonian and the Poisson equation. This problem involves both electron and hole densities, and while some approximate approaches have been discussed [45], it has not yet been solved satisfactorily. For this reason we choose to only take into account the electrostatics due to gating on the level of the capacitor model. We extract a electrostatic potential $V(z)$, approximating the voltage drop between the nodes of the capacitor model as linear (this is justified as the dielectric constants of the different materials differ by at most a factor of 2). This potential enters the Kane Hamiltonian (2.64) as an additional term on the diagonal. Finally, the spin texture shown in Fig. 1(c) of the main text are calculated as the expectation value of the electron spin Pauli matrices $\sigma_{x,y}$ at a constant energy.

The use of the capacitor model is justified in that we only strive to capture the qualitative aspects of the band structure. Further, as we see below, the spin-orbit features depend little on gating, as they are dominated by the intrinsic inversion symmetry breaking in the quantum well structure.

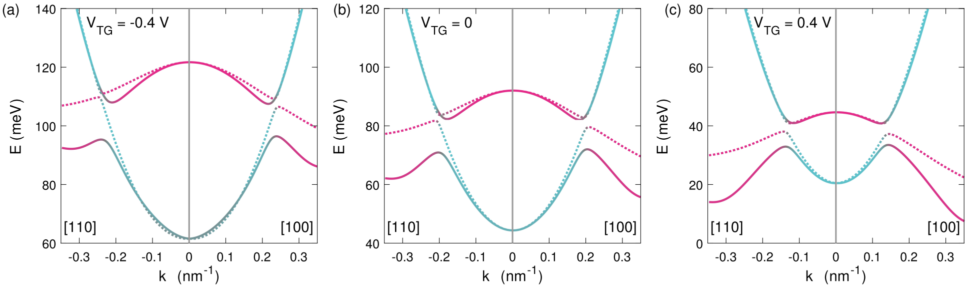

Figure 6.6: Numerical band structure calculation of InAs/GaSb for two crystallographic directions at different top gate voltages. The band coloring represents the wavefunction character (blue for electron-like sates, red for hole-like states) while solid and dotted lines distinguish the two spin-orbit split bands. (a) $V_{TG} = -0.4$ V, strong band splitting for the two lower bands and significant splitting in the two upper bands. (b) $V_{TG} = 0$ (only built in electric field). Still strong spin-orbit splitting in the lower bands, still visible split in the upper bands. (c) $V_{TG} = 0.4$ V, significant split in the two lower bands, vanishing split in the upper bands.

We present result of the band structure calculation for different top gate voltage in Fig. 6.6. We show results for the [110] crystallographic direction on the left hand side of each plot, and results for the [100] direction of the right hand side. The colors of the band indicate the wavefunction character (blue for electron-like and red for hole-like states) while solid and dashed lines distinguish the two spin-orbit split bands. We describe the proceude used to calculate the colors in Sec. 6.7.5. The biggest effect of the gate voltage is an change of the $k = 0$ gap between the hole and the electron bands due to the electric field. As a consequence, the hybridization gap occurs at larger momenta for more negative top-gate voltages. At the same time, the hybridization gap becomes smaller and eventually vanishes. This is consistent with the experiment that finds still a significant residual conductance at the charge neutrality point.

The spin splitting in the band above the hybridization gap is gate-voltage dependent (from well visible at $V_{TG} = -0.4$ V) to nearly vanishing at $V_{TG} = 0.4$ V)). On the other hand, the large spin-orbit splitting in the bands below the hybridization gap is largely independent of gate voltage. Therefore at every gate voltage we can choose a Fermi level that corresponds to a system characterized by a single electron spin species. The hybridization gap also changes with gate voltage. For example a large positive gap is obtained for $V_{TG} = 0.4$ V). In that situation, and with the Fermi energy placed in the gap with the help of a back gate voltage, the system would reach the topological insulator regime. As the top gate voltage is made more negative, the bands overlap increases and the hybridization gap reduces. In particular, already at $V_{TG} = -0.4$ V close inspection reveals the gap is anisotropic and vanishes along the [110] direction. As a result, at the energy level II of Fig. 1(b) of the main text, four Fermi pockets centered along the [110] direction could be present. In the present work we believe disorder potential could largely smear these features, if actually present in our samples. Furthermore their large effective mass would make negligible their contribution in transport. For this reason their presence is ignored in the left hand side of Fig. 1(c) of the main text.

6.7.5. ESTIMATION OF ELECTRON-HOLE MIXING IN MOMENTUM STATES

The wave functions of momentum states that we present in Fig. 1(b) of the main text and in Fig. 6.6 contain both electron and hole components. Assuming the order of different wave function components is in agreement with the Hamiltonian of Eq. 2.64, we define

$$|\psi_e|^2 = \sum_{n=1}^{n=2} \int |\psi_n(x)|^2 \, dx; \tag{6.1}$$

$$|\psi_h|^2 = \sum_{n=3}^{n=8} \int |\psi_n(x)|^2 \, dx, \tag{6.2}$$

where

$$|\psi_e|^2 + |\psi_h|^2 = 1. \tag{6.3}$$

The blue color on the band structure plots corresponds to pure electron state ,$|\psi_e|^2 = 1$, and the pink color corresponds to pure hole state, $|\psi_h|^2 = 1$. The smooth color variation from blue to red indicates the mixing of electron and holes states along the energy bands.

REFERENCES

[1] M. J. Yang, C. H. Yang, B. R. Bennett, and B. V. Shanabrook, *Evidence of a Hybridization Gap in "Semimetallic" InAs/GaSb Systems,* Phys. Rev. Lett. **78**, 4613 (1997).

[2] C. Liu, T. L. Hughes, X.-L. Qi, K. Wang, and S.-C. Zhang, *Quantum Spin Hall Effect in Inverted Type-II Semiconductors,* Phys. Rev. Lett. **100**, 236601 (2008).

[3] F. Qu, A. J. Beukman, S. Nadj-Perge, M. Wimmer, B.-M. Nguyen, W. Yi, J. Thorp, M. Sokolich, A. A. Kiselev, M. J. Manfra, C. M. Marcus, and L. P. Kouwenhoven, *Electric and Magnetic Tuning Between the Trivial and Topological Phases in InAs/GaSb Double Quantum Wells,* Phys. Rev. Lett. **115**, 036803 (2015).

[4] F. Nichele, H. J. Suominen, M. Kjaergaard, C. M. Marcus, E. Sajadi, J. A. Folk, F. Qu, A. J. A. Beukman, F. K. d. Vries, J. v. Veen, S. Nadj-Perge, L. P. Kouwenhoven, B.-M. Nguyen, A. A. Kiselev, W. Yi, M. Sokolich, M. J. Manfra, E. M. Spanton, and K. A. Moler, *Edge transport in the trivial phase of InAs/GaSb,* New J. Phys. **18**, 083005 (2016).

[5] I. Knez, R.-R. Du, and G. Sullivan, *Evidence for Helical Edge Modes in Inverted* InAs/GaSb *Quantum Wells,* Phys. Rev. Lett. **107**, 136603 (2011).

[6] K. Suzuki, Y. Harada, K. Onomitsu, and K. Muraki, *Edge channel transport in the InAs/GaSb topological insulating phase,* Phys. Rev. B **87**, 235311 (2013).

[7] I. Knez, C. T. Rettner, S.-H. Yang, S. S. Parkin, L. Du, R.-R. Du, and G. Sullivan, *Observation of Edge Transport in the Disordered Regime of Topologically Insulating* InAs/GaSb *Quantum Wells,* Phys. Rev. Lett. **112**, 026602 (2014).

[8] L. Du, I. Knez, G. Sullivan, and R.-R. Du, *Robust Helical Edge Transport in Gated* InAs/GaSb *Bilayers,* Phys. Rev. Lett. **114**, 096802 (2015).

[9] S. Mueller, A. N. Pal, M. Karalic, T. Tschirky, C. Charpentier, W. Wegscheider, K. Ensslin, and T. Ihn, *Nonlocal transport via edge states in InAs/GaSb coupled quantum wells,* Phys. Rev. B **92**, 081303 (2015).

[10] I. Žutić, J. Fabian, and S. Das Sarma, *Spintronics: Fundamentals and applications,* Rev. Mod. Phys. **76**, 323 (2004).

[11] R. Winkler, *Spin-Orbit Coupling Effects in Two-Dimensional Electron and Hole Systems* (Springer, Berlin, Heidelberg, 2003).

[12] J. Luo, H. Munekata, F. F. Fang, and P. J. Stiles, *Observation of the zero-field spin splitting of the ground electron subband in gasb-inas-gasb quantum wells,* Phys. Rev. B **38**, 10142 (1988).

[13] B. Das, D. C. Miller, S. Datta, R. Reifenberger, W. P. Hong, P. K. Bhattacharya, J. Singh, and M. Jaffe, *Evidence for spin splitting in* $\mathrm{In}_x\mathrm{Ga}_{1-x}\mathrm{As}/\mathrm{In}_{0.52}\mathrm{Al}_{0.48}\mathrm{As}$ *heterostructures as* $B \rightarrow 0$*,* Phys. Rev. B **39**, 1411 (1989).

[14] J. P. Heida, B. J. van Wees, J. J. Kuipers, T. M. Klapwijk, and G. Borghs, *Spin-orbit interaction in a two-dimensional electron gas in a InAs/AlSb quantum well with gate-controlled electron density,* Phys. Rev. B **57**, 11911 (1998).

[15] S. Brosig, K. Ensslin, R. J. Warburton, C. Nguyen, B. Brar, M. Thomas, and H. Kroemer, *Zero-field spin splitting in InAs-AlSb quantum wells revisited,* Phys. Rev. B **60**, R13989 (1999).

[16] Y. S. Gui, C. R. Becker, N. Dai, J. Liu, Z. J. Qiu, E. G. Novik, M. Schäfer, X. Z. Shu, J. H. Chu, H. Buhmann, and L. W. Molenkamp, *Giant spin-orbit splitting in a* HgTe *quantum well,* Phys. Rev. B **70**, 115328 (2004).

[17] M. Nishioka, B. A. Gurney, E. E. Marinero, and F. Mireles, *Zero field spin splitting in AlSb/InAs/AlSb quantum wells induced by surface proximity effects,* Appl. Phys. Lett. **95**, 242108 (2009).

[18] H. L. Stormer, Z. Schlesinger, A. Chang, D. C. Tsui, A. C. Gossard, and W. Wiegmann, *Energy Structure and Quantized Hall Effect of Two-Dimensional Holes,* Phys. Rev. Lett. **51**, 126 (1983).

[19] B. Habib, E. Tutuc, S. Melinte, M. Shayegan, D. Wasserman, S. A. Lyon, and R. Winkler, *Spin splitting in GaAs (100) two-dimensional holes,* Phys. Rev. B **69**, 113311 (2004).

[20] F. Nichele, A. N. Pal, R. Winkler, C. Gerl, W. Wegscheider, T. Ihn, and K. Ensslin, *Spin-orbit splitting and effective masses in p-type GaAs two-dimensional hole gases,* Phys. Rev. B **89**, 081306 (2014).

[21] G. M. Minkov, A. V. Germanenko, O. E. Rut, A. A. Sherstobitov, S. A. Dvoretski, and N. N. Mikhailov, *Hole transport and valence-band dispersion law in a HgTe quantum well with a normal energy spectrum,* Phys. Rev. B **89**, 165311 (2014).

[22] A. Zakharova, S. T. Yen, and K. A. Chao, *Strain-induced semimetal-semiconductor transition in InAs/GaSb broken-gap quantum wells,* Phys. Rev. B **66**, 085312 (2002).

[23] J. Li, W. Yang, and K. Chang, *Spin states in InAs/AlSb/GaSb semiconductor quantum wells,* Phys. Rev. B **80**, 035303 (2009).

[24] L.-H. Hu, C.-X. Liu, D.-H. Xu, F.-C. Zhang, and Y. Zhou, *Electric control of inverted gap and hybridization gap in type-II InAs/GaSb quantum wells,* Phys. Rev. B **94**, 045317 (2016).

[25] I. Knez, R. R. Du, and G. Sullivan, *Finite conductivity in mesoscopic Hall bars of inverted InAs/GaSb quantum wells,* Phys. Rev. B **81**, 201301 (2010).

[26] R. J. Nicholas, K. Takashina, M. Lakrimi, B. Kardynal, S. Khym, N. J. Mason, D. M. Symons, D. K. Maude, and J. C. Portal, *Metal-Insulator Oscillations in a Two-Dimensional Electron-Hole System,* Phys. Rev. Lett. **85**, 2364 (2000).

[27] F. Nichele, A. N. Pal, P. Pietsch, T. Ihn, K. Ensslin, C. Charpentier, and W. Wegscheider, *Insulating State and Giant Nonlocal Response in an* InAs/GaSb *Quantum Well in the Quantum Hall Regime,* Phys. Rev. Lett. **112**, 036802 (2014).

[28] S.-F. Tsay, J.-C. Chiang, Z. M. Chau, and I. Lo, $\boldsymbol{k}\cdot\boldsymbol{p}$ *finite-difference method: Band structures and cyclotron resonances of* $\mathrm{Al}_x\mathrm{Ga}_{1-x}\mathrm{Sb/InAs}$ *quantum wells,* Phys. Rev. B **56**, 13242 (1997).

[29] Y. Vasilyev, S. Suchalkin, K. von Klitzing, B. Meltser, S. Ivanov, and P. Kop'ev, *Evidence for electron-hole hybridization in cyclotron-resonance spectra of InAs/GaSb heterostructures,* Phys. Rev. B **60**, 10636 (1999).

[30] T. Ando, A. B. Fowler, and F. Stern, *Electronic properties of two-dimensional systems,* Rev. Mod. Phys. **54**, 437 (1982).

[31] P. T. Coleridge, R. Stoner, and R. Fletcher, *Low-field transport coefficients in GaAs/*$\mathrm{Ga}_{1-x}\mathrm{Al}_x$*As heterostructures,* Phys. Rev. B **39**, 1120 (1989).

[32] Y. A. Bychkov and E. I. Rashba, *Oscillatory effects and the magnetic susceptibility of carriers in inversion layers,* J. Phys. C: Solid State Phys. **17**, 6039 (1984).

[33] B. Huckestein, *Scaling theory of the integer quantum Hall effect,* Rev. Mod. Phys. **67**, 357 (1995).

[34] K. S. Novoselov, A. K. Geim, S. V. Morozov, D. Jiang, M. I. Katsnelson, I. V. Grigorieva, S. V. Dubonos, and A. A. Firsov, *Two-dimensional gas of massless Dirac fermions in graphene,* Nature **438**, 197 (2005).

[35] Y. Zhang, Y.-W. Tan, H. L. Stormer, and P. Kim, *Experimental observation of the quantum Hall effect and Berry's phase in graphene,* Nature **438**, 201 (2005).

[36] D.-X. Qu, Y. S. Hor, J. Xiong, R. J. Cava, and N. P. Ong, *Quantum Oscillations and Hall Anomaly of Surface States in the Topological Insulator Bi2Te3,* Science **329**, 821 (2010).

[37] J. Xiong, Y. Luo, Y. Khoo, S. Jia, R. J. Cava, and N. P. Ong, *High-field Shubnikov–de Haas oscillations in the topological insulator* Bi_2Te_2Se, Phys. Rev. B **86**, 045314 (2012).

[38] A. R. Wright and R. H. McKenzie, *Quantum oscillations and Berry's phase in topological insulator surface states with broken particle-hole symmetry,* Phys. Rev. B **87**, 085411 (2013).

[39] B.-M. Nguyen, W. Yi, R. Noah, J. Thorp, and M. Sokolich, *High mobility back-gated InAs/GaSb double quantum well grown on GaSb substrate,* Appl. Phys. Lett. **106**, 032107 (2015).

[40] S. Luryi, *Quantum capacitance devices,* Appl. Phys. Lett. **52**, 501 (1988).

[41] E. O. Kane, in *Handbook on Semiconductors,* Vol. 1, edited by W. Paul and F. John (North-Holland, Amsterdam, 1982) p. 193.

[42] G. Bastard, *Wave Mechanics Applied to Semiconductor Heterostructures* (Wiley, New York, 1988).

[43] E. Halvorsen, Y. Galperin, and K. A. Chao, *Optical transitions in broken gap heterostructures,* Phys. Rev. B **61**, 16743 (2000).

[44] P. Lawaetz, *Valence-Band Parameters in Cubic Semiconductors,* Phys Rev B **4**, 3460–3467 (1971).

[45] T. Andlauer and P. Vogl, *Full-band envelope-function approach for type-II broken-gap superlattices,* Phys. Rev. B **80**, 035304 (2009).

7

ORBITAL CONTRIBUTIONS TO THE ELECTRON g-FACTOR IN SEMICONDUCTOR NANOWIRES

This chapter has been previously published as Georg W. Winkler, Dániel Varjas, **Rafal Skolasinski**, Alexey A. Soluyanov, Matthias Troyer, and Michael Wimmer, *Orbital Contributions to the Electron g-factor in Semiconductor Nanowires*, Phys. Rev. Lett. **119**, 037701 (2017).

7.1. INTRODUCTION

Early electron spin resonance experiments in the 2D electron gas (2DEG) formed in AlGaAs/GaAs heterostructures found a reduced Landé g-factor of electrons [1], which was later theoretically explained to arise due to the electronic confinement [2–4]. It is by now well established that confinement in a nanostructure leads to a reduction in the g-factor[1] [6]—the subband confinement increases the energy gap, which is inversely proportional to $g^* - g_0$, where g^* is the effective and g_0 the free electron g-factor [6, 7]. Surprisingly, experiments in InAs [8, 9] and InSb [10, 11] nanowires found g-factors surpassing the corresponding bulk g-factors by up to 40%.

Recently, this discrepancy has attracted interest due to the experimental discovery of a zero bias conductance peak in semiconductor nanowires proximity coupled to an s-wave superconductor [12–17], which is believed to be a signature of the Majorana bound state [18–20] having possible applications in topological quantum computation [21, 22]. The electron g-factor of the semiconductor nanowire determines the strength of magnetic field required to trigger the topological phase transition in these systems. It is desirable to keep the magnetic field low since it also suppresses superconductivity, and thus a large g-factor semiconductor is desired. Furthermore, Majorana proposals based on magnetic textures [23–25] and various spintronic devices [26] require large g-factors. Small band-gap semiconductors like InAs and InSb are therefore the materials of choice for Majorana nanowires, having large g-factors and strong spin-orbit coupling (SOC).

In a recent experiment with InAs nanowires g-factors[2] more than three times larger than the bulk g-factor ($g^*_{\text{InAs}} = -14.9$ [6, 27]) were measured [15]. Moreover, it was found that the g-factor depends very strongly on the chemical potential μ tuned by the gate potential [28]. For low μ small g-factors where found which can be explained by the bulk g-factor of InAs. The anomalously large g-factors have been only detected at high chemical potential μ.

In this work, we present a mechanism that can lead to very large g-factors in higher subbands of nanowires and similarly shaped nanostructures. With this we can explain both the large g-factors observed in Refs. [8–10, 15], and the chemical potential dependence [28]. In particular, we find that the orbital angular momentum in the confined nanostructure plays a crucial role. The lowest conduction subband/state is characterized by no or only small orbital angular momentum. In this case the usual reasoning applies and confinement does lead to a reduction of the g-factor. Higher subbands/states, however, can have nonzero orbital angular momentum in an approximately cylindrical structure. Due to strong SOC in small band-gap semiconductors one finds an $\mathbf{L}\cdot\mathbf{S}$-type spin alignment if the orbital angular momentum $\mathbf{L}$ is nonzero. Kramers pairs of opposite orbital angular momentum form at $B = 0$, and thus the g-factor obtains an additional contribution resulting from the coupling of the orbital angular momentum to the magnetic field. A similar orbital enhancement of the g-factor is known from the theory of the hydrogen atom [29] and has also been observed in carbon nanotubes [30, 31]. However, due to the small effective mass the g-factor enhancement can be orders of magnitude larger in the semiconducting structures investigated here.

---

[1] With the exception of the exchange enhancement of g-factors [5].

[2] We measure the g-factors in units of the Bohr-magneton $\mu_B = \frac{e\hbar}{2m_0}$ and use the sign convention where the free electron g-factor is $g_0 \approx +2$.

7.2. LANDÉ g-FACTOR IN SYSTEMS WITH CYLINDRICAL SYMMETRY

We start by considering cylindrical nanowires and estimate the maximally achievable g-factor for subbands as a function of their orbital angular momentum. Initially, we assume independent SU(2) spin rotation symmetry (no SOC) and time-reversal (TR) invariance without magnetic field. We then introduce magnetic field parallel to the wire, thus preserving the rotational invariance (both in real space and spin) around the axis of the wire (z direction in the following).

As the wire is translationally invariant in the z direction, and the conduction band minimum is at $k_z = 0$, we restrict to $k_z = 0$ in the following and investigate the wavefunction in the xy plane only. As a consequence of separate real space and spin rotation symmetries, the states can be classified by their orbital angular momentum $L_z = 0, \pm\hbar, \pm 2\hbar$, etc. and spin $S_z = \pm\frac{\hbar}{2}$ (for brevity we drop the z subscript in the following and use the lower case letters for angular momentum in units of $\hbar$). The lowest subband is twofold spin degenerate $\left|l = 0, s = \pm\frac{1}{2}\right\rangle$, higher subbands with $l \neq 0$ being fourfold $\left|\pm|l|, \pm\frac{1}{2}\right\rangle$.

In a simple quadratic band with an effective mass m^*, the momentum and electrical current are related as $\mathbf{J} = \frac{e}{m^*}\mathbf{p}$. Using the orbital angular momentum $\mathbf{L} = \mathbf{r} \times \mathbf{p}$ the orbital magnetic moment is expressible as

$$\mathbf{M}_\text{o} = \frac{1}{2}\mathbf{r} \times \mathbf{J} = -\frac{e}{2m^*}\mathbf{L} = -\frac{m_0}{m^*}\mu_B l \mathbf{e}_z\,. \tag{7.1}$$

We see that the orbital magnetic moment is enhanced by the low effective mass of the bands. Because of the fourfold degeneracy, we cannot unambiguously calculate g-factors and thus next include spin-orbit coupling.

With SOC the orbital and spin angular momentum is no longer separately conserved, but the total angular momentum $f_z = l_z + s_z$ is still conserved and takes half-integer values. Without magnetic field the system is TR invariant. As angular momentum is odd under TR, the degenerate Kramers-pairs have opposite f. Turning on SOC splits the fourfold degeneracy of the $l \neq 0$ subbands into two degenerate pairs: $\left|+|l|, +\frac{1}{2}\right\rangle$ and $\left|-|l|, -\frac{1}{2}\right\rangle$ stay degenerate ($f = \pm(|l| + \frac{1}{2})$) and so do $\left|+|l|, -\frac{1}{2}\right\rangle$ and $\left|-|l|, +\frac{1}{2}\right\rangle$ ($f = \pm(|l| - \frac{1}{2})$), as shown in Fig. 7.1 (a). Even though the orbital and local angular momenta are no longer separately conserved their expectation values remain similar for realistic SOC strengths.

The magnetic field $\mathbf{B}$ couples to the total magnetic moment $\mathbf{M} = \mathbf{M}_o - g^* \frac{e}{2m_0}\mathbf{S}$ [4]. Using Eq. (7.1), the Zeeman splitting of a Kramer's pair $\left|\pm|l|, +\frac{1}{2}\right\rangle$ and $\left|\mp|l|, -\frac{1}{2}\right\rangle$ for a magnetic field in z-direction is given by $\Delta E_\text{Zeeman} = \mu_B(g^* \pm 2\frac{m_0}{m^*}|l|)\frac{B_z}{2}$ and the resulting effective g-factor can be read off

$$g_{|l|\pm\frac{1}{2}} = g^* \pm 2\frac{m_0}{m^*}|l|\,. \tag{7.2}$$

Below we will see from numerical simulation that this is a good approximation even in a less ideal case.

This result is analogous to the well known Landé g-factor of the Hydrogen atom when taking relativistic SOC into account: the splitting induced by weak external magnetic field has contributions from both the orbital and spin angular momentum [29]. This effect is

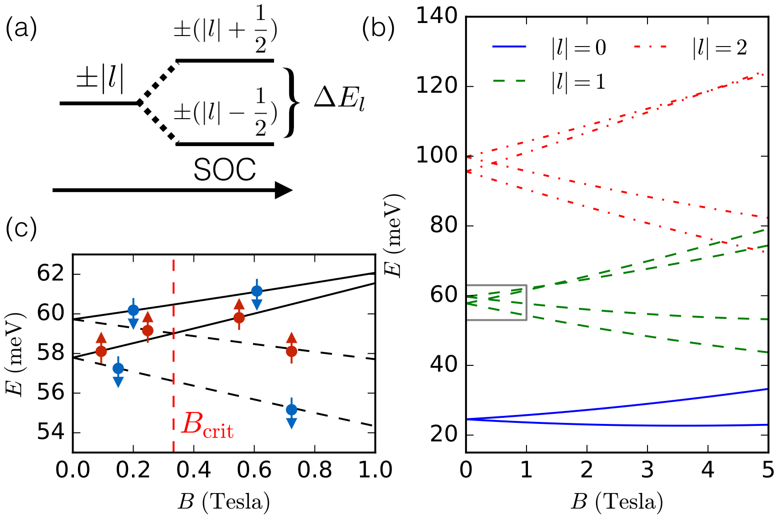

Figure 7.1: (a) Evolution of the energy levels at $k_z = 0$ in cylindrical symmetry when SOC is turned on. (b) Energy levels of a cylindrical InSb wire with 40 nm diameter in an axial magnetic field. (c) Zoom in on the $|l| = 1$ states marked by the gray rectangle in (b). Dashed lines are $l = +1$, and solid lines $l = -1$, states. The spin alignments are marked by the small arrows and the vertical dashed red line marks $B_{\rm crit}$.

amplified in semiconductor nanostructures because the small effective mass increases both the orbital magnetic moment and the bulk g-factor g^*.

7.3. NUMERICAL CALCULATIONS

We next validate our theoretical findings with simulations of nanowires using an eight-band **k**·**p**-model for zincblende semiconductors [6, 32, 33]. At first, we assume perfect cylindrical symmetry of a nanowire, grown in 001 direction, and employ the axial approximation [34–36], that we discuss further in Chapter 7.6.1. In this case, the wavefunctions can be written as [37]

$$\psi(\rho,\phi,z) = \sum_n g_n(\rho,z)e^{il_n\phi}|u_n\rangle\,, \tag{7.3}$$

where $|u_n\rangle$ are the basis states of the 8-band **k**·**p** Hamiltonian with local angular momentum j_n.[3] Since the Hamiltonian conserves the total angular momentum f one obtains the orbital part of each component as $l_n = f - j_n$. If we furthermore focus on an infinite wire in the z-direction the problem is reduced to a 1D boundary value problem in ρ which we solve using the finite difference method, Chapter 7.6.2.

Figure 7.1 (b) shows the subband edges of an InSb nanowire of 40 nm diameter. At $B = 0$ one generically finds the lowest conduction subband to originate from the $|l| = 0$ state without SOC. At higher energy there are the $|l| = 1$ and $|l| = 2$ states and then another $|l| = 0$ state with a higher radial quantum number (not shown). This order of states is generic as long as the conduction band is approximately quadratic [38]. Figure 7.1 (c)

---

[3] Here j takes the role of s in the previous argument, as in these materials the p-type orbitals have nonzero local orbital angular momentum and are treated as spin-3/2 degrees of freedom.

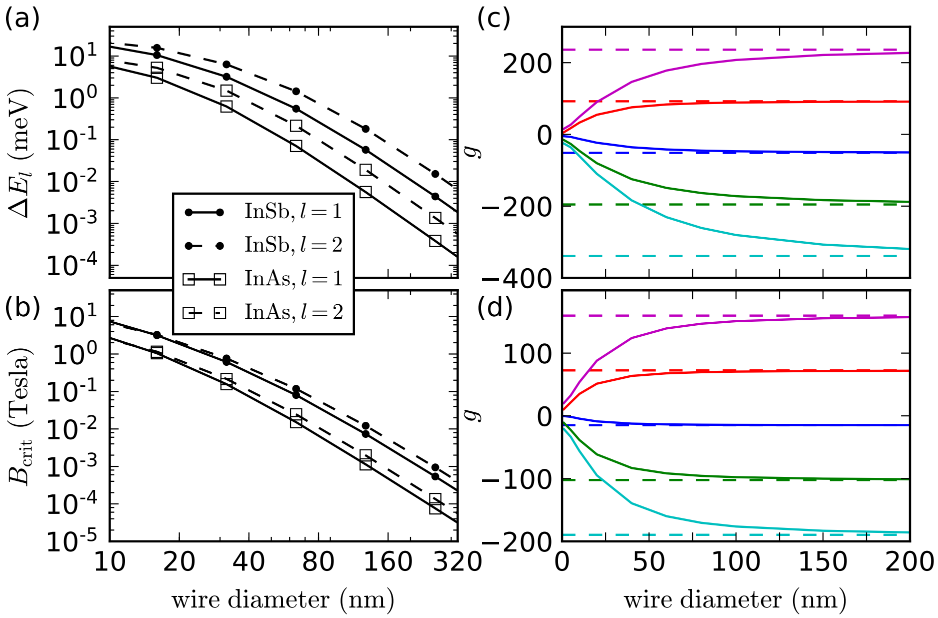

Figure 7.2: (a) Diameter dependence of the SOC splitting ΔE_1 and ΔE_2 for InSb and InAs wires. (b) Diameter dependence of the critical magnetic field B_{crit} defined in Fig. 7.1 (b). (c)((d)) Effective g-factors at infinitesimal magnetic field of the first five subbands of an InSb (InAs) wire: $l = 0, |f| = \frac{1}{2}$ (blue), $|l| = 1, |f| = \frac{1}{2}$ (green), $|l| = 1, |f| = \frac{3}{2}$ (red), $|l| = 2, |f| = \frac{3}{2}$ (cyan) and $|l| = 2, |f| = \frac{5}{2}$ (magenta). The dashed lines in the corresponding colors are the prediction of Eq. (7.2) where we substituted bulk values.

zooms in on the $|l| = 1$ subbands. Due to SOC the $|f| = \frac{3}{2}$ and $|f| = \frac{1}{2}$ states are split at $B = 0$ by $\Delta E_1 \approx 2\,\text{meV}$. If a magnetic field $B < B_{\text{crit}}$ (see Fig. 7.1 (c)) is turned on a splitting between states of opposite orbital angular momentum l is observed and thus, enhanced g-factors according to Eq. (7.2). However, when the magnetic field is large, $B > B_{\text{crit}}$, states of the same orbital angular momentum bundle together and their relative slope with respect to B corresponds to the normal g-factor without orbital contributions. Thus a splitting ΔE_l is a crucial ingredient for enhanced g-factors.

Figure 7.2 shows the dependence on the diameter of the nanowire. From the ΔE_l dependence it is evident that the wire cannot be made too thick to experimentally observe the effect with a detectable energy scale, e.g. to distinguish the split energy levels using Coulomb oscillations [39]. Figures 7.2 (c) and (d) show that at large wire diameters Eq. (7.2) is reproduced perfectly by numerics, but for small diameters the g-factor enhancement is reduced by the confinement. Thus, the optimal diameter range where enhancement of the g-factor is strong and at the same time ΔE_l and B_{crit} are large enough is in between 10 and 100 nm. We see that the g-factors of higher subbands can be very large—enhancements of an order of magnitude compared to the bulk g-factor are possible.

The splitting ΔE_l is generic if SOC is present, since in a typical semiconductor wire with SOC there is no symmetry that would protect the degeneracy between states of different total angular momentum. The conduction band of zincblende semiconductors has a purely s-orbital character at the Γ-point of the Brillouin zone (BZ), which is insensitive to SOC. Thus, also the conduction subbands of a zincblende nanowire are mostly derived from s-orbitals. Any nonzero splitting ΔE_l results from p-like hole contributions to the conduction band due to confinement. This explains why the splitting in the conduction band is so small compared to the split-off energy of the valence bands Δ, which is 0.81 eV for InSb and 0.38 eV for InAs [6].

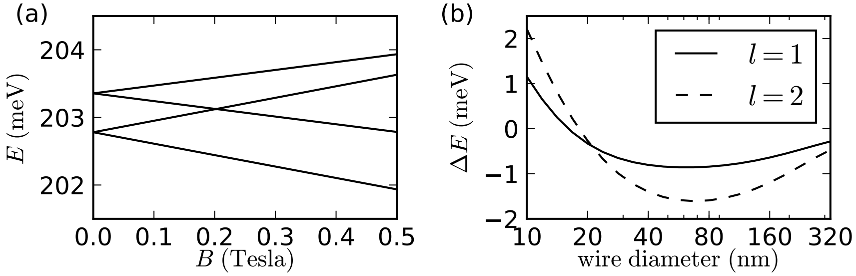

Figure 7.3: (a) Energy levels of the lowest $|l| = 1$ states as a function of B in a tight-binding simulation of a hexagonal InSb wire of 20.1 nm diameter, grown in the 111 direction. (b) SOC splitting as a function of diameter in a cylindrical wurtzite InAs wire.

Since ΔE_l results from the scattering of states at the surface of the wire, the boundary conditions impact the numerical value, and even the sign, of ΔE_l, see Chapter 7.6.1. Abrupt boundaries can be problematic in $\mathbf{k}\cdot\mathbf{p}$ simulations [40], therefore, we use tight-binding (TB) simulations to check the robustness of our results, Chapter 7.6.2. The effective tight-binding Hamiltonian is generated from the first-principles s and p-like Wannier functions [41], calculated using the Vienna *ab initio* simulation package (VASP) [42–45] with the projector augmented-wave method [46, 47], a cut-off energy of 300 eV, a 8×8×8 Monkhorst-Pack mesh and using the HSE06 hybrid functional [48–50]. Furthermore, the TB model includes the Dresselhaus term which was neglected for the zincblende $\mathbf{k}\cdot\mathbf{p}$ simulations since its effect is found to be very small, Chapter 7.6.1. In Fig. 7.3 (a) we show the magnetic field dependence of the $|l| = 1$ subbands in a hexagonal InSb wire. The g-factors of -59 and +40 and $B_{\text{crit}} \approx 0.2$ Tesla agree qualitatively with the $\mathbf{k}\cdot\mathbf{p}$-results.

While in zincblende wires boundary effects are dominating, in wurtzite wires the situation is different: There, the conduction band has a mixed s and p character. Thus, wurtzite wires have an intrinsic splitting independent of confinement [51]. Using a $\mathbf{k}\cdot\mathbf{p}$-model for wurtzite semiconductors [52], we find a nearly size-independent ΔE_l of order 1 meV for [0001] grown wurtzite InAs wires for experimentally used diameters of 40 to 160 nm [53], see Fig. 7.3 (b). At very large wire diameters > 200 nm the confinement induced subband splitting becomes smaller than ΔE_l, leading to a reduction of ΔE_l, and at very small diameters < 20 nm the cubic Dresselhaus term dominates over the linear Rashba term, causing a sign change in ΔE_l [54], Chapter 7.6.1.

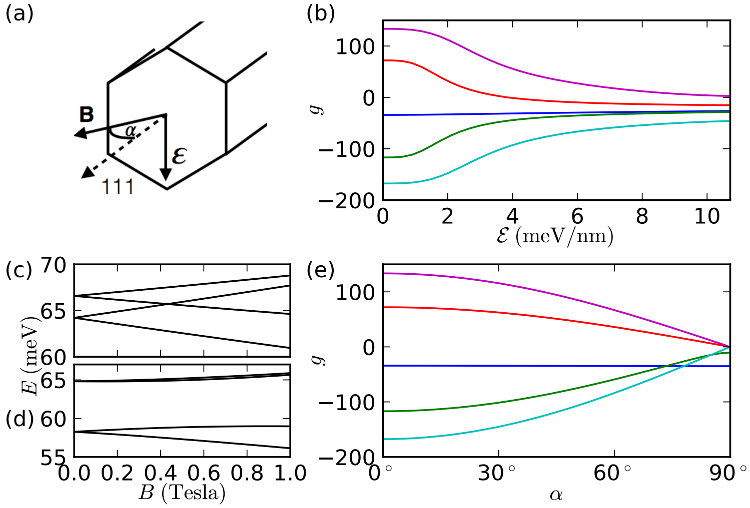

Figure 7.4: (a) Magnetic and electric field directions in the hexagonal 111 wire. (b) The g-factors measured at 0.2 Tesla ($\alpha = 0$) of a hexagonal InSb wire with 40 nm diameter as a function of a perpendicular electric field. (c) ((d)) Energy levels of the $|l| = 1$ states as a function of B at an electric field of $\mathcal{E} = 0\,\mathrm{meV/nm}$ ($\mathcal{E} = 3\,\mathrm{meV/nm}$). (e) The g-factors as a function of α measured at 0.2 Tesla in a hexagonal InSb wire with 40 nm diameter. In (b) and (e) the color code is the same as in Fig. 7.2 (c/d).

7.4. LANDÉ g-FACTOR IN SYSTEMS WITH BROKEN CYLINDRICAL SYMMETRY

We now consider the effects of broken cylindrical symmetry and solve the full 2D cross section of hexagonal zincblende wires, grown in the 111 direction, using a 2D discretization of the **k**·**p**-model [55], Chapter 7.6.3. We allow for symmetry breaking by electric field and off-axis magnetic field, see Fig. 7.4 (a) for the definitions of the relevant directions. In experimental situations, the symmetry is generally broken by electric fields, e.g. due to the backgate for tuning the electron density in the wire [8, 10, 15, 28]. We find that, especially in higher subbands, the enhanced g-factors are quite robust to an external electric field.

In Fig. 7.4 (b-d) we simulate a hexagonal InSb wire, of 40 nm diameter, in a perpendicular external electric field $\mathcal{E}$. The point group of the wire at $\mathcal{E} = 0$ is C_{3v} and crossings between states of different angular momentum are protected, as illustrated in Figure 7.4 (c). At nonzero $\mathcal{E}$ the different angular momentum eigenstates hybridize, which reduces their orbital angular momentum expectation value. However, as shown in Figs. 7.4 (b) and (d), the orbital contribution to the g-factor remains very significant until very large fields are applied. Bands with larger values of $|l|$ have larger splitting ΔE_l and, therefore, the orbital contribution to their g-factors is more robust and can remain significantly larger than the bulk g-factor until large electric fields, e.g. see the cyan and magenta lines corresponding to $|l| = 2$ in Fig. 7.4 (b).

The electron g-factor anisotropy in the magnetic field of 2DEGs is well established [3, 6, 56, 57]. In our case of orbitally enhanced g-factors in nanowires we expect an even

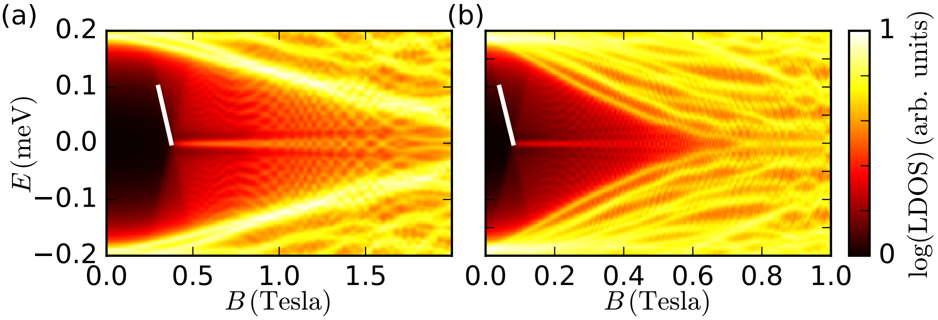

Figure 7.5: (a) ((b)) show the local density of states (LDOS) at the end of an InAs wire with 40 nm diameter and 2172 nm length in an electric field of $\mathcal{E} = 1.2\,\text{meV/nm}$ and proximity effect induced superconducting pairing $\Delta = 0.2\,\text{meV}$. The chemical potential $\mu = 39.6\,\text{meV}$ ($\mu = 68.5\,\text{meV}$) is tuned to the $|l| = 1$ ($|l| = 2$) subbands. The slope of the whites lines amount to a g-factor of 23 (43).

stronger anisotropy. Indeed, the electron spins in subbands with $l \neq 0$ feel a very strong orbital magnetic field that aligns them (anti-) parallel to the wire axis. Therefore, a perpendicular magnetic field first needs to overcome this orbital effect to create a Zeeman splitting of the states [30, 31].

This is illustrated in Fig. 7.4 (e), where we simulate a hexagonal InSb wire of 40 nm diameter in a magnetic field of 0.2 Tesla. We show there the g-factor as a function of the angle α between the magnetic field and the nanowire axis. While the g-factor of the lowest $l = 0$ subband is unaffected by the direction of $\mathbf{B}$, the g-factor for bands with $l \neq 0$ almost vanishes for perpendicular magnetic field. This strong anisotropy of the electron g-factor can be used in experiments to prove the important role of orbital angular momentum in nanowires.

In a Majorana wire circular symmetry breaking by gate potentials and band bending is mandatory to create a Rashba effect in the wire [19, 20, 58]. The results shown above suggest that even in such an environment orbital effects still dominate the g-factors of certain subbands in wires. This is illustrated in Fig. 7.5 (a) and (b), where we simulate an InAs wire proximity coupled to an Al superconductor, Chapter 7.6.3. When the chemical potential is tuned to the $|l| = 1$ and $|l| = 2$ subbands, the g-factors, extracted from the slope of the Majorana state forming Andreev bound state, are 23 and 43[4], respectively. These g-factors are significantly larger than the bulk g-factor of InAs, thus reproducing the experimental result of Ref. [15].

7.5. CONCLUSIONS

In summary, we have provided a theory for the previously unexplained large g-factors observed in nanowires. Our findings help to better understand and optimize Majorana experiments. Similar results apply to quantum dots. For cylindrical quantum dots we find that orbital g-factor enhancements are still significant if the length of the dot is much shorter than its diameter. Due to the observed robustness of the effect, it also applies in

---

[4] Our simulations do not include the effects of the superconductor [59, 60], which could lead to a reduction of the resulting g-factor.

irregularly shaped quantum dots and can explain g-factor fluctuations there.

7.6. SUPPLEMENTARY INFORMATION

7.6.1. SOLVING CYLINDRICAL NANOSTRUCTURES IN THE AXIAL APPROXIMATION

NUMERIC SIMULATIONS EMPLOYING THE AXIAL APPROXIMATION

The cylindrical symmetry of a quantum wire allows for a considerable reduction in the computational effort of simulating the wire. To make use of this we furthermore assume that the zincblende structure itself has cylindrical symmetry by employing the so-called axial approximation [35]. In this approximation the **k**·**p**-Hamiltonian has continuous rotational symmetry about the principal axis of the crystal. In this section we consider wires consisting of a zincblende semiconductor grown in the 001 direction and wurtzite semiconductor in the 0001.

In its simplest form the axial approximation amounts to equalling the two Luttinger-Kohn parameters $\gamma_2 = \gamma_3$. We choose to set $\gamma_2 = \gamma_3$ only in the terms of the Kane Hamiltonian [32] that would otherwise break the cylindrical symmetry. For the exact definition of the Hamiltonian see Tab. V in Ref. [34]. The **k**·**p**-parameters of InAs and InSb are taken from Ref. [6]. Throughout the paper, we avoid spurious solutions by renormalizing the bare electron mass to $\gamma_0 = 5$ [33, 61].

Within the axial approximation, the wave-function can be written as [37]

$$\psi(\rho,\phi,z) = \sum_n g_n(\rho,z) e^{i l_{zn}\phi} |u_n\rangle, \tag{7.4}$$

where $|u_n\rangle$ are the basis states for the 8-band **k**·**p** Hamiltonian $|j_{\text{tot}}, j_z\rangle$:

$$\begin{aligned} &|u_1\rangle = |\tfrac{1}{2}, \ \tfrac{1}{2}\rangle, \quad |u_2\rangle = |\tfrac{1}{2}, -\tfrac{1}{2}\rangle, \quad |u_3\rangle = |\tfrac{3}{2}, \ \tfrac{3}{2}\rangle, \quad |u_4\rangle = |\tfrac{3}{2}, \ \tfrac{1}{2}\rangle, \\ &|u_5\rangle = |\tfrac{3}{2}, -\tfrac{1}{2}\rangle, \quad |u_6\rangle = |\tfrac{3}{2}, -\tfrac{3}{2}\rangle, \quad |u_7\rangle = |\tfrac{1}{2}, \ \tfrac{1}{2}\rangle, \quad |u_8\rangle = |\tfrac{1}{2}, -\tfrac{1}{2}\rangle. \end{aligned} \tag{7.5}$$

The states $|u_1\rangle$ and $|u_2\rangle$ derive from s-orbitals, whereas the remaining basis states are derived from p-orbitals. Since the Hamiltonian is block-diagonal in the total angular momentum f_z one obtains the orbital part of each component $l_{zn} = f_z - j_{zn}$.

The Hamiltonian is transformed into polar coordinates $(x, y, z) \to (\rho, \phi, z)$

$$H_{ij}^{\text{Polar}}(\rho,\phi,z) = e^{-i(f_z - j_{zi})} H_{ij}^{\text{Cartesian}}(x,y,z) e^{i(f_z - j_{zj})}, \tag{7.6}$$

where the ϕ-dependece of H^{Polar} drops out due to the axial approximation. The momenta k_x and k_y are transformed by

$$\begin{aligned} k_x &= -i\frac{\partial}{\partial x} = -i(\cos\phi\frac{\partial}{\partial\rho} - \frac{\sin\phi}{\rho}\frac{\partial}{\partial\phi}) = \cos\phi\, k_\rho - \frac{\sin\phi}{\rho}k_\phi, \\ k_y &= -i\frac{\partial}{\partial y} = -i(\sin\phi\frac{\partial}{\partial\rho} + \frac{\cos\phi}{\rho}\frac{\partial}{\partial\phi}) = \sin\phi\, k_\rho + \frac{\cos\phi}{\rho}k_\phi. \end{aligned} \tag{7.7}$$

Below we write all the terms that appear in the Hamiltonian and need to be transformed

(note that k_ρ and k_ϕ do not commute when the magnetic field is turned on)

$$k_+ = k_x + ik_y = e^{i\phi}(k_\rho + \frac{i}{\rho}k_\phi), \tag{7.8}$$

$$k_- = k_x - ik_y = e^{-i\phi}(k_\rho - \frac{i}{\rho}k_\phi), \tag{7.9}$$

$$(k_+)^2 = e^{2i\phi}[k_\rho^2 + \frac{i}{\rho}k_\rho + \frac{i}{\rho}(k_\rho k_\phi + k_\phi k_\rho) + \frac{1}{\rho^2}(-2k_\phi - k_\phi^2)], \tag{7.10}$$

$$(k_-)^2 = e^{-2i\phi}[k_\rho^2 + \frac{i}{\rho}k_\rho - \frac{i}{\rho}(k_\rho k_\phi + k_\phi k_\rho) + \frac{1}{\rho^2}(2k_\phi - k_\phi^2)], \tag{7.11}$$

$$k_x^2 + k_y^2 = k_\rho^2 - \frac{i}{\rho}k_\rho + \frac{1}{\rho^2}k_\phi^2. \tag{7.12}$$

According to Eq. (7.4), in the final matrix elements H_{ij}, one needs to replace each occurence of k_ϕ by $l_{zn} = f_z - j_{zn}$.

For a uniform magnetic field **B** in the z direction the vector potential may be taken as

$$A_z = A_\rho = 0, \quad A_\phi = \frac{1}{2}B\rho, \tag{7.13}$$

which can be included in the simulation by substituting

$$k_\phi \to k_\phi - \frac{\pi}{2\phi_0}B\rho, \tag{7.14}$$

where ϕ_0 is the magnetic flux quantum.

7

We solve the system of coupled differential equations for the eigenmodes by rewriting it first to a generalized eigenvalue problem

$$H\mathbf{v}_n = E_n C\mathbf{v}_n, \tag{7.15}$$

where H is the Hamiltonian with substituted discretized expressions for the differential operators. The indices i, j of H_{ij} run over both the basis states Eq. (7.5) and the discretized radial positions ρ.

We have to consider boundary conditions of both Dirichlet type $v_{ni} = 0$ and Neumann type $v_{ni} - v_{n(i+1)} = 0$. If i corresponds to a position with $\rho = W$, with W being the radius of the wire, the Dirichlet condition is taken. If i corresponds to $\rho = 0$ the Dirichlet condition is taken for $l_z \neq 0$ and the Neumann condition for $l_z = 0$. Thus, the matrix C_{ij}, which encodes the boundary conditions, has only diagonal elements which are 1 if i corresponds to an interior site of the wire and 0 if i is either at $\rho = 0$ or $\rho = W$.

ANALYTIC ESTIMATES FOR THE SPIN-ORBIT SPLITTING

We calculate the spin-orbit interaction (SOI) splitting δE of the subbands perturbatively in the rotational invariant case with $\gamma_2 = \gamma_3$ in a circular wire. We use the continuum Hamiltonian in cylindrical coordinates. Starting from the exact solution in the $\gamma_1 = \gamma_2 = \gamma_3 = 0$ case [36] we find a splitting that lowers the energy of subbands with parallel orbital and spin angular momentum using the minimal boundary amplitude condition. This splitting scales as W^{-4} for thick wires and as Δ for small Δ.

Exact solution of a special case The real-space continuum problem can be exactly solved for the electron-like wave functions when $\gamma_1 = \gamma_2 = \gamma_3 = 0$. Following Ref. [36] we express the hole-like components in terms of the electron-like ones from the Schrödinger equation, and substitute it back to the electron component equation to get the Helmholtz-equation

$$\left\{ \left[\frac{P^2}{3} \left(\frac{2}{E+E_0} + \frac{1}{E+E_0+\Delta} \right) + \frac{\gamma_0}{2m_0} \right] \nabla^2 + E \right\} \psi_{e\sigma}(\mathbf{r}) = 0 \tag{7.16}$$

where ∇^2 is the Laplacian, E is the (unknown) energy of the state and $\psi_{e\sigma}(\mathbf{r})$ is the wave function amplitude in the electron-like bands (the equations are identical for the two spin sectors). The full wave-function, including the hole-like components can be written as

$$\psi_\uparrow(\mathbf{r}) = \begin{pmatrix} 1 & 0 & -\frac{k_-P}{\sqrt{2}(E_0+E)} & \frac{\sqrt{\frac{2}{3}}k_zP}{E_0+E} & \frac{k_+P}{\sqrt{6}(E_0+E)} & 0 & -\frac{k_zP}{\sqrt{3}(\Delta+E_0+E)} & -\frac{k_+P}{\sqrt{3}(\Delta+E_0+E)} \end{pmatrix} \psi_{e\uparrow}(\mathbf{r}) \tag{7.17}$$

$$\psi_\downarrow(\mathbf{r}) = \begin{pmatrix} 0 & 1 & 0 & -\frac{k_-P}{\sqrt{6}(E_0+E)} & \frac{\sqrt{\frac{2}{3}}k_zP}{E_0+E} & \frac{k_+P}{\sqrt{2}(E_0+E)} & -\frac{k_-P}{\sqrt{3}(\Delta+E_0+E)} & \frac{k_zP}{\sqrt{3}(\Delta+E_0+E)} \end{pmatrix} \psi_{e\downarrow}(\mathbf{r}) \tag{7.18}$$

where for a cylindrical wire the momenta can be written in cylindrical coordinates as in Eq. (7.7). The hole-like components of the real space wave-function are obtained by acting with the differential operators on the electron-like wave-function on the right.

As the equation is invariant under rotations around the z axis and translations along the z axis, the wave-function can be separated as $\psi_{e\uparrow}(\rho,\phi,z) = R_{l\sigma}(\rho)e^{il\phi}e^{ik_zz}$, substituting this we get the Bessel equation for the radial part

$$\left(\frac{d^2}{d\rho^2} + \frac{1}{\rho}\frac{d}{d\rho} - \frac{l^2}{\rho^2} + \chi^2 \right) R_{l\sigma}(\rho) = 0 \tag{7.19}$$

with

$$\chi^2 = -k_z^2 + E \Big/ \left[\frac{P^2}{3} \left(\frac{2}{E+E_0} + \frac{1}{E+E_0+\Delta} \right) + \frac{\gamma_0}{2m_0} \right] \tag{7.20}$$

where χ is the radial wavenumber and is determined by the boundary conditions. The solutions can be written in terms of Bessel functions $R_{l\sigma}(\rho) = J_l(\chi\rho)$. Setting $k_z = 0$, the full wave function can be written as:

$$\psi_{l\uparrow}(\rho,\phi) = \begin{pmatrix} 1 & 0 & \frac{ie^{-i\phi}P(l+ik_\rho\rho)}{\sqrt{2}(E_0+E)\rho} & 0 & \frac{e^{i\phi}P(il+k_\rho\rho)}{\sqrt{6}(E_0+E)\rho} & 0 & 0 & -\frac{e^{i\phi}P(il+k_\rho\rho)}{\sqrt{3}(\Delta+E_0+E)\rho} \end{pmatrix} R_{l\uparrow}(\rho), \tag{7.21a}$$

$$\psi_{l\downarrow}(\rho,\phi) = \begin{pmatrix} 0 & 1 & 0 & \frac{ie^{-i\phi}P(l+ik_\rho\rho)}{\sqrt{6}(E_0+E)\rho} & 0 & \frac{e^{i\phi}P(il+k_\rho\rho)}{\sqrt{2}(E_0+E)\rho} & \frac{ie^{-i\phi}P(l+ik_\rho\rho)}{\sqrt{3}(\Delta+E_0+E)\rho} & 0 \end{pmatrix} R_{l\downarrow}(\rho), \tag{7.21b}$$

where we used that the action on our ansatz amounts to the replacement of k_ϕ with l. The different hole-like Bloch states have different internal angular momentum, but the total angular momentum of each component is the same, this is manifest in the extra orbital phase factors in the expression.

The hole-like contribution is proportional to the radial derivative of the wave function. As the Bessel-functions cannot have both vanishing magnitude and derivative at finite ρ, it is not possible to demand vanishing of all components of the wave function at the boundary. In the large wire (large W and small χ) limit the hole-like amplitude is suppressed, so demanding the electron-like component to vanish is approximately a good boundary condition.

Minimal boundary amplitude boundary condition We assume that the system is infinite, but the states are confined by a large potential V at the boundary. Assuming V is much larger than any of the energy scales in the problem, then the wave function decays exponentially outside as

$$\psi(W) \approx e^{-(\rho-W)\sqrt{\frac{2m^*}{\hbar^2}V}} \tag{7.22}$$

where W is the radius of the wire where the potential step is. The expectation value of the potential energy goes as $\sqrt{\frac{\hbar^2}{2m^*}V}|\psi(W)|^2$, so in the large V limit the wave function amplitude is minimized, and the states get shifted up as $\sqrt{V}$.

We express the magnitude squared of the wave function on the boundary using our previous expression.

$$|\psi_{l\sigma}(W,\phi)|^2 = R^2\left(1+\frac{l^2(2a+b)}{3W^2}\right)+\sigma l R R'\frac{2(a-b)}{3W^2}+\left(R'\right)^2\frac{(2a+b)}{3W^2} \tag{7.23}$$

where $\sigma = \pm 1$ stands for up and down spin,

$$a = \frac{P^2}{(E_0+E)^2}, \tag{7.24}$$

$$b = \frac{P^2}{(E_0+E+\Delta)^2} \tag{7.25}$$

are constants with length squared dimension and we introduced the dimensionless quantity $\chi' = \chi W$, such that $R = J_l(\chi W) = J_l(\chi')$ and $R' = W\frac{dJ_l}{d\rho}(\chi W) = \chi' J_l'(\chi')$. It can be seen that in the $W^2 \gg a,\ b$ limit (for InSb $b < a \approx 10\text{nm}^2$) the total amplitude can be minimized by minimizing the amplitude in the electron bands. This happens when $\chi' = z_{lp}$, the p'th root of J_l.

For finite W we expand around this solution. To get a tractable approximation we can treat R and R' as independent variables and express R that minimizes the amplitude in terms of R':

$$R = -\sigma l R'\frac{(a-b)}{3W^2+(2a+b)l^2}. \tag{7.26}$$

The right hand side does not depend on γ_0 and is linear in Δ for small values and E can be set to zero for approximate calculations if the subband energy is much smaller than the bandgap, $E \ll E_0$. We expand both sides to first order in $\delta\chi' = \chi' - z_{lp}$ and use the identity[5] $J_l'(z_{lp}) + z_{lp}J_l''(z_{lp}) = 0$ to get

$$\delta\chi' = -\sigma l z_{lp}\frac{a-b}{3W^2+(2a+b)l^2}. \tag{7.27}$$

---

[5] This follows from the identity $\frac{l^2-x^2}{x}J_l(x) = J_l'(x) + xJ_l''(x)$.

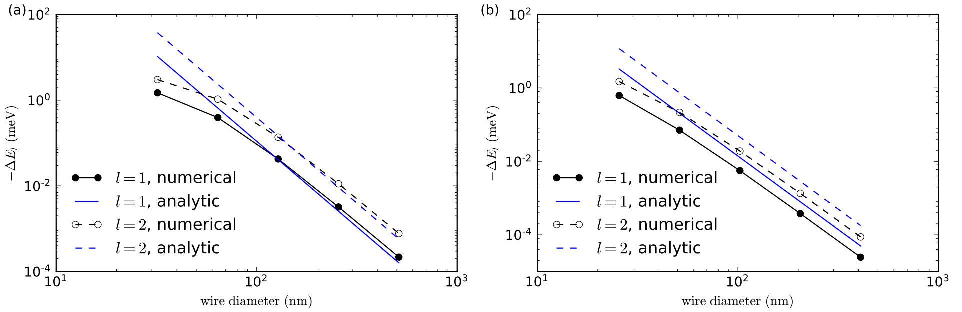

Figure 7.6: (a) ((b)) Diameter dependence of the SOI splitting ΔE_1 and ΔE_2 for InSb (InAs) wires with soft boundary conditions. The analytic approximation of Eq. (7.30) is shown for comparison.

Such a change in χ' effectively renormalizes the radius of the wire and results in a splitting between states with different total angular momentum. From Eq. (7.20) the energy E of a state in the small χ (large W, small l and p and small E) limit is approximately

$$E_{lp} = \frac{z_{lp}^2 P^2}{3W^2} \frac{3E_0 + 2\Delta}{E_0(E_0 + \Delta)}. \tag{7.28}$$

where we set $\chi = z_{lp}/W$ ignoring SO corrections. Note that this approximation does not depend on γ_0. Substituting χ' with $\chi' + \delta\chi'$ from (7.27) and expanding to linear order the energy change induced by SOI is

$$\delta E_{lp\sigma} = -\sigma l \frac{2E_{lp}(a-b)}{3W^2 + (2a+b)l^2}. \tag{7.29}$$

In the large W limit the subband splitting is (dotted lines in Fig. 7.6)

$$E_{lp\uparrow} - E_{lp\downarrow} = -l \frac{4z_{l,p}^2 P^4 \Delta(\Delta + 2E_0)(2\Delta + 3E_0)}{9W^4 E_0^3 (\Delta + E_0)^3}, \tag{7.30}$$

which for the lowest $l = 1$ subband gives

$$E_{11\uparrow} - E_{11\downarrow} \approx -\frac{1}{W^4} 687\,\mathrm{eV\,nm}^4 \tag{7.31}$$

where in the last approximation we used the renormalized parameters for InSb [33, 61], note that W is the *radius* of the wire.

In the above calculation we used the linearized expression for E and set $E = 0$ in a and b. A more precise result can be obtained for thin wires by numerically solving the third order Eq. (7.20) for E with $\chi' = z_{lp}$ (no SOI), substituting it in Eq. (7.27) and calculating the energy at the modified χ' by again using Eq. (7.20).

Numerical results for wires with soft boundary conditions

All results shown in the main text refer to the hard boundary condition case, where the wave functions is set to zero at the boundary of the wire. Here we instead apply a step

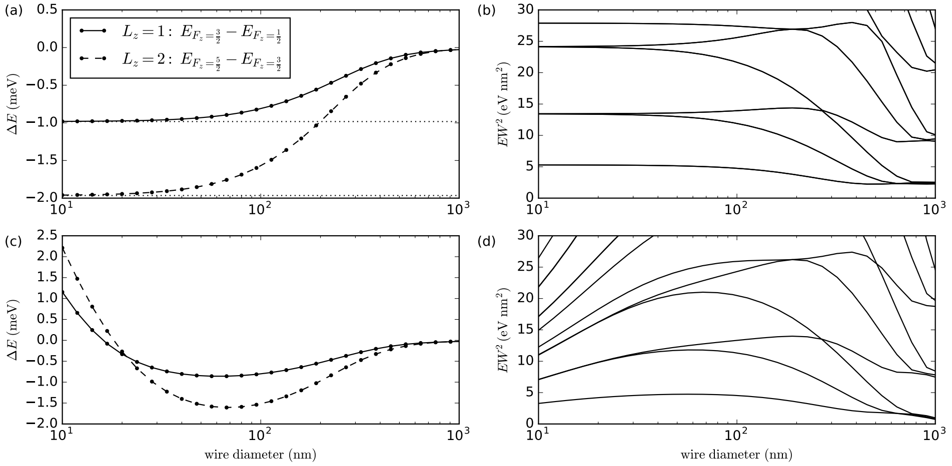

Figure 7.7: (a) SOI splitting in the Rashba model wire as a function of wire diameter. The dotted lines are the analytical result of Eq. (7.33). (b) Rescaled energies as a function of wire diameter. (c) ((d)) SOI splitting (rescaled energy levels) in an InAs wire obtained by an 8-band **k**·**p**-model for wurtzite InAs.

potential, which is set to zero inside the wire and 0.2 eV outside of the wire. This mimics the minimal amplitude boundary condition referred to above.

Most results, like the g-factors and the magnitude of ΔE_l, are very similar with soft and hard boundary conditions. The most striking difference is that, for soft boundary conditions, and zero magnetic field, the Kramers pair $\left|\pm|l|,\mp\frac{1}{2}\right\rangle$ is higher in energy than the Kramers pair $\left|\pm|l|,\pm\frac{1}{2}\right\rangle$. Thus ΔE_l has a negative sign in the soft boundary case.

In Fig. 7.6 we show the SOI splitting for wires with soft boundary conditions. Apart from the sign, the asymptotic behavior is identical. Especially, the $\frac{1}{W^4}$ dependence for large W, as in Eq. (7.30), is present in both the soft and hard boundary case. Generally, the agreement of the numerics with the analytic approximation Eq. (7.30) is quite good.

NUMERICAL RESULTS FOR WURTZITE WIRES

Here we consider InAs wurtzite wires in the 0001 growth direction, as they have been used in Majorana experiments [15]. The main difference in the conduction band of a wurtzite-type semiconductor to a zincblende one is the linear Rashba-like spin-splitting in directions orthogonal to the 0001 wurtzite direction [51]. Therefore, the SOI splitting has a contribution originating from this linear spin splitting. Apart from the origin of the SOI splitting, the mechanism for the enhancement of g-factors in wurtzite wires is equivalent to zincblende wires.

We describe the conduction band of wurtzite InAs by a Rashba model

$$H = -\frac{\hbar^2}{2}\left(\frac{k_x^2+k_y^2}{m_\perp}+\frac{k_z^2}{m_\parallel}\right)+\alpha\left(\sigma_x k_y-\sigma_y k_x\right). \tag{7.32}$$

using $m_\perp = 0.0416\,m_e$ and $m_\parallel = 0.0370\,m_e$ [54] and $\alpha = 0.03\,\text{eVnm}$ [52]. We solve this model in an infinite wire geometry using cylindrical coordinates as described above. In

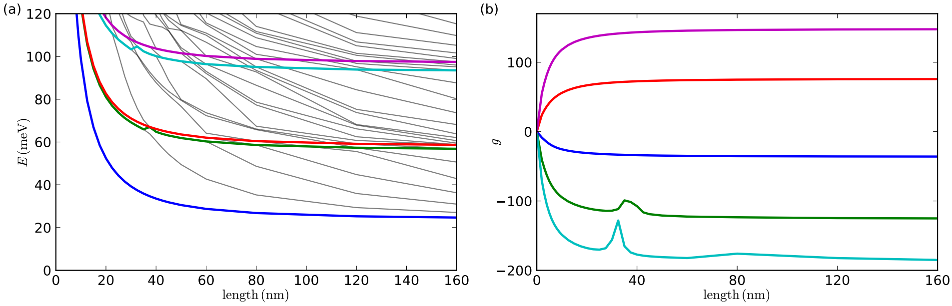

Figure 7.8: (a) ((b)) The energy levels (g-factors) in a cylindrical InSb quantum dot with 40 nm diameter and variable length. The g-factors where evaluated at infinitesimal magnetic field. The lowest five distinct angular momentum subbands are labeled by their color: $l = 0, |f| = \frac{1}{2}$ (blue), $|l| = 1, |f| = \frac{1}{2}$ (green), $|l| = 1, |f| = \frac{3}{2}$ (red), $|l| = 2, |f| = \frac{3}{2}$ (cyan) and $|l| = 2, |f| = \frac{5}{2}$ (magenta). The subbands induced by the confinement in z direction are marked in gray.

Fig. 7.7 (a) we show the SOI splittings ΔE_1 and ΔE_2 as a function of wire diameter. For wire diameters smaller than 100 nm it is approximately constant. For small wire diameters the SOI splitting is approximately given by [62]

$$\Delta E_l = E(l + \frac{1}{2}) - E(l - \frac{1}{2}) = -l \frac{2m^* \alpha^2}{\hbar^2}, \tag{7.33}$$

which is in good agreement with our numerical solution. Note that the sign is opposite from the zincblende hard boundary case. For large wire diameters (around 100 nm) the subband splitting becomes of similar size as the SOI splitting leading to a reduction of the SOI splitting. This is also visible in the rescaled energies shown in Fig. 7.7 (b).

While the Rashba model can explain the origin of the SOI splitting in wurtzite wires it neglects several other aspects like the nonparabolicity of bands and the cubic Dresselhaus splitting. Therefore, we solve the 8-band **k**·**p**-model for wurtzite InAs introduced in Ref. [52] in cylindrical coordinates. Note, that the model is already axially symmetric and no further simplification is needed as in the zincblende case. The results are shown in Fig. 7.7 (c) and (d). For small wire diameter the cubic in k Dresselhaus spin splitting dominates over the linear in k Rashba splitting and causes an SOI splitting that is different in sign. At large wire diameter the results are very similar to the Rashba model.

QUANTUM DOTS

The same reasoning as for wires leads to enhanced g-factors in quantum dots with (approximate) cylindrical symmetry. Cylindrically symmetric quantum dots are simulated in the axial approximation. Due to the additional confinement in z-direction a 2D boundary value problem needs to be solved now.

In Fig. 7.8 we investigate the length dependence of the g-factor in a short cylindrical InSb wire of 40 nm diameter. The g-factors of higher subbands stay larger than the bulk g-factor even when the wire length is already much shorter than the wire diameter. The kinks in the g-factors result from level crossings with z-confinement induced subbands.

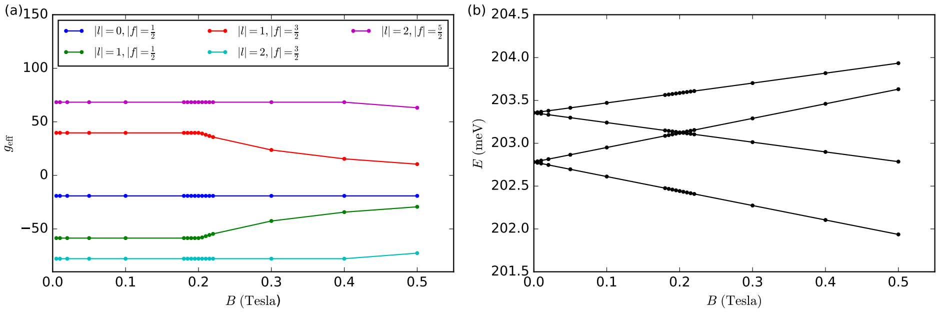

Figure 7.9: Tight-binding simulation of a hexagonal InSb wire, grown in the 111 direction, with 20.1 nm diameter. (a) The g-factor of the lowest five Kramers pairs in the conduction states as a function of B. (b) Energy levels of the lowest $|l| = 1$ states as a function of B.

Therefore, besides wires, the enhanced g-factors could be observed in gate-defined quantum dots embedded in a 2DEG, either of circular or approximately square shape (the square case is treated below). We also expect orbital contributions to be relevant to quantum rings hosting possible Majorana bound states [63].

7.6.2. TIGHT-BINDING SIMULATIONS

The $\mathbf{k}\cdot\mathbf{p}$ approximation is only guaranteed to work for long wavelengths and the zincblende $\mathbf{k}\cdot\mathbf{p}$ model used in our simulations neglects the Dresselhaus term, which results from inversion symmetry breaking. For comparison, we also simulate semiconductor wires in zincblende structure using highly accurate first-principles derived tight-binding models. In the tight-binding framework the states are described correctly in the whole Brillouin zone of the lattice, thus, abrupt changes like a hard boundary pose no problem.

For the first-principles calculations we used the Vienna *ab initio* simulation package (VASP) [44, 45] with the projector augmented-wave method, a cut-off energy of 300 eV and using the HSE06 hybrid functional [48–50]. The BZ integration was faciliated with an 8×8×8 Monkhorst-Pack mesh. Due to the computational complexity of the HSE06 functional only bulk unit cells were considered directly with *ab initio* methods. Instead, wire calculations use an effective tight-binding Hamiltonian generated from the first-principles Wannier functions [41], by projecting the first-principles wave-function on the s and p-like orbitals of In, As and Sb. The magnetic field is added via Peierls substitution to the Hamiltonian [64].

In Fig. 7.9 we show results for a InSb wire grown in the 111 direction and with 20.1 nm diameter. The measured g-factors and the critical magnetic field B_{crit} of about 0.2 Tesla agree qualitatively with the $\mathbf{k}\cdot\mathbf{p}$-results presented in the main text. We also find that for the $l \neq 0$ states the Kramers pair with negative g-factor, corresponding to $\left|\pm|l|, \mp\frac{1}{2}\right\rangle$, is lower in energy than the one with positive g-factor, which corresponds to $\left|\pm|l|, \pm\frac{1}{2}\right\rangle$. Thus, the tight-binding approach gives the same sign of ΔE_l as the hard wall case in $\mathbf{k}\cdot\mathbf{p}$, justifying our choice of boundary conditions in the main text.

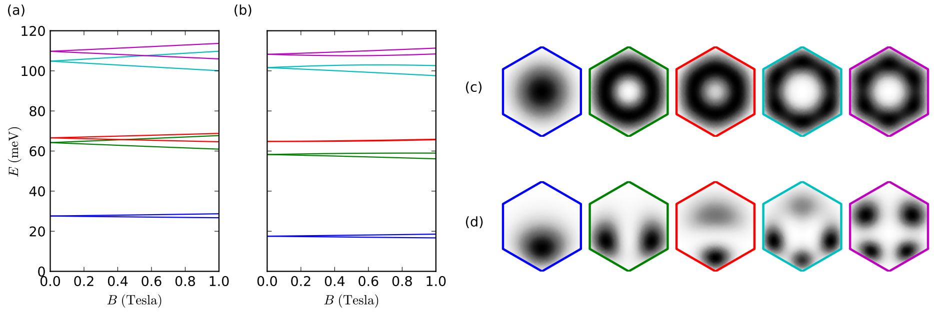

Figure 7.10: Hexagonal InSb wire with 40 nm diameter with perpendicular electric field. (a) ((b)) Energy levels of the first ten states as a function of B at an electric field of $\mathcal{E} = 0\,\text{meV/nm}$ ($\mathcal{E} = 3\,\text{meV/nm}$). In the $\mathcal{E} = 0$ case the colors mark different angular momenta. (c) ((d)) Norm squared wave functions of the first five conduction levels at $k = 0$ and $B = 0$ at an electric field of $\mathcal{E} = 0\,\text{meV/nm}$ ($\mathcal{E} = 3\,\text{meV/nm}$).

7.6.3. k·p SIMULATIONS WITH BROKEN CYLINDRICAL SYMMETRY

HEXAGONAL WIRES

In the main text we consider hexagonal wires grown in the 111 direction of a zincblende semiconductor. Again we take the **k·p**-parameters from Ref. [6]. The 8-band Kane model, this time without the axial approximation, is taken from Ref. [6] and is discretized on a simple cubic lattice. Apart from the Majorana simulations we use a lattice constant of 0.5 nm for the discretization. The wire is built and infinitely extended in the 111 direction. Magnetic and electric fields are added to the lattice Hamiltonian [64]. Note that the simple cubic discretization conserves all symmetries of the cubic zincblende lattice, thus also conserving all symmetries of the wire. Sparse diagonalization is finally used to solve for the eigenenergies and eigenstates of the wire. In Fig. 7.10 we show results for a hexagonal InSb wire of 40 nm diameter.

In previous 8-band zincblende **k·p** simulations we neglected the Dresselhaus term. While we implicitly checked that the Dresselhaus term does not introduce significant changes via the tight-binding calculation, it is convenient to have a direct comparison of 8-band **k·p** results with and without Dresselhaus term. The Dresselhaus term is added to the 8-band **k·p** Hamiltonian using the definitions and parameters of Ref. [6]. In principle, the Dresselhaus term should affect the SOI splitting ΔE_l, like it is the case in wurtzite wires. However, for InAs and InSb it is too small in magnitude to have a significant effect, see Fig. 7.11.

RECTANGULAR WIRES

In the main text we focused on hexagonal and cylindrical wires, here we consider now rectangular wires. The parameters of the simulation are identical to the hexagonal case apart from the the growth direction which is now 001.

For a simple quadratic band with effective mass m^* the energy levels at $k = 0$ of a

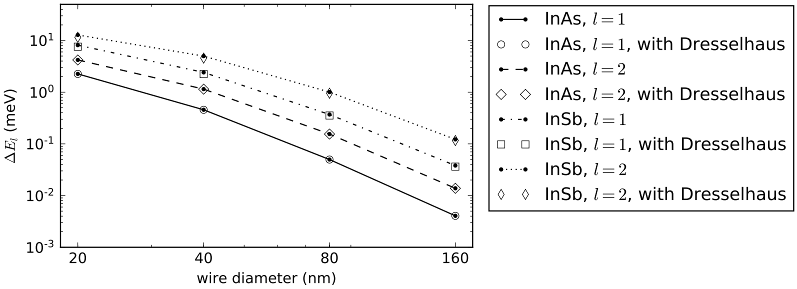

Figure 7.11: Diameter dependence of the SOI splitting ΔE_1 and ΔE_2 for hexagonal InSb and InAs wires ($B = 0$ and $\mathcal{E} = 0$). Results with and without Dresselhaus term are compared.

rectangular wire with dimensions L_x and L_y are given by

$$E_{n_x,n_y} = \frac{\hbar^2}{2m^*}\left[\left(\frac{n_x\pi}{L_x}\right)^2 + \left(\frac{n_y\pi}{L_y}\right)^2\right], \tag{7.34}$$

with the quantum numbers n_x and n_y taking on nonzero positive integer values. The corresponding wavefunctions are given by

$$\psi_{n_x,n_y}(x,y,z) = \frac{1}{\sqrt{N_{n_x,n_y}}}\sin\left(\frac{n_x\pi}{L_x}x\right)\sin\left(\frac{n_y\pi}{L_y}y\right)e^{ikz}, \tag{7.35}$$

where $N(n_x, n_y)$ is a normalization factor.

In the case $L_x = L_y$ the lowest energy level is $E_{0,0}$ and the first excited level is two-fold degenerate $E_{1,2} = E_{2,1}$. With SOI the two-fold degeneracy is lifted into two separate states with $f_z \approx \frac{1}{2}$ and $f_z = \frac{3}{2}$ with SOI splitting ΔE_1. Note that due to the C_4 symmetry of the wire the angular momenta $f_z = \{-\frac{3}{2}, -\frac{1}{2}, \ \frac{1}{2}, \ \frac{3}{2}\}$ are still in different symmetry sectors. Therefore, we can still talk of the $l \approx 1$ subbands as in the cylindrical case and also the enhanced g-factors are found.

This is illustrated in Fig. 7.12 where a rectangular InSb wire is simulated. For $L_x = L_y$ we find ΔE_1 and the g-factor for the $l \approx 1$ bands similar to the cylindrical and hexagonal case. The wavefunctions of the second and third state shown in Fig. 7.12 (c) are clearly angular momentum eigenstates.

Upon deformation of the quadratic wire the geometry splitting of the second and third state soon surpasses the SOI splitting ΔE_1 and g-factors decline rapidly, see Fig. 7.12 (a) and (b). In the simple quadratic band model the geometry splitting is given by

$$E_{n_x,n_y} - E_{n_y,n_x} = \frac{\hbar^2\pi^2}{2m^*}\left(\frac{1}{L_x^2} - \frac{1}{L_y^2}\right)(n_x^2 - n_y^2), \tag{7.36}$$

which is also found in good approximation in our more sophisticated 8-band $\mathbf{k}\cdot\mathbf{p}$ calculation. If L_x and L_y differ enough the geometry splitting exceeds the SOI splitting and the wavefunctions are no more angular momentum eigenstates, see Fig. 7.12 (d).

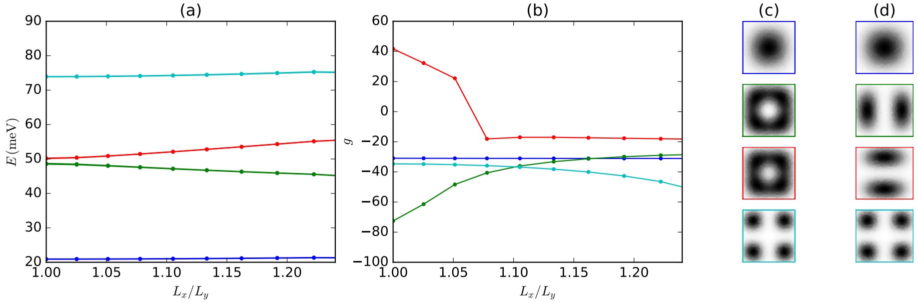

Figure 7.12: Results for rectangular InSb wires with fixed crossection of $40 \times 40 = 1600\,\mathrm{nm}^2$ and variable ratio of height to width (L_x/L_y). (a) ((b)) Energy levels (g-factors) of the first four conduction Kramers pairs as a function L_x/L_y. (c) ((d)) Norm squared wave functions of the first four conduction states at $L_x/L_y = 1$ ($L_x/L_y = 1.1$). The color code for the Kramers pairs is the same in (a), (b), (c) and (d).

EFFICIENT MAJORANA WIRE SIMULATIONS

The realization of Majorana states requires a proximity induced superconducting pairing potential in the wire [19, 20]. For the superconducting calculations we transform the zincblende **k·p** Hamiltonian in the Bogoliubov de Gennes (BdG) basis and double the Hilbert space via adding the hole degrees of freedom. Then, we add an s-wave pairing term $\hat{\Delta}$ to the off-diagonal block of the Hamiltonian [65]

$$H_{\mathrm{BdG}}(k_z) = \begin{pmatrix} H(k_z) & \hat{\Delta} \\ \hat{\Delta}^\dagger & -H^*(-k_z) \end{pmatrix}. \tag{7.37}$$

The s-wave pairing $\hat{\Delta}$ is assumed to be local and is kept constant throughout the wire. Furthermore, we restrict it to the conduction band s-like orbitals (the $|u_1\rangle$ and $|u_2\rangle$ basis states), which dominate near the Fermi level. It is then of the form

$$\hat{\Delta} = \Delta \sum_i \left(c^\dagger_{i\uparrow} c^\dagger_{i\downarrow} + \mathrm{h.c.} \right), \tag{7.38}$$

where c and $c^\dagger$ are annihilation and creation operators and with i running over all sites and the s-like $|u_1\rangle = i\uparrow$ and $|u_2\rangle = i\downarrow$ basis states.

Differential conductivity measurements in semiconductor nanowires in contact to a superconductor are an important probe of possible Majorana states [12–17]. Simulating a realistic infinite wire is already computationally demanding, however, simulating a finite 3D wire long enough to host protected Majorana modes by exact diagonalization would be a hopeless endeavor using current computer hardware. Using the clever Sancho-Rubio scheme [66, 67] it is possible to significantly lessen the computational strain to something which is tractable on modern supercomputers. With the Sancho-Rubio scheme one can simulate the boundary and bulk Greens function of a wire in an iterative fashion, doubling the effective wire length in each iteration [68].

We begin by writing the 1D Hamiltonian in a form that has only nearest neighbor interactions and is translationally invariant inside the wire

$$H_{\text{wire}} = \begin{pmatrix} \epsilon & \alpha & & \\ \beta & \epsilon & \alpha & \\ & \beta & \epsilon & \ddots \\ & & \ddots & \ddots \end{pmatrix}, \tag{7.39}$$

where $\beta = \alpha^{\dagger}$. Longer range interactions can be incorporated by artificially increasing the size of the unit cell such that the effective interactions become nearest neighbor again. Now one can make use of Dyson's identity to write the Green's function $G_{n=2}$ at the left site for a chain of length 2

$$G_{n=2}^{-1} = \omega - \underbrace{(\epsilon + \alpha(\omega-\epsilon)^{-1}\beta)}_{\epsilon_1^s}, \tag{7.40}$$

where ω is the energy and ϵ_1^s is an effective Hamiltonian for the left surface site. Equivalently, one can attach two sites to the left and to the right to obtain the effective bulk Hamiltonian in the middle of a chain of three sites

$$\epsilon_1 = \epsilon_0 + \alpha(\omega-\epsilon)^{-1}\beta) + \beta(\omega-\epsilon)^{-1}\alpha. \tag{7.41}$$

It can be shown that the new effective interactions α_1 and β_1 for the effective Hamiltonians ϵ_1 and ϵ_1^s are given by [67]

$$\alpha_1 = \alpha(\omega-\epsilon)^{-1}\alpha \tag{7.42}$$

$$\beta_1 = \beta(\omega-\epsilon)^{-1}\beta. \tag{7.43}$$

Thus the effective Hamiltonian for a system of length $2^l a$, with a being the lattice constant of the chain, can be obtained by iterating the following set of equations

$$\alpha_l = \alpha_{l-1}(\omega-\epsilon_{l-1})^{-1}\alpha_{l-1} \tag{7.44}$$

$$\beta_l = \beta_{l-1}(\omega-\epsilon_{l-1})^{-1}\beta_{l-1} \tag{7.45}$$

$$\epsilon_l = \epsilon_{l-1} + \alpha_{l-1}(\omega-\epsilon_{l-1})^{-1}\beta_{l-1} + \beta_{l-1}(\omega-\epsilon_{l-1})^{-1}\alpha_{l-1}) \tag{7.46}$$

$$\epsilon_l^s = \epsilon_{l-1}^s + \alpha_{l-1}(\omega-\epsilon_{l-1})^{-1}\beta_{l-1}. \tag{7.47}$$

The bulk and surface Green's function are given by $G_b = (\omega-\epsilon_l)^{-1}$ and $G_s = (\omega-\epsilon_s)^{-1}$. In practice a small imaginary part is added to ω to broaden the energy levels for better visibility.

From the diagonal part of the Greens function we obtain the local density of states (LDOS) at the boundary of the wire, which is closely related to the differential conductivity [69]. Due to the increased computational effort a coarser discretization with a lattice constant of 2.5 nm is used in these simulations.

REFERENCES

[1] D. Stein, K. v. Klitzing, and G. Weimann, *Electron Spin Resonance on* GaAs – $\mathrm{Al}_x\mathrm{Ga}_{1-x}\mathrm{As}$ *Heterostructures,* Phys. Rev. Lett. **51**, 130 (1983).

[2] G. Lommer, F. Malcher, and U. Rössler, *Reduced g factor of subband Landau levels in AlGaAs/GaAs heterostructures,* Phys. Rev. B **32**, 6965 (1985).

[3] E. L. Ivchenko and A. A. Kiselev, Sov Phys Semicond **26**, 827 (1992).

[4] A. A. Kiselev, E. L. Ivchenko, and U. Rössler, *Electron g factor in one- and zero-dimensional semiconductor nanostructures,* Phys. Rev. B **58**, 16353 (1998).

[5] T. Ando and Y. Uemura, *Theory of Oscillatory g Factor in an MOS Inversion Layer under Strong Magnetic Fields,* J. Phys. Soc. Jpn. **37**, 1044 (1974).

[6] R. Winkler, *Spin-Orbit Coupling Effects in Two-Dimensional Electron and Hole Systems* (Springer, Berlin, Heidelberg, 2003).

[7] L. M. Roth, B. Lax, and S. Zwerdling, *Theory of Optical Magneto-Absorption Effects in Semiconductors,* Phys. Rev. **114**, 90 (1959).

[8] S. Csonka, L. Hofstetter, F. Freitag, S. Oberholzer, C. Schönenberger, T. S. Jespersen, M. Aagesen, and J. Nygård, *Giant Fluctuations and Gate Control of the g-Factor in InAs Nanowire Quantum Dots,* Nano Lett. **8**, 3932 (2008).

[9] M. D. Schroer, K. D. Petersson, M. Jung, and J. R. Petta, *Field Tuning the g Factor in InAs Nanowire Double Quantum Dots,* Phys. Rev. Lett. **107**, 176811 (2011).

[10] H. A. Nilsson, P. Caroff, C. Thelander, M. Larsson, J. B. Wagner, L.-E. Wernersson, L. Samuelson, and H. Q. Xu, *Giant, Level-Dependent g Factors in InSb Nanowire Quantum Dots,* Nano Lett. **9**, 3151 (2009).

[11] I. van Weperen, S. R. Plissard, E. P. A. M. Bakkers, S. M. Frolov, and L. P. Kouwenhoven, *Quantized Conductance in an InSb Nanowire,* Nano Lett. **13**, 387 (2013).

[12] A. Das, H. Shtrikman, M. Heiblum, Y. Most, Y. Oreg, and Y. Ronen, *Zero-bias peaks and splitting in an Al–InAs nanowire topological superconductor as a signature of Majorana fermions,* Nat. Phys. **8**, 887 (2012).

[13] M. T. Deng, C. L. Yu, G. Y. Huang, M. Larsson, P. Caroff, and H. Q. Xu, *Anomalous Zero-Bias Conductance Peak in a Nb–InSb Nanowire–Nb Hybrid Device,* Nano Lett. **12**, 6414 (2012).

[14] V. Mourik, K. Zuo, S. M. Frolov, S. R. Plissard, E. P. a. M. Bakkers, and L. P. Kouwenhoven, *Signatures of Majorana Fermions in Hybrid Superconductor-Semiconductor Nanowire Devices,* Science **336**, 1003 (2012).

[15] S. M. Albrecht, A. P. Higginbotham, M. Madsen, F. Kuemmeth, T. S. Jespersen, J. Nygård, P. Krogstrup, and C. M. Marcus, *Exponential protection of zero modes in Majorana islands,* Nature **531**, 206 (2016).

[16] H. Zhang, Ö. Gül, S. Conesa-Boj, M. P. Nowak, M. Wimmer, K. Zuo, V. Mourik, F. K. d. Vries, J. v. Veen, M. W. A. d. Moor, J. D. S. Bommer, D. J. v. Woerkom, D. Car, S. R. Plissard, E. P. A. M. Bakkers, M. Quintero-Pérez, M. C. Cassidy, S. Koelling, S. Goswami, K. Watanabe, T. Taniguchi, and L. P. Kouwenhoven, *Ballistic superconductivity in semiconductor nanowires,* Nat. Commun. **8**, 16025 (2017).

[17] Ö. Gül, H. Zhang, J. D. S. Bommer, M. W. A. de Moor, D. Car, S. R. Plissard, E. P. A. M. Bakkers, A. Geresdi, K. Watanabe, T. Taniguchi, and L. P. Kouwenhoven, *Ballistic Majorana nanowire devices,* Nature Nanotechnology (2018), 10.1038/s41565-017-0032-8.

[18] A. Y. Kitaev, *Unpaired Majorana fermions in quantum wires,* Phys.-Usp. **44**, 131 (2001).

[19] R. M. Lutchyn, J. D. Sau, and S. Das Sarma, *Majorana Fermions and a Topological Phase Transition in Semiconductor-Superconductor Heterostructures,* Phys. Rev. Lett. **105**, 077001 (2010).

[20] Y. Oreg, G. Refael, and F. von Oppen, *Helical Liquids and Majorana Bound States in Quantum Wires,* Phys. Rev. Lett. **105**, 177002 (2010).

[21] A. Y. Kitaev, *Fault-tolerant quantum computation by anyons,* Annals of Physics **303**, 2 (2003).

[22] C. Nayak, S. H. Simon, A. Stern, M. Freedman, and S. Das Sarma, *Non-Abelian anyons and topological quantum computation,* Rev. Mod. Phys. **80**, 1083 (2008).

[23] M. Kjaergaard, K. Wölms, and K. Flensberg, *Majorana fermions in superconducting nanowires without spin-orbit coupling,* Phys. Rev. B **85**, 020503 (2012).

[24] G. L. Fatin, A. Matos-Abiague, B. Scharf, and I. Žutić, *Wireless Majorana Bound States: From Magnetic Tunability to Braiding,* Phys. Rev. Lett. **117**, 077002 (2016).

[25] A. Matos-Abiague, J. Shabani, A. D. Kent, G. L. Fatin, B. Scharf, and I. Žutić, *Tunable magnetic textures: From Majorana bound states to braiding,* Solid State Communications **262**, 1 (2017).

[26] I. Žutić, J. Fabian, and S. Das Sarma, *Spintronics: Fundamentals and applications,* Rev. Mod. Phys. **76**, 323 (2004).

[27] C. R. Pidgeon, D. L. Mitchell, and R. N. Brown, *Interband Magnetoabsorption in InAs and InSb,* Phys. Rev. **154**, 737 (1967).

[28] S. Vaitiekėnas, M. T. Deng, and C. M. Marcus, private communication .

[29] L. D. Landau and E. M. Lifshitz, *Quantum Mechanics: Non-Relativistic Theory* (Elsevier, 1981).

[30] F. Kuemmeth, S. Ilani, D. C. Ralph, and P. L. McEuen, *Coupling of spin and orbital motion of electrons in carbon nanotubes,* Nature **452**, 448 (2008).

[31] E. A. Laird, F. Kuemmeth, G. A. Steele, K. Grove-Rasmussen, J. Nygård, K. Flensberg, and L. P. Kouwenhoven, *Quantum transport in carbon nanotubes,* Rev. Mod. Phys. **87**, 703 (2015).

[32] E. O. Kane, *Band structure of indium antimonide,* J Phys Chem Solids **1**, 249–261 (1957).

[33] B. A. Foreman, *Elimination of spurious solutions from eight-band* $k \cdot p$ *theory,* Phys. Rev. B **56**, R12748–R12751 (1997).

[34] P. C. Sercel and K. J. Vahala, *Analytical formalism for determining quantum-wire and quantum-dot band structure in the multiband envelope-function approximation,* Phys. Rev. B **42**, 3690 (1990).

[35] K. J. Vahala and P. C. Sercel, *Application of a total-angular-momentum basis to quantum-dot band structure,* Phys. Rev. Lett. **65**, 239 (1990).

[36] S. Çakmak, A. M. Babayev, E. Artunç, A. Kökçe, and S. Çakmaktepe, *g-Factor of carriers in Kane-type semiconductor wire,* Physica E: Low-dimensional Systems and Nanostructures **18**, 365 (2003).

[37] L. C. Lew Yan Voon, C. Galeriu, B. Lassen, M. Willatzen, and R. Melnik, *Electronic structure of wurtzite quantum dots with cylindrical symmetry,* Appl. Phys. Lett. **87**, 041906 (2005).

[38] R. W. Robinett, *Quantum mechanics of the two-dimensional circular billiard plus baffle system and half-integral angular momentum,* Eur. J. Phys. **24**, 231 (2003).

[39] S. Tarucha, D. G. Austing, T. Honda, R. J. van der Hage, and L. P. Kouwenhoven, *Shell Filling and Spin Effects in a Few Electron Quantum Dot,* Phys. Rev. Lett. **77**, 3613 (1996).

[40] A. V. Rodina, A. Y. Alekseev, A. L. Efros, M. Rosen, and B. K. Meyer, *General boundary conditions for the envelope function in the multiband* $\boldsymbol{k}\cdot\boldsymbol{p}$ *model,* Phys. Rev. B **65**, 125302 (2002).

[41] A. A. Mostofi, J. R. Yates, G. Pizzi, Y.-S. Lee, I. Souza, D. Vanderbilt, and N. Marzari, *An updated version of wannier90: A tool for obtaining maximally-localised Wannier functions,* Computer Physics Communications **185**, 2309 (2014).

[42] G. Kresse and J. Hafner, *Ab initio,* Phys. Rev. B **47**, 558 (1993).

[43] G. Kresse and J. Hafner, *Ab initio,* Phys. Rev. B **49**, 14251 (1994).

[44] G. Kresse and J. Furthmüller, *Efficient iterative schemes for ab initio total-energy calculations using a plane-wave basis set,* Phys. Rev. B **54**, 11169 (1996).

[45] G. Kresse and J. Furthmüller, *Efficiency of ab-initio total energy calculations for metals and semiconductors using a plane-wave basis set,* Computational Materials Science **6**, 15 (1996).

[46] P. E. Blöchl, *Projector augmented-wave method,* Phys. Rev. B **50**, 17953 (1994).

[47] G. Kresse and D. Joubert, *From ultrasoft pseudopotentials to the projector augmented-wave method,* Phys. Rev. B **59**, 1758 (1999).

[48] Y.-S. Kim, K. Hummer, and G. Kresse, *Accurate band structures and effective masses for InP, InAs, and InSb using hybrid functionals,* Phys. Rev. B **80**, 035203 (2009).

[49] J. Heyd, G. E. Scuseria, and M. Ernzerhof, *Hybrid functionals based on a screened Coulomb potential,* The Journal of Chemical Physics **118**, 8207 (2003).

[50] J. Heyd and G. E. Scuseria, *Efficient hybrid density functional calculations in solids: Assessment of the Heyd–Scuseria–Ernzerhof screened Coulomb hybrid functional,* The Journal of Chemical Physics **121**, 1187 (2004).

[51] L. C. Lew Yan Voon, M. Willatzen, M. Cardona, and N. E. Christensen, *Terms linear in k in the band structure of wurtzite-type semiconductors,* Phys. Rev. B **53**, 10703 (1996).

[52] P. E. Faria Junior, T. Campos, C. M. O. Bastos, M. Gmitra, J. Fabian, and G. M. Sipahi, *Realistic multiband* $\boldsymbol{k}\cdot\boldsymbol{p}$ *approach from ab initio and spin-orbit coupling effects of InAs and InP in wurtzite phase,* Phys. Rev. B **93**, 235204 (2016).

[53] P. Krogstrup, N. L. B. Ziino, W. Chang, S. M. Albrecht, M. H. Madsen, E. Johnson, J. Nygård, C. M. Marcus, and T. S. Jespersen, *Epitaxy of semiconductor–superconductor nanowires,* Nat. Mater. **14**, 400 (2015).

[54] M. Gmitra and J. Fabian, *First-principles studies of orbital and spin-orbit properties of GaAs, GaSb, InAs, and InSb zinc-blende and wurtzite semiconductors,* Phys. Rev. B **94**, 165202 (2016).

[55] B. Nijholt and A. R. Akhmerov, *Orbital effect of magnetic field on the Majorana phase diagram,* Phys. Rev. B **93**, 235434 (2016).

[56] H. W. van Kesteren, E. C. Cosman, W. A. J. A. van der Poel, and C. T. Foxon, *Fine structure of excitons in type-II GaAs/AlAs quantum wells,* Phys. Rev. B **41**, 5283 (1990).

[57] P. Peyla, A. Wasiela, Y. Merle d'Aubigné, D. E. Ashenford, and B. Lunn, *Anisotropy of the Zeeman effect in CdTe/*$\mathrm{Cd}_{1-x}\mathrm{Mn}_x$*Te multiple quantum wells,* Phys. Rev. B **47**, 3783 (1993).

[58] W. Chang, S. M. Albrecht, T. S. Jespersen, F. Kuemmeth, P. Krogstrup, J. Nygård, and C. M. Marcus, *Hard gap in epitaxial semiconductor–superconductor nanowires,* Nat. Nanotechnol. **10**, 232 (2015).

[59] T. D. Stanescu, R. M. Lutchyn, and S. Das Sarma, *Majorana fermions in semiconductor nanowires,* Phys. Rev. B **84**, 144522 (2011).

[60] D. Sticlet, B. Nijholt, and A. Akhmerov, *Robustness of Majorana bound states in the short-junction limit,* Phys. Rev. B **95**, 115421 (2017).

[61] F. Nichele, M. Kjaergaard, H. J. Suominen, R. Skolasinski, M. Wimmer, B.-M. Nguyen, A. A. Kiselev, W. Yi, M. Sokolich, M. J. Manfra, F. Qu, A. J. Beukman, L. P. Kouwenhoven, and C. M. Marcus, *Giant Spin-Orbit Splitting in Inverted InAs/GaSb Double Quantum Wells,* Phys. Rev. Lett. **118**, 016801 (2017).

[62] E. N. Bulgakov and A. F. Sadreev, *Spin polarization in quantum dots by radiation field with circular polarization,* Jetp Lett. **73**, 505 (2001).

[63] B. Scharf and I. Žutić, *Probing Majorana-like states in quantum dots and quantum rings,* Phys. Rev. B **91**, 144505 (2015).

[64] M. Graf and P. Vogl, *Electromagnetic fields and dielectric response in empirical tight-binding theory,* Phys. Rev. B **51**, 4940 (1995).

[65] M. Tinkham, *Introduction to Superconductivity* (Courier Corporation, 1996).

[66] M. P. L. Sancho, J. M. L. Sancho, and J. Rubio, *Quick iterative scheme for the calculation of transfer matrices: application to Mo (100),* J. Phys. F: Met. Phys. **14**, 1205 (1984).

[67] M. P. L. Sancho, J. M. L. Sancho, J. M. L. Sancho, and J. Rubio, *Highly convergent schemes for the calculation of bulk and surface Green functions,* J. Phys. F: Met. Phys. **15**, 851 (1985).

[68] M. Luisier, A. Schenk, W. Fichtner, and G. Klimeck, *Atomistic simulation of nanowires in the* $sp^3d^5s^*$ *tight-binding formalism: From boundary conditions to strain calculations,* Phys. Rev. B **74**, 205323 (2006).

[69] S. Datta, *Electronic Transport in Mesoscopic Systems* (Cambridge University Press, 1997).

8

CONCLUSIONS

8.1. CHAPTER 3

We discussed the two numerical methods used in this thesis. First, we proposed a discretization algorithm that automatizes the process of obtaining a tight binding Hamiltonian from a continuous one. The discretization algorithm works with any power of momentum operators and properly treats all space-dependent parameters in the Hamiltonian. The reference implementation has been released as a part of Kwant simulation package [1]. Second, we discussed an implementation of Löwdin perturbation theory [2, 3]. Our implementation allows to obtain numerically an effective model up to a specified order of perturbation. The resulting effective models are an analytic polynomial in the specified free parameters, e.g. magnetic field or in-plane momentum. The reference implementation is planned to be a part of a future Kwant release. Code is available upon request.

8.2. CHAPTER 4

We used numerical calculations to analyse band structure and effective models of two-dimensional InAs/GaSb and HgTe/CdTe heterostructures. A detailed $\mathbf{k}\cdot\mathbf{p}$ [4–7] analysis revealed a burying of the Dirac point in the valence band. We showed that together with a suppression of the edge-state g-factor this mechanism is a plausible explanation why experiments on quantum spin Hall effect in InAs/GaSb shows extraordinary robustness to magnetic field.

We found that the burying of the Dirac point is a generic feature for both InAs/GaSb and HgTe/CdTe systems. The Dirac point is inside the topological gap only close to the topological phase transition. Localizing the Majorana zero modes requires to align the chemical potential with the edge-state Zeeman gap [8, 9]. Because of that, the quantum spin Hall edge states can be used as a Majorana platform only if the Dirac point is located in the topological gap. We therefore recommend to operate in the regime close to the topological phase transition where the edge-state crossing remains in the gap.

Possible continuation of the research could be concentrated on investigating different growth directions (other than 001) and different direction of edges (other than 100 or 010).

8.3. CHAPTER 5

We investigated the spin-orbit interaction in a dual gated InAs/GaSb quantum well. By using the back and top gate of the device, it was possible to tune the system from single carrier (only electron) to two-carriers (both electron and hole) regimes in the experiment [10]. In the single carrier regime, by comparing the Shubnikov-de Haas oscillations data with the results of Landau level simulations, we extracted the strength of the linear Dresselaus as $\beta = 28.5$ meVÅ and the Rashba coefficient α as between 75 and 53 meVÅ as the electric field changes. Experimentally, in the two-carrier regime, a quenching of the spin-splitting has been observed.

Our $\mathbf{k}{\cdot}\mathbf{p}$ band structure calculations are consistent with the experimental observations. We showed that in the single-carrier regime the Rashba coefficient α show strong response to the change of electric field, whereas effect on β is negligible. In the two-carrier regime the $\mathbf{k}{\cdot}\mathbf{p}$ calculations revealed crossing of the bands with different spin that explains the experimentally observed quenching of the spin-splitting.

An interesting direction of further research is how the strength of the spin-orbit interaction depends on the different topological regime (inverted, trivial, close to phase transition) as well as on the size of topological gap.

8.4. CHAPTER 6

We discussed a giant spin-orbit splitting observed in inverted InAs/GaSb quantum wells. A fully spin-orbit polarized state has been found in both electron-like and hole-like states. Hall plateaus evolving in e^2/h steps and a non-trivial Berry phase confirmed the 100% polarization of the system.

In the $\mathbf{k}{\cdot}\mathbf{p}$ band structure calculation we observe that bands with different spin have different energy gaps that is consistent with the experimental observation of full spin-orbit polarization.

8.5. CHAPTER 7

We discussed the orbital contributions to the electron g-factor in semiconductor nanowires. First, we investigated problem analytically using the cylindrical approximation. We showed that an $\boldsymbol{L}\cdot\boldsymbol{S}$ coupling in higher subbands leads to an enhancement of the g-factor of an order of magnitude or more in semiconductors with a small effective mass. We validated our theoretical finding with simulations of InAs and InSb band structure using the $\mathbf{k}{\cdot}\mathbf{p}$ model with axial approximation. Second, we investigated wires with square and hexagonal cross section without the axial approximation. We showed that the effect persists even if cylindrical symmetry is broken.

We observed that similar results apply to quantum dots. For cylindrical quantum dots, we found that orbital g-factor enhancements are still significant if the length of the dot is much shorter than its diameter. Due to the observed robustness of the effect, it should also applied in irregularly shaped quantum dots, which may be a subject of further research.

REFERENCES

[1] C. W. Groth, M. Wimmer, A. R. Akhmerov, and X. Waintal, *Kwant: a software package for quantum transport*, New J. Phys. **16**, 063065 (2014).

[2] P. Löwdin, *A Note on the Quantum-Mechanical Perturbation Theory*, J. Chem. Phys. **19**, 1396–1401 (1951).

[3] R. Winkler, *Spin-Orbit Coupling Effects in Two-Dimensional Electron and Hole Systems* (Springer, Berlin, Heidelberg, 2003).

[4] E. O. Kane, *Band structure of indium antimonide*, J Phys Chem Solids **1**, 249–261 (1957).

[5] E. O. Kane, *Semiconductors and Semimetals*, in *Physics of III-V-Compounds*, Vol. 1, edited by R. K. Willardson and A. C. Beer (Academic Press, New York, London, 1966) pp. 75–100.

[6] E. O. Kane, in *Handbook on Semiconductors*, Vol. 1, edited by W. Paul and F. John (North-Holland, Amsterdam, 1982) p. 193.

[7] G. Bastard, *Wave Mechanics Applied to Semiconductor Heterostructures* (Wiley, New York, 1988).

[8] L. Fu and C. L. Kane, *Josephson current and noise at a superconductor/quantum-spin-Hall-insulator/superconductor junction*, Phys. Rev. B **79**, 161408 (2009).

[9] J. Alicea, *New directions in the pursuit of Majorana fermions in solid state systems*, Rep. Prog. Phys. **75**, 076501 (2012).

[10] F. Qu, A. J. Beukman, S. Nadj-Perge, M. Wimmer, B.-M. Nguyen, W. Yi, J. Thorp, M. Sokolich, A. A. Kiselev, M. J. Manfra, C. M. Marcus, and L. P. Kouwenhoven, *Electric and Magnetic Tuning Between the Trivial and Topological Phases in InAs/GaSb Double Quantum Wells*, Phys. Rev. Lett. **115**, 036803 (2015).

CURRICULUM VITÆ

Rafał Jarosław SKOLASIŃSKI

12-01-1989 Born in Warsaw, Poland.

EDUCATION

2005–2008 High School
XVIII L.O. Jana Zamoyskiego, Warsaw

2008–2013 Bsc. and Msc. in Physics
Faculty of Physics, University of Warsaw

Bsc. Thesis: Examination of ground states of the quantum Heisenberg model
Promotor: Dr. J. Wojtkiewicz

Msc. Thesis: Exact diagonalization of hard-core bosons models in topologically non-trivial flat bands
Promotor: Dr. J. Tworzydło

2014–2018 PhD. in Physics
Delft University of Technology, Delft Netherlands

Thesis: Topology, Magnetism, and Spin-Orbit: A Band Structure Study of Semiconducting Nanodevices
Promotor: Prof. dr. Y. V. Nazarov
Copromotor: dr. M. T. Wimmer

LIST OF PUBLICATIONS

1. **Rafal Skolasinski**, Dmitry I. Pikulin, Jason Alicea, and Michael Wimmer, *Robust Helical Edge Transport in Quantum Spin Hall Quantum Wells*, arXiv:1709.04830 (2017).
2. Arjan J. A. Beukman, Folkert K. de Vries, Jasper van Veen, **Rafal Skolasinski**, Michael Wimmer, Fanming Qu, David T. de Vries, Binh-Minh Nguyen, Wei Yi, Andrey A. Kiselev, Marko Sokolich, Michael J. Manfra, Fabrizio Nichele, Charles M. Marcus, Leo P. Kouwenhoven, *Spin-orbit interaction in a dual gated InAs/GaSb quantum well*, Phys. Rev. B **96**, 241401(R) (2017)
3. Fabrizio Nichele, Morten Kjaergaard, Henri J. Suominen, **Rafal Skolasinski**, Michael Wimmer, Binh-Minh Nguyen, Andrey A. Kiselev, Wei Yi, Marko Sokolich, Michael J. Manfra, Fanming Qu, Arjan J.A. Beukman, Leo P. Kouwenhoven, Charles M. Marcus, *Giant spin-orbit splitting in inverted InAs/GaSb double quantum wells*, Phys. Rev. Lett. **118**, 016801 (2017).
4. Georg W. Winkler, Dániel Varjas, **Rafal Skolasinski**, Alexey A. Soluyanov, Matthias Troyer, and Michael Wimmer, *Orbital Contributions to the Electron g-factor in Semiconductor Nanowires*, Phys. Rev. Lett. **119**, 037701 (2017).
5. Jacek Wojtkiewicz, **Rafał Skolasiński**, *Inequalities between ground-state energies of Heisenberg models*, Physica A, **419**, 134-144, (2015).